Scattering processes in interacting Floquet systems

Martin Reitter

München, 2017

Scattering processes in interacting Floquet systems

Martin Reitter

Dissertation
an der Fakultät für Physik
der Ludwig–Maximilians–Universität
München

vorgelegt von
Martin Reitter
aus München

München, 23. Oktober 2017

Erstgutachter: Prof. Dr. Immanuel Bloch
Zweitgutachter: Prof. Dr. Ulrich Schollwöck
Tag der mündlichen Prüfung: 15. Dezember 2017

Zusammenfassung

Periodisches Treiben optischer Gitter ist ein vielseitiges Hilfsmittel auf dem Gebiet der ultrakalten Atome geworden, da es die Erzeugung neuartiger Bandstrukturen ermöglicht, die in statischen Gittersystemen nicht realisierbar sind. Diese Technik ermöglichte unter anderem die Erzeugung topologischer Bandstrukturen und künstlicher Magnetfelder für neutrale Atome. Experimente, die mit wechselwirkenden bosonischen Atomen durchgeführt wurden, litten jedoch häufig unter starkem Heizen, was die Lebenszeit des Systems deutlich reduzierte. Die Kombination von starken Wechselwirkungen und periodischem Treiben ist jedoch von großem Interesse, da sie die Untersuchung von topologischen Vielteilchensystemen, wie zum Beispiel gebrochenzahligen Quanten-Hall-Systemen, ermöglichen könnte. Aus diesem Grund ist ein Verständnis der zugrundeliegenden Heizmechanismen sehr wichtig, um Strategien entwickeln zu können, die das Heizen in zukünftigen Experimenten reduzieren.

Diese Arbeit berichtet von experimentell gemessenen Atomzahlverlusten aus einem wechselwirkenden Bose-Einstein-Kondensat, welches in einem periodisch getriebenen, eindimensionalen optischen Gitter gefangen ist. Es werden systematisch die Verlustraten für unterschiedliche Wechselwirkungsstärken und Schüttelparameter studiert. Ein besonderer Fokus liegt hierbei auf der Analyse zweier unterschiedlicher Parameterbereiche, die von experimenteller Bedeutung sind: Für Antriebsfrequenzen, die größer als die Bandbreite des untersten Bandes, aber dennoch klein im Vergleich zur Resonanzfrequenz zum ersten angeregten Band sind, wird das Tunnelmatrixelement zwischen zwei benachbarten Gitterplätzen durch eine Besselfunktion renormiert. Im zweiten betrachteten Regime liegen die Schüttelfrequenzen in der Bandlücke zwischen dem ersten und dem zweiten angeregten Band. In diesem Regime hybridisieren die Bänder sehr stark miteinander, was zu einer doppelmuldenartigen Dispersionsrelation des untersten Bandes führen kann. Das erstgenannte Regime kann dazu genutzt werden, künstliche Magnetfelder und topologische Bandstrukturen zu kreieren, wohingegen das letztgenannte Regime die Untersuchung symmetriegebrochener Domänen ermöglicht.

Zusätzlich zur experimentellen Bestimmung der Heizraten wird ein theoretisches Modell entwickelt, welches die zugrundeliegenden resonanten Streuprozesse beschreibt. Nach der Identifikation der dominanten Streukanäle können die resultierenden Heizraten des Systems mithilfe Fermis Goldener Regel abgeschätzt werden. Durch den Vergleich von experimentell gemessenen Heizraten und theoretisch abgeschätzen Raten findet man heraus, dass das Aufheizen des Systems reduziert werden kann, wenn resonant gestreute Teilchen direkt die Falle verlassen können, bevor sie ihre Energie an das System abgeben. Zusätzlich zu den Daten in einem eindimensionalen Gitter werden vorläufige Messungen von Heizraten in einem getriebenen hexagonalen Gitter präsentiert. Da die in dieser Arbeit diskutierten Heizmechanismen mindestens eine schwach eingeschlossene transversale Richtung

benötigen, könnte die Implementierung von Schüttelbewegungen in einer dreidimensionalen Gitterstruktur ein entscheidender Schritt zur Minimierung der Heizraten in angetriebenen Gittersystemen sein.

Abstract

The periodic driving of optical lattices has become a versatile tool in cold atoms experiments as it enables the creation of novel band structures not realizable in static lattice systems. This technique has facilitated both the creation of topological bands and artificial magnetic fields for neutral atoms. However, experiments conducted with interacting bosonic particles often suffered from strong heating, which leads to dramatically reduced lifetimes of the system. The combination of strong interactions and periodic driving is, however, of large interest as it could enable the study of topological many-body physics such as fractional quantum Hall systems. Therefore, it is of vital importance to understand the underlying heating mechanisms in order to find strategies to reduce this heating in future experiments.

In this thesis, we report on experimentally measured atom number losses from an interacting Bose-Einstein condensate in a periodically driven one-dimensional optical lattice. We systematically study the loss rates for different interaction strengths and shaking parameters. We focus our study on two different shaking regimes that are of experimental relevance: for driving frequencies that are larger than the bandwidth of the lowest band but still small compared to the resonance frequency to the first excited band, the tunneling matrix element between neighboring lattice sites is renormalized by a Bessel function. In the second regime, we study shaking frequencies that lie between the band gap of the first and second excited band. In this regime, the bands strongly hybridize with each other, which can lead to a double-well-like dispersion relation in the lowest band. While the former regime can be utilized to create artificial magnetic fields and topological band structures, the latter facilitates the study of symmetry-broken domains.

In addition to the experimental determination of heating rates, we develop a theoretical model that describes the underlying resonant scattering processes. Having identified the dominant scattering channels, we estimate the resulting heating rates of the system within a Fermi's golden rule approach. By comparing the measured heating rates with theory, we find that heating can be reduced when resonantly scattered particles are allowed to directly leave the trap before dissipating their energy into the system. In addition to the experiments conducted in a one-dimensional lattice, we also present preliminary data on heating rates in a driven hexagonal lattice. Since the heating mechanisms discussed in this thesis rely on at least one weakly confined transverse direction, a crucial step towards minimizing heating in driven lattice systems might be the implementation of shaking within a three-dimensional lattice structure.

Contents

Chapter 1

Introduction

Periodically driven systems can exhibit interesting and unintuitive phenomena not present in static systems. One paradigmatic example in classical physics is the so-called "Kapitza pendulum", a rigid pendulum whose pivot point allows for a periodical drive along the vertical direction [1, 2]. Without driving, the inverted position above the pivot point is an unstable equilibrium position. This implies that the smallest perturbation takes the system away from this position and induces oscillations of the pendulum. Once the oscillations damp out, the system relaxes to the stable equilibrium position below the pivot point. By carefully choosing the frequency and amplitude of the external drive, one can transform the inverted unstable equilibrium position into a stable one. Now, small displacements from this position will lead to slow oscillations of the pendulum's bob about this inverted position. Once these oscillations damp out, the pendulum will return to the inverted position. This system represents one kind of passive dynamical stabilization, where otherwise unstable modes can be stabilized by periodically driving the system.

In 1986, Dunlap and Kenkre introduced the concept of controlling a physical system through periodic driving to lattice structures [3]. They studied on a theoretical level how charged particles in a lattice structure behave in the presence of an external oscillating electric field. In a static system, initially localized particles spread out over the lattice with time. However, they showed that this spreading can be slowed down or even completely suppressed by applying a periodic drive with properly chosen driving parameters. As the particles can neither move nor spread and remain localized on a single lattice site this phenomenon was termed "dynamic localization". This effect is a quantum-mechanical version of the above-mentioned Kapitza pendulum which shows that time-periodic forcing can stabilize an otherwise unstable system.

Later theoretical studies showed that this dynamic localization of matter waves was associated with a suppression of Bloch bands [4–6]. While it was theoretically shown that this kind of dynamic stabilization also survives in real solid-state materials where Coulomb interactions between particles play a major role [7], the experimental observation proved to be challenging. By applying a terahertz electric field to a semiconductor superlattice, dynamic localization was indirectly observed

by measuring a suppressed conductance of the sample [8]. However, this experiment also had to handle a multitude of additional competing effects that occurred at the same time. While this experiment showed the suppression of inter-well tunneling events, it could not show the suppression of Bloch bands.

The advent of ultracold atoms trapped in crystals of light changed this situation dramatically. By loading a cold gas of sodium atoms into an optical lattice and periodically modulating its position, it was possible to directly observe a suppression of Bloch bands [9]. Subsequent studies involving a Bose-Einstein condensate (BEC) showed the dynamic localization of matter waves as well as the underlying mechanism responsible for dynamic localization, the rescaling of the tunneling matrix element by a Bessel function [10, 11].

This example illustrates that ultracold quantum gases trapped in optical lattices are a suitable system to simulate condensed matter systems. Compared to real solid state materials, ultracold quantum gases in optical lattices offer extremely clean potential landscapes combined with exceptional control possibilities over the system parameters [12, 13].

The rapid development of quantum simulation with ultracold atoms was made possible by the creation of the first gaseous BEC in 1995 [14–16] and the first degenerate Fermi gas in 1999 [17]. By loading ultracold atoms into an optical lattice created by the interference of multiple laser beams, the Hubbard model can be realized [18]. This model was initially designed to describe strongly-correlated electrons in condensed matter systems [19] and is characterized by two parameters, the tunnel coupling between neighboring lattice sites and the interaction strength between individual particles. Both of these parameters can be individually manipulated in ultracold quantum gas experiments with high precision. Interactions between atoms are typically tuned via Feshbach resonances [20] and the tunnel coupling can be tuned by changing the lattice depth. This tuning ability allowed optical lattice experiments to enter the strongly correlated regime, which led to the hallmark observation of the superfluid to Mott insulator transition in a three-dimensional optical lattice [21].

Many different lattice structures have been realized in the last decade, ranging from simple cubic lattices to more exotic lattice structures like the honeycomb and triangular lattice [22–24], the checkerboard lattice [25] or the Kagome lattice [26]. In addition to an extensive toolbox to manipulate the system, which even extends down to the single particle level [27], many different detection methods for the many-body state are also available. Besides the standard absorption and phase contrast imaging techniques [28], there are also noise correlation measurements [29, 30] and the imaging of both bosonic and fermionic atoms at the single-particle level available [31–37].

In recent years, the periodic modulation of optical lattice potentials became a versatile tool to probe and alter the band structure. Amplitude modulation of the lattice has mainly been used to probe nearest-neighbor correlations [38] or the ex-

citation spectrum of the system [39–41]. Other possibilities include photon-assisted tunneling [42] or algorithmic cooling of the system [43]. Although phase or frequency modulation of the lattice beams can, in principle, also be used for the same purposes discussed above, it has been particularly used to engineer novel band structures.

The effects of the spatial modulation of the lattice potential onto the band structure can be grouped into two experimentally relevant regimes. When shaking with a frequency close to the energy separation between two bands, the two bands start to hybridize. If bands with different curvature are hybridized [44], the resulting band structure can be exploited to study, for example, the formation of symmetry-broken domains [45, 46]. The other shaking regime is obtained for driving frequencies that are far above the bandwidth of the lowest band but which are still small compared to the separation of the lowest two bands. In this regime, the periodic driving renormalizes the tunneling matrix element by a Bessel function, as already mentioned above. It was shown that this renormalization remains effective even if the particles strongly interact with each other [47]. This tuning ability was later used to cross the superfluid to Mott insulator transition in a dynamic fashion [48].

Recently, periodic driving has also attracted attention as a possible candidate to implement artificial gauge fields in cold atoms systems. Many interesting effects in condensed matter physics, such as the quantum Hall effect [49], rely on charged particles interacting with magnetic fields via the Lorentz force. Since this interaction is absent in cold atom systems due to the charge-neutrality of the trapped atoms, there has been an increasing interest in engineering artificial magnetic or electric fields. In general, the effect of an external gauge potential on a charged particle confined in a lattice structure is captured by a complex tunneling phase, the so-called Peierls phase [50, 51]. This Peierls phase is given by the line integral of the gauge potential along a lattice bond and the resulting strength of the magnetic field is hence given by the integral of the Peierls phases over a single plaquette of the lattice. Therefore, the general strategy to implement artificial gauge fields in lattice systems is to create complex tunneling phases that lead to a non-trivial magnetic flux per plaquette.

By choosing an appropriate driving scheme, such complex tunneling phases can be imprinted. The trapped neutral particles then effectively behave like charged particles in the presence of an external magnetic field [52–54]. These complex tunneling phases do not have to be imprinted via spatial lattice shaking. Another technique exploited laser-assisted tunneling between neighboring lattice sites in order to create strong staggered and non-staggered magnetic fields [55–62]. In these schemes, tunneling between neighboring lattice sites is initially inhibited by employing a magnetic field gradient or a superlattice potential. Tunneling with the desired complex phases is then restored by driving the system with additional lasers at a frequency that is resonant to the energy offset between neighboring lattice sites.

Periodic driving has also been intensively discussed in the context of engineering topological band structures [52, 63–67]. By circularly driving a hexagonal lattice

it was possible to create a topological band structure [68, 69] which resembled the Haldane model [70]. This toy model demonstrated that the quantum Hall effect can occur in Bloch band structures even without the need of a strong external magnetic field if time-reversal symmetry is broken by other means.

Despite the many successes and promising future applications of shaken lattice systems, they are accompanied by their own set of challenges. One major issue of periodically driven systems, especially interacting ones, is that they exhibit considerable heating, which leads to a strong reduction of their lifetime. This behavior is rooted in a general property of periodically driven systems. As the system can absorb or emit energy from the drive, energy is not conserved anymore. In close analogy to particles in a spatially periodic potential, where the momentum is only defined modulo reciprocal lattice vectors, the energy of a driven system is only defined modulo the energy quantum $\hbar\omega$. Due to this lack of energy conservation, it is generally assumed that interacting driven systems heat up to an infinite temperature like state [71, 72].

As many physical effects require strong interactions between particles, as for example fractional quantum Hall states [73], it is desirable to combine periodically driven systems with strong interactions. However, to successfully combine these two properties, a thorough understanding of the underlying heating mechanisms is necessary because only then can strategies be developed in order to minimize heating of the system.

In this thesis, we study heating rates of an interacting BEC in a shaken one-dimensional optical lattice as a function of both driving and interaction strength. We choose this system due to its inherent simplicity. Apart from determining heating rates experimentally, we also develop a theoretical model that describes the dominant heating channels. This theoretical model is based on Fermi's golden rule, which was already studied in earlier theoretical work [74–78]. For the quantitative comparison between the theoretically estimated and experimentally measured heating rates, we choose two different driving frequencies which represent the two different driving regimes mentioned above. In the regime of low shaking frequencies, the dominant heating channels are given by resonant collision processes between two particles during which one- or two-photons from the drive are absorbed. For high shaking frequencies, the dominant heating channels are given by single-particle multiphoton excitations, where energy and momentum conservation is satisfied through a subsequent ordinary collision process between two particles. We find that the measured heating rates for low shaking frequencies are larger than the theoretically expected scattering rates. We attribute this discrepancy to secondary collision processes that occur when excited particles cannot directly leave the trap. One strategy to reduce heating in such a scenario would be to implement a trapping configuration where excited particles can directly leave the trap before dissipating their energy. Since the presented heating channels require at least one transverse direction, they should be forbidden in a three-dimensional lattice structure.

Outline

- **Chapter 2:** In this chapter, we review the basic theoretical knowledge necessary to understand ultracold atoms trapped in optical lattice structures and describe how the band energies and eigenstates of single particles can be obtained. In the last part of this chapter we review basic concepts of Floquet theory, such as the concept of quasienergy. In the course of this discussion we will give two explicit examples on how the band structure of a one-dimensional lattice changes under the influence of an external drive.

- **Chapter 3:** The experimental setup and the procedure to obtain a Bose-Einstein condensate of ^{39}K atoms are presented in this chapter. Furthermore, we discuss the utilized detection and manipulation techniques. In the last part of this chapter, we characterize relevant parameters of the system such as the total atom number and the momentum spread of the condensate.

- **Chapter 4:** In chapter 4 we present the general foundation of how heating rates in a shaken optical lattice can be obtained. In particular, we distinguish between single-particle heating and interaction-dependent heating. While single-particle heating only occurs at specific shaking frequencies when a multiphoton resonance condition to an excited band is fulfilled, interaction dependent heating occurs at all driving frequencies. We present a general theoretical model with which heating rates can be determined by Fermi's golden rule and where the density distribution of the atoms is considered within a local density approximation.

- **Chapter 5:** A quantitative comparison between the measured and estimated heating rates is presented for two different driving regimes. For frequencies larger than the bandwidth of the lowest band but still small compared to the band gap the dominant heating processes are given by resonant two-particle scattering. In the second driving regime where the shaking frequency is larger than the band gap a multitude of different scattering channels appear. In both regimes we find good agreement between the measured data and the theoretical estimation.

- **Chapter 6:** In chapter 6 we conclude this thesis and present future prospects of the experiment. Additionally, preliminary results on measured heating rates in a shaken hexagonal lattice are presented.

Publications

The main results of this thesis are published in the following paper:

- **Interaction dependent heating and atom loss in a periodically driven optical lattice.**
  Martin Reitter, Jakob Näger, Karen Wintersperger, Christoph Sträter, Immanuel Bloch, André Eckardt, Ulrich Schneider.
  Physical Review Letters 119, 200402 (2017)

Apart from this work I contributed to the following two publications which are not described in this thesis:

- **An Aharonov-Bohm interferometer for determining Bloch band topology.**
  Lucia Duca, Tracy Li, Martin Reitter, Immanuel Bloch, Monika Schleier-Smith, Ulrich Schneider.
  Science 347, 288-292 (2015).

- **Bloch state tomography using Wilson lines.**
  Tracy Li, Lucia Duca, Martin Reitter, Fabian Grusdt, Eugene Demler, Manuel Endres, Monika Schleier-Smith, Immanuel Bloch, Ulrich Schneider.
  Science 352, 1094-1097 (2016).

Chapter 2

Theoretical background

This chapter summarizes the most important theoretical concepts necessary to understand ultracold atoms in driven optical lattice systems. We start in section 2.1 by introducing Bose-Einstein condensation. In particular, we will focus on condensates trapped in a harmonic trapping potential. Afterwards, in section 2.2 we will describe how single particles behave in the presence of an external lattice structure. We will introduce the concept of energy bands and describe the single-particle wave function on a single lattice site. We focus our discussion on a one-dimensional optical lattice, as this lattice structure is used in most parts of this thesis. In addition, we also give a short introduction of the hexagonal lattice as we will also present some preliminary measurements in this lattice structure in section 6.1. We conclude this chapter with a description of Floquet theory in section 2.3.

2.1 Theory of ultracold bosonic particles

In this section, we will introduce the basic theoretical background necessary to understand ultracold bosonic gases. We will start with a brief introduction of Bose-Einstein condensation and will then discuss the Gross-Pitaevskii equation as this equation and derivations from it, like the Thomas-Fermi approximation, will play a central role in this thesis later on.

2.1.1 Bose-Einstein condensation

Bose-Einstein-condensation (BEC), the macroscopic occupation of a single eigenstate, was already predicted almost one hundred years ago [79, 80] after which it took 70 years until the first gaseous condensates were realized in the lab [14, 15]. For an ideal, non-interacting Bose gas the average occupation number of a single-particle eigenstate with energy ϵ_i is given by the Bose-Einstein distribution [81]

$$\bar{n}_i = \frac{1}{e^{(\epsilon_i - \mu)/(k_B T)} - 1}, \tag{2.1}$$

where μ is the chemical potential, k_B is Boltzmann's constant and T denotes the temperature of the system. Since the occupation number must have a positive value, Eq. 2.1 places a physical constraint on the chemical potential μ being smaller than the ground state energy of the system ϵ_0. Bose-Einstein condensation occurs in the limit where $\mu \to \epsilon_0$. In this regime, the ground state becomes macroscopically occupied by N_0 atoms

$$N_0 \equiv \frac{1}{e^{(\epsilon_0-\mu)/(k_BT)}-1}. \tag{2.2}$$

One can, therefore, express the total atom number of the system as the sum of atoms in the ground state and atoms occupying higher-lying energy states

$$N = N_0 + N_T, \tag{2.3}$$

where

$$N_T = \sum_{i\neq 0} \bar{n}_i(T,\mu) \tag{2.4}$$

is also referred to as the thermal background of the gas. For typical experiments the condensate will be trapped in an external harmonic potential whose energy levels are given by [82]

$$\epsilon_{n_x,n_y,n_z} = \hbar\omega_x\left(n_x+\frac{1}{2}\right) + \hbar\omega_y\left(n_y+\frac{1}{2}\right) + \hbar\omega_z\left(n_z+\frac{1}{2}\right), \tag{2.5}$$

where $\omega_{x,y,z}$ is the harmonic trapping frequency and $\hbar$ the reduced Planck constant. In the limit $\mu = \epsilon_0$[1] with large particle numbers and a harmonic oscillator level spacing much smaller than k_BT, one can replace the sum in Eq. 2.4 by an integral leading to

$$N_T = \int \mathrm{d}n_x \mathrm{d}n_y \mathrm{d}n_z \frac{1}{\exp[\beta\hbar(\omega_x n_x + \omega_y n_y + \omega_z n_z)]-1}, \tag{2.6}$$

where $\beta = 1/(k_BT)$ is the inverse temperature. The critical temperature below which a macroscopic occupation of the ground state occurs can be obtained by equating N_T with N and is given by [83]

$$k_BT_c = \hbar\bar{\omega}\left(\frac{N}{\zeta(3)}\right)^{1/3}. \tag{2.7}$$

[1] If the temperature is larger than the critical temperature T_c at which Bose-Einstein condensation occurs, this equation cannot be fulfilled without violating the normalization condition that $N_T \leq N$. Hence, for temperatures larger than T_c the lowest energy state is only occupied microscopically with a negligible contribution to the thermodynamic properties of the system.

Here $\bar{\omega} = (\omega_x \omega_y \omega_z)^{1/3}$ is the geometric mean of the trapping frequencies and $\zeta(x)$ is the Riemann function. Depending on the temperature of the system, only a fraction of atoms condense into the lowest energy state. We can express this condensate fraction N_0/N in terms of the temperature as

$$\frac{N_0}{N} = 1 - \left(\frac{T}{T_c}\right)^3 . \tag{2.8}$$

In the case of an ideal condensate at zero temperature, all atoms occupy the lowest energy state which for an external harmonic oscillator potential is the harmonic oscillator ground state wave function $\phi_0(\boldsymbol{r})$. Thus, the density distribution $n_0(\boldsymbol{r})$ of the condensate can be described by

$$n_0(\boldsymbol{r}) = N_0 \left|\phi_0(\boldsymbol{r})\right|^2 . \tag{2.9}$$

2.1.2 The Gross-Pitaevskii equation

So far we have assumed an ideal, non-interacting Bose gas. However, a generic bosonic quantum system will exhibit finite interactions between its particles. We can describe such an interacting many-body system that is additionally confined by an external potential $V(\boldsymbol{r})$, within second quantization by the Hamiltonian [84]

$$\begin{aligned} \hat{H} &= \int \mathrm{d}\boldsymbol{r} \hat{\Psi}^\dagger(\boldsymbol{r}) \left[-\frac{\hbar^2}{2M}\nabla^2 + V(\boldsymbol{r})\right] \hat{\Psi}(\boldsymbol{r}) \\ &\quad + \frac{1}{2}\int \mathrm{d}\boldsymbol{r}\mathrm{d}\boldsymbol{r}' \hat{\Psi}^\dagger(\boldsymbol{r})\hat{\Psi}^\dagger(\boldsymbol{r}') U_{\mathrm{int}}(\boldsymbol{r}-\boldsymbol{r}')\hat{\Psi}(\boldsymbol{r}')\hat{\Psi}(\boldsymbol{r}). \end{aligned} \tag{2.10}$$

Here M is the mass of the atoms and $\hat{\Psi}^\dagger(\boldsymbol{r})$ and $\hat{\Psi}(\boldsymbol{r})$ denote the bosonic field operators that create or annihilate a particle at position $\boldsymbol{r}$, respectively. The interaction potential between two particles is given by $U_{\mathrm{int}}(\boldsymbol{r}-\boldsymbol{r}')$. The exact solution of this Hamiltonian is generally not possible, especially for systems that contain a large number of atoms, which is usually the case when studying condensates. To simplify the Hamiltonian defined in Eq. 2.10, we perform a mean-field approximation. Since a single eigenstate becomes macroscopically occupied in a condensate, the field operators can be expressed as

$$\hat{\Psi}(\boldsymbol{r},t) = \Phi(\boldsymbol{r},t) + \hat{\Psi}'(\boldsymbol{r},t), \tag{2.11}$$

where $\Phi(\boldsymbol{r},t) \equiv \langle\hat{\Psi}(\boldsymbol{r},t)\rangle$ is the expectation value of the field operator. Within this approximation, the condensate density $n_0(\boldsymbol{r},t)$ is given by $n_0(\boldsymbol{r},t) = |\Phi(\boldsymbol{r},t)|^2$. The operator $\hat{\Psi}'(\boldsymbol{r},t)$ describes small fluctuations of the condensate density and will be neglected in the following.

At the ultracold temperatures present in a BEC, the mean inter-particle distance in the condensate as well as the de Broglie wavelength of the atoms are much larger than the range of interactions between particles, which are described by the van der Waals force [85, 86]. Furthermore, due to the low energy of the atoms, only s-wave scattering between particles has to be taken into account. With all these considerations, we can approximate the interaction potential by a contact interaction potential

$$U_{\text{int}}(\boldsymbol{r} - \boldsymbol{r}') \approx g\delta(\boldsymbol{r} - \boldsymbol{r}'), \tag{2.12}$$

where $g = 4\pi\hbar^2 a/M$ and a is the s-wave scattering length and $\delta(\boldsymbol{r})$ is the Dirac delta function.

Inserting these approximations into Eq. 2.10 we arrive at the Gross-Pitaevskii equation [87]

$$i\hbar\frac{\partial}{\partial t}\Phi(\boldsymbol{r},t) = \left(-\frac{\hbar^2\nabla^2}{2M} + V(\boldsymbol{r}) + g\left|\Phi(\boldsymbol{r},t)\right|^2\right)\Phi(\boldsymbol{r},t). \tag{2.13}$$

This equation is a non-linear partial differential equation which is generally difficult to solve. By choosing the stationary state of the condensate wave function to be given by $\Phi(\boldsymbol{r},t) = \phi(\boldsymbol{r})\exp(-i\mu t/\hbar)$ [81], we can remove the time dependence of the Gross-Pitaevskii equation. Inserting this condensate wave function which is also called the order parameter into Eq. 2.13, we obtain the time-independent Gross-Pitaevskii equation

$$\left(-\frac{\hbar^2\nabla^2}{2M} + V(\boldsymbol{r}) + g\left|\phi(\boldsymbol{r})\right|^2\right)\phi(\boldsymbol{r}) = \mu\phi(\boldsymbol{r}). \tag{2.14}$$

2.1.3 Thomas-Fermi approximation

The Gross-Pitaevskii equation defined in Eq. 2.14 is still a non-linear Schrödinger equation, which generally has to be solved numerically. However, in the presence of an external trap and repulsive interactions, the problem can be further simplified, and an analytic solution is available. Let us, for simplicity, consider a three-dimensional symmetric harmonic oscillator potential

$$V(\boldsymbol{r}) = \frac{1}{2}M\omega^2 r^2, \tag{2.15}$$

in which a BEC of spatial extent R is trapped. For non-interacting particles, the typical cloud size would be given by the harmonic oscillator length [87]

$$R = r_{ho} = \sqrt{\frac{\hbar}{M\omega}}. \tag{2.16}$$

Furthermore, the density of particles in a condensate is proportional to $n \propto N/R^3$ leading to an interaction energy per particle of gN/R^3. In the case of repulsive interactions both the kinetic energy term and the interaction energy term in Eq. 2.14 try to increase the cloud size whereas the potential energy term tries to reduce it. Since both the kinetic energy term and the interaction term act in the same direction, we can neglect one of them if one is much larger than the other. From the relationship between the two terms which is proportional to [84]

$$\frac{E_{int}}{E_{kin}} \propto \frac{Na}{r_{ho}}, \tag{2.17}$$

we find that the kinetic energy term can be neglected if $Na \gg r_{ho}$. This condition is usually fulfilled for condensates with a large atom number N and a non-vanishing scattering length[2]. With all these considerations we arrive at the so-called Thomas-Fermi approximation

$$\left(V(\boldsymbol{r}) + g\left|\phi(\boldsymbol{r})\right|^2\right)\phi(\boldsymbol{r}) = \mu\phi(\boldsymbol{r}). \tag{2.18}$$

The solution of this equation is given by

$$\left|\phi(\boldsymbol{r})\right|^2 = n_0(\boldsymbol{r}) = \begin{cases} \frac{\mu - V(\boldsymbol{r})}{g} & \text{where } V(\boldsymbol{r}) < \mu \\ 0 & \text{elsewhere.} \end{cases} \tag{2.19}$$

The density profile of the cloud along the axes of the harmonic trapping potential is thus given by an inverted parabola. The radius at which the density of the condensate vanishes is called the Thomas-Fermi radius and is given by

$$R_{TF} = \sqrt{\frac{2\mu}{M\omega^2}}. \tag{2.20}$$

In general, the harmonic trapping potential is not isotropic and is given by

$$V(\boldsymbol{r}) = \frac{1}{2}M\left(\omega_x^2 x^2 + \omega_y^2 y^2 + \omega_z^2 z^2\right). \tag{2.21}$$

Inserting this trapping potential into Eq. 2.19, we can express the total number of condensed atoms N_0 as

[2] In our experiment, this fraction between interaction and kinetic energy is between approximately 150 and 1200 depending on which scattering length is used.

$$\begin{aligned} N_0 &= \int \mathrm{d}\boldsymbol{r}\, n_0(\boldsymbol{r}) \\ &= \frac{\mu}{g}\left(\frac{2\mu}{M\bar{\omega}^2}\right)^{3/2} \underbrace{\int_{|\tilde{\boldsymbol{r}}|\leq 1} \mathrm{d}\tilde{\boldsymbol{r}}\,[1-\tilde{\boldsymbol{r}}^2]}_{8\pi/15}, \end{aligned} \tag{2.22}$$

where $\tilde{\boldsymbol{r}} = (\tilde{x}, \tilde{y}, \tilde{z})$, with $\tilde{x}^2 = M\omega_x^2 x^2/(2\mu)$ and likewise expressions for $\tilde{y}$ and $\tilde{z}$. Solving Eq. 2.22 for μ we obtain

$$\mu = \frac{\hbar\bar{\omega}}{2}\left(\frac{15N_0 a}{\bar{r}_{ho}}\right)^{2/5}, \tag{2.23}$$

where $\bar{r}_{ho} = \sqrt{\hbar/(M\bar{\omega})}$. By inserting Eq. 2.23 into Eq. 2.20 we obtain expressions for the Thomas-Fermi radii along all three trapping directions

$$R_{TF}^i = \left(15N_0 a\frac{\hbar^2\bar{\omega}^3}{M^2\omega_i^5}\right)^{1/5}, \quad i = x, y, z. \tag{2.24}$$

This expression will play a central part in the determination of the total atom number of our system, see section 3.4.2.

2.2 Ultracold atoms in lattice structures

In this section, we briefly review the single-particle eigenstates and energy bands in different lattice structures. At first, we will discuss the one-dimensional lattice as most experiments described in this thesis will be conducted in this lattice structure due to its inherent simplicity. Afterwards, we will apply the presented techniques to a hexagonal lattice structure.

2.2.1 Bloch waves and band structure of a 1D lattice

To derive the eigenstates and eigenenergies of particles in a one-dimensional lattice structure, we will neglect interactions between them. This approximation is justifiable since the typical interaction energies between particles are weak compared to the natural energy scales of the lattice in our system. To further simplify the system we will assume a homogeneous lattice structure. Within these approximations, the system is described by the following Schrödinger equation:

$$\hat{H}\phi_q^{(b)}(x) = E_q^{(b)}\phi_q^{(b)}(x) \quad \text{with} \quad \hat{H} = \frac{\hat{p}^2}{2M} + V_L(x), \tag{2.25}$$

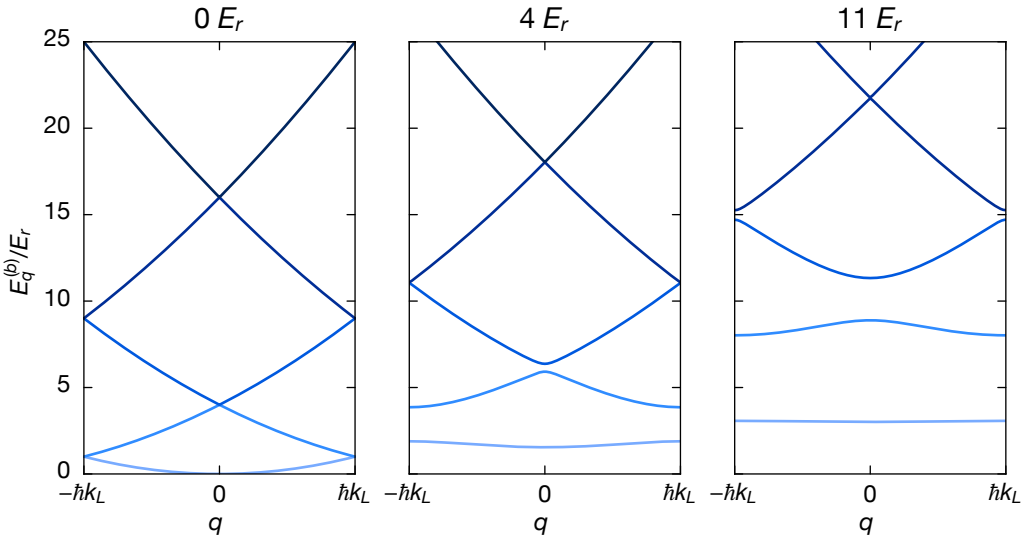

Figure 2.1: **Bandstructure of a one dimensional lattice.** The plots show the eigenenergies $E_q^{(b)}$ of the Bloch states for different quasimomenta q within the first Brillouin zone for various lattice depths.

where $\hat{p} = -i\hbar\partial/\partial x$ is the momentum operator and $V_L(x) = V_0 \cos^2(k_L x)$ describes the lattice potential with lattice depth V_0 and wave number k_L. According to Bloch's theorem [88], the eigenstates of this Hamiltonian read:

$$\phi_q^{(b)}(x) = e^{iqx/\hbar} u_q^{(b)}(x). \tag{2.26}$$

These so-called Bloch functions are plane waves multiplied by a periodic function $u_q^{(b)}(x)$, whose periodicity is the same as the lattice potential. Due to the periodic structure of $u_q^{(b)}(x)$ and $V_L(x)$, we can express them as discrete Fourier sums

$$V_L(x) = \sum_m V_m e^{2ik_L mx} \quad \text{and} \quad u_q^{(b)}(x) = \sum_n c_n^{(b,q)} e^{2ik_L nx}, \tag{2.27}$$

where m, n are integer numbers. By inserting the expansion of $u_q^{(b)}(x)$ into Eq. 2.26, we find that the new wave numbers $q/\hbar + 2k_L n$, of the Bloch functions are periodic with a periodicity of $2k_L$. Due to this periodicity, we can restrict the quasimomentum q to the first Brillouin zone, which is defined as the interval $]-\hbar k_L, \hbar k_L]$. The Fourier expansion of the lattice potential $V_L(x)$ is given by

$$V_L(x) = \frac{1}{4} V_0 \left(e^{2ik_L x} + e^{-2ik_L x} + 2 \right). \tag{2.28}$$

Inserting the obtained Fourier sums of $V_L(x)$ and $\phi_q^{(b)}(x)$ into Eq. 2.25, we can express this equation in matrix form as:

$$\sum_{n'} H_{n,n'} c_{n'}^{(b,q)} = E_q^{(b)} c_n^{(b,q)} \quad \text{with} \quad H_{n,n'} = \begin{cases} (2n + \frac{q}{\hbar k_L})^2 E_r + V_0/2 & \text{if } |n - n'| = 0 \\ V_0/4 & \text{if } |n - n'| = 1 \\ 0 & \text{otherwise.} \end{cases} \tag{2.29}$$

Here we have introduced the recoil energy E_r, the natural unit of the lattice depth V_0, which is defined as

$$E_r = \frac{\hbar^2 k_L^2}{2M}. \tag{2.30}$$

The eigenenergies $E_q^{(b)}$ and eigenvectors $c_n^{(b,q)}$ can be determined by numerically diagonalizing the Hamiltonian $H_{n,n'}$. To make the numerical evaluation of the Hamiltonian tractable, we have to truncate the size of the matrix. As we are only interested in the lowest three bands of the lattice, we restrict $|n| \leq 12$[3]. Figure 2.1 shows the numerically calculated eigenenergies $E_q^{(b)}$ for three different lattice depths V_0. For a vanishing lattice depth, the eigenenergies simply correspond to the quadratic dispersion relation of free particles reduced to the first Brillouin zone. Upon increasing the lattice depth, gaps open up between the bands and the bandwidth of the individual bands decrease. For very deep lattices the lowest bands become almost flat, and their energy spacing is given by the harmonic oscillator spacing $\hbar\omega_{\text{on-site}}$. Here $\omega_{\text{on-site}}$ describes the on-site frequency for a harmonic approximation of each lattice well.

By inserting the eigenvectors $c_n^{(b,q)}$ obtained from the numerical diagonalization of the Hamiltonian $H_{n,n'}$ into Eq. 2.27 and Eq. 2.26, we can determine the Bloch wave functions. Figure 2.2 (a) shows the obtained Bloch function of the lowest band, in a $11\,E_r$ deep lattice, for two different quasimomenta $q = 0$ and $q = \pm\hbar k_L$. While the Bloch function in the center of the Brillouin zone at $q = 0$ is symmetric, the one at the zone edges at $q = \pm\hbar k_L$ is antisymmetric. Figure 2.2 (b) shows the probability densities $|\phi_q^{(0)}(x)|^2$ of these two Bloch functions together with a sketch of the lattice potential.

2.2.2 Wannier functions of a 1D lattice

To describe interactions between particles on a single lattice site, as will become relevant later on, the Bloch waves introduced in section 2.2.1 are not the best choice

[3] In principle, the numerical diagonalization of a Hamiltonian with matrix entries up to an index $|n| \leq n_{\max}$ yield results for the first $2n_{\max}$ bands. The result, however, is most accurate only for the lowest energy bands.

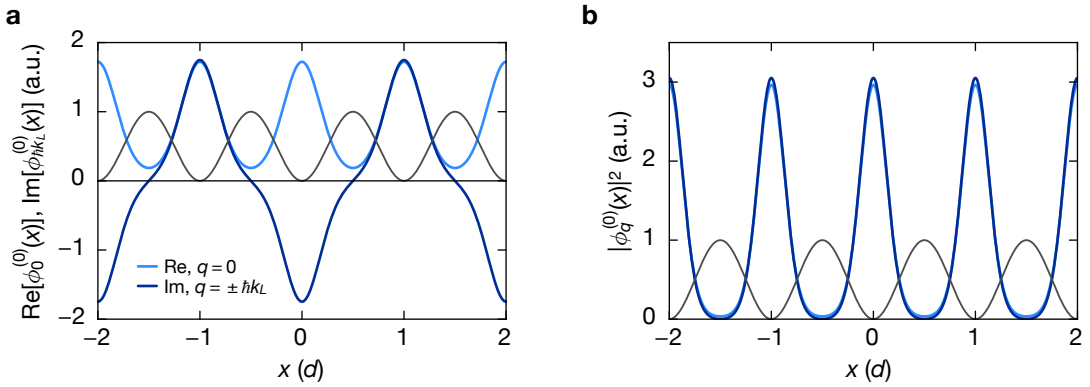

Figure 2.2: **Bloch functions of a one dimensional lattice. (a)** Bloch functions of the lowest band ($b = 0$) at $q = 0$ (light blue) and at $q = \pm\hbar k_L$ (dark blue) of an $11E_r$ deep lattice. The gray line illustrates the lattice potential. **(b)** Probability densities at $q = 0$ (light blue) and at $q = \pm\hbar k_L$ (dark blue).

since they are completely delocalized. For such a task it is more convenient to use an orthonormal basis set of wavefunctions that are localized to individual lattice sites. The maximally localized Wannier functions form such a basis set. A single localized particle on lattice site i in the bth band of the lattice can be described by its Wannier function [88]

$$w_b(x - x_i) = \frac{1}{\sqrt{\mathcal{N}}} \sum_q e^{-iqx_i/\hbar} \phi_q^{(b)}(x), \tag{2.31}$$

where the sum runs over all quasimomenta of the first Brillouin zone. Here the position of the i^{th} lattice site is given by x_i and $\mathcal{N}$ describes a normalization constant. Figure 2.3 shows Wannier functions at two different lattice depths. Particularly for the lower lattice depth one can see that the Wannier function has finite values at neighboring lattice sites. This means that there is a finite probability to find the particle on a neighboring lattice site which results in a finite value of the tunnel coupling between these lattice sites. This tunneling between neighboring lattice sites i and j can be described by the tunneling matrix element J_b which is given by

$$J_b = \int w_b(x - x_i) \left(-\frac{\hbar^2}{2M} \frac{\partial^2}{\partial x^2} + V_L(x) \right) w_b(x - x_j) \mathrm{d}x. \tag{2.32}$$

Within the Wannier basis, we can describe the interaction matrix element between two particles on the same lattice site by

$$U_{\text{int}} = \frac{4\pi\hbar^2 a}{M} \int |w_0(x)|^4 \, \mathrm{d}x. \tag{2.33}$$

Here we have assumed that both particles are in the lowest band of the lattice.

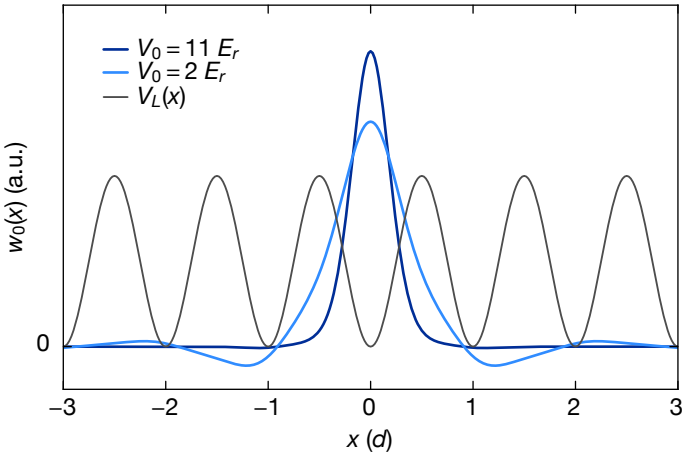

Figure 2.3: **Wannier functions of lowest band.** Wannier function $w_0(x)$ of the lowest band for two different lattice depths of $V_0 = 11E_r$ (dark blue) and $V_0 = 2E_r$ (light blue). The lattice potential is illustrated in gray. For deeper lattices, the Wannier functions become more and more localized on a single lattice site leading to smaller tunneling matrix elements J_b.

2.2.3 Tight-binding limit

For deep lattices, the tunneling matrix element between neighboring lattice sites becomes dominant and one can neglect tunneling events over larger distances than one lattice site. This approximation is called the tight-binding approximation. In a one-dimensional lattice it becomes valid for lattice depths that are deeper than approximately $5E_r$. At this lattice depth, the next-nearest tunneling element becomes one order of magnitude smaller than the nearest-neighbor tunneling matrix element. Within the tight-binding approximation, the dispersion relation of the lowest band is described by [87]

$$E^{(0)}(q) = -2J_0 \cos(dq), \tag{2.34}$$

where d is the lattice spacing. The corresponding bandwidth of the lowest band is thus given by $4J_0$.

2.2.4 The honeycomb lattice

Although most experimental results in this thesis are obtained in a one-dimensional lattice, the honeycomb lattice plays an important role in balancing the lattice beams, see section 3.3.3. Furthermore, as the honeycomb lattice is the predominantly used lattice structure in our lab so far, it will most likely be used for subsequent experiments that combine lattice shaking with this band structure. To this end, we have

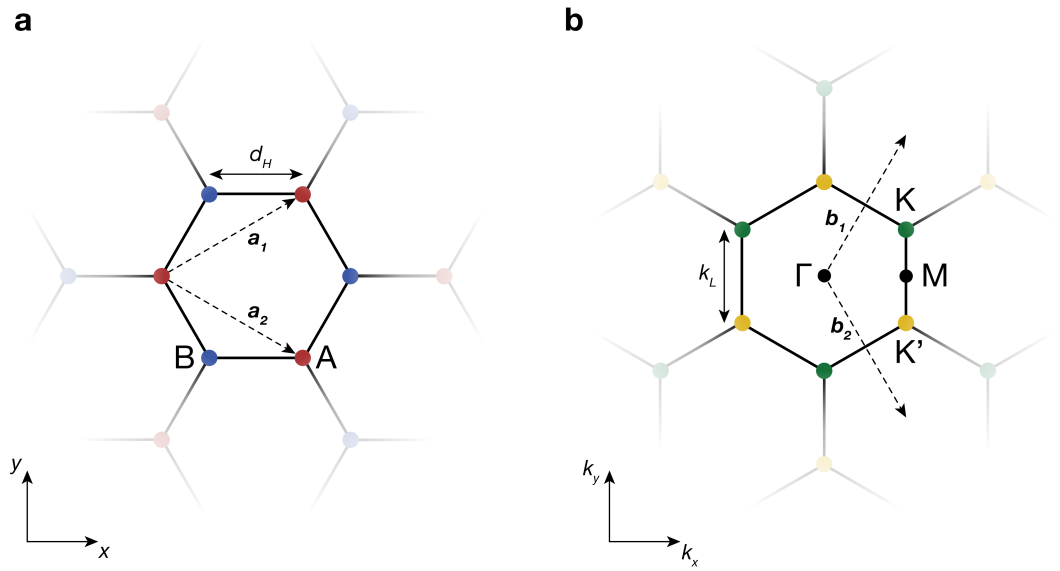

Figure 2.4: **Honeycomb lattice in real space and reciprocal space.** **(a)** Honeycomb lattice in real space. The lattice is comprised out of two triangular Bravais lattices A and B with lattice sites marked by red and blue dots, respectively. The distance between neighboring lattice sites of the A and B sublattice is given by d_H. The primitive lattice vectors $\boldsymbol{a}_1$ and $\boldsymbol{a}_2$ are chosen to connect the lattice sites of the A sublattice. **(b)** Honeycomb lattice in reciprocal space. The high symmetry points Γ and M are indicated by black dots whereas the K and K' points are indicated by green and yellow dots, respectively, to emphasize their inequality. The primitive reciprocal lattice vectors $\boldsymbol{b}_1$ and $\boldsymbol{b}_2$ span the Brillouin zone.

already obtained preliminary measurements of heating rates in a shaken honeycomb lattice, which can be found in section 6.1. As the honeycomb lattice plays only a minor role in this thesis, we will only give a short introduction of the most important parts of the band structure of the honeycomb lattice. Further information, especially about the geometric and topological properties of the hexagonal lattice can be found in references [89, 90] and references therein.

Compared to the one-dimensional lattice, the honeycomb lattice is a two-dimensional lattice. Its real space and momentum space structure are illustrated in Fig. 2.4. One particularly interesting feature of the honeycomb lattice is that it is comprised out of two triangular sublattices with lattice sites A and B. The primitive lattice vectors which are chosen to connect the A sites of the lattice are defined as

$$\begin{aligned} \boldsymbol{a}_1 &= \frac{d_H}{2}\left(3, \sqrt{3}\right) \\ \boldsymbol{a}_2 &= \frac{d_H}{2}\left(3, -\sqrt{3}\right), \end{aligned} \tag{2.35}$$

where d_H is the distance between neighboring A and B sites. The associated reciprocal lattice is illustrated in Fig. 2.4 (b) and has the same honeycomb like structure as the real space lattice. The reciprocal lattice vectors $\boldsymbol{b}_i$ in momentum space are related to the real space vectors $\boldsymbol{a}_i$ via the relation $\boldsymbol{a}_i \cdot \boldsymbol{b}_j = 2\pi\delta_{ij}$ [91], where δ_{ij} is the Kronecker delta, and are given by

$$\begin{aligned} \boldsymbol{b}_1 &= \frac{2\pi}{3d_H}\left(1, \sqrt{3}\right) \\ \boldsymbol{b}_2 &= \frac{2\pi}{3d_H}\left(1, -\sqrt{3}\right). \end{aligned} \tag{2.36}$$

There are multiple high symmetry points associated with this lattice structure, of which we will mention the most relevant ones to us. The center of the Brillouin zone is referred to as the Γ point and the corners of the Brillouin zone are labeled the K and K' points. Note that K and K' are inequivalent since they cannot be connected by a reciprocal lattice vector. The center point between the K and K' point on the edge of the Brillouin zone is labeled the M point.

A hexagonal lattice structure can experimentally be realized by interfering three running-wave laser beams that intersect each other at an angle of 120°, for further details see section 3.1.4. The resulting lattice potential is described by

$$\begin{aligned} V_L(\boldsymbol{r}) &= V_1 + V_2 + V_3 + 2\sqrt{V_1 V_2}\cos((\boldsymbol{b}_1 - \boldsymbol{b}_2)\boldsymbol{r}) \\ &+ 2\sqrt{V_1 V_3}\cos(\boldsymbol{b}_2\boldsymbol{r}) + 2\sqrt{V_2 V_3}\cos(\boldsymbol{b}_1\boldsymbol{r}). \end{aligned} \tag{2.37}$$

Here $V_{1,2,3}$ are the AC Stark shifts[4] created by the individual laser beams with wave-vectors

$$\boldsymbol{k}_1 = k_L(0,1) \tag{2.38}$$

$$\boldsymbol{k}_2 = k_L\left(-\frac{\sqrt{3}}{2}, -\frac{1}{2}\right) \tag{2.39}$$

$$\boldsymbol{k}_3 = k_L\left(\frac{\sqrt{3}}{2}, -\frac{1}{2}\right), \tag{2.40}$$

where $k_L = 2\pi/\lambda$ and λ is the wavelength of the laser. The primitive reciprocal lattice vectors $\boldsymbol{b}_1$ and $\boldsymbol{b}_2$ can be expressed in terms of the wave-vectors as [92]

$$\boldsymbol{b}_1 \equiv \boldsymbol{k}_1 - \boldsymbol{k}_2 = k_L\left(\frac{\sqrt{3}}{2}, \frac{3}{2}\right) \tag{2.41}$$

$$\boldsymbol{b}_2 \equiv \boldsymbol{k}_3 - \boldsymbol{k}_1 = k_L\left(\frac{\sqrt{3}}{2}, -\frac{3}{2}\right). \tag{2.42}$$

In order to calculate the band structure of the honeycomb lattice, we follow the same route as described in section 2.2.1. As for the 1D lattice we Fourier expand the honeycomb potential

$$V_L(\boldsymbol{r}) = \sum_{\boldsymbol{K}} V_{\boldsymbol{K}} e^{i\boldsymbol{K}\cdot\boldsymbol{r}}, \tag{2.43}$$

where the summation runs over all reciprocal lattice vectors $\boldsymbol{K}$, which themselves are a linear combination of the primitive reciprocal lattice vectors $\boldsymbol{b}_1$ and $\boldsymbol{b}_2$:

$$\boldsymbol{K} = l_1\boldsymbol{b}_1 + l_2\boldsymbol{b}_2, \tag{2.44}$$

with integers l_1 and l_2. From Eq. 2.37 one can see that only linear combinations of $l_{1,2} = 0, \pm 1$ result in nonzero Fourier components. The Bloch wave function is still defined according to Eq. 2.26, but due to the two-dimensionality of the honeycomb potential the scalar x has to be replaced by a vector $\boldsymbol{r}$. The lattice periodic part $u_{\boldsymbol{q}}^{(b)}(\boldsymbol{r})$ of the Bloch wave function then becomes

$$u_{\boldsymbol{q}}^{(b)}(\boldsymbol{r}) = \sum_{\boldsymbol{K'}} c_{\boldsymbol{K'}}^{(b,\boldsymbol{q})} e^{i\boldsymbol{K'}\boldsymbol{r}}. \tag{2.45}$$

[4]The explanation on the origin of this potential is described in section 3.1.1.

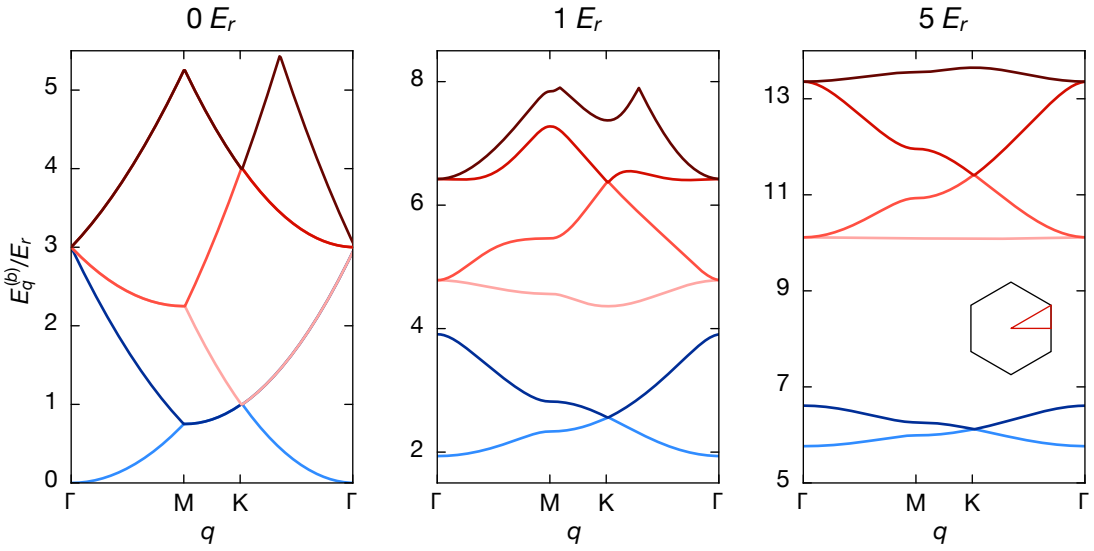

Figure 2.5: **Band structure of the honeycomb lattice.** Eigenenergies $E_q^{(b)}$ of the lowest six bands of the honeycomb lattice, for different lattice depths. The band energies are plotted along the high symmetry path $\boldsymbol{q} = \Gamma \to \mathrm{M} \to \mathrm{K} \to \Gamma$, illustrated by the red triangle in the inset of the right plot. The s-bands are illustrated in blue and the p-bands in red.

By inserting the obtained Fourier sums into Eq. 2.25, the Hamiltonian $\hat{H}$ can, in close similarity to the one-dimensional lattice, be written down in matrix form as

$$H_{\boldsymbol{K},\boldsymbol{K'}} = \begin{cases} \left(\frac{\boldsymbol{q}}{\hbar k_L} + l_1\boldsymbol{b}_1 + l_2\boldsymbol{b}_2\right)^2 E_r + 3V_0 & \text{if } l_1 = l_1' \text{ and } l_2 = l_2' \\ V_0 & \text{if } |l_1 - l_1'| = 1 \text{ and } l_2 = l_2' \\ V_0 & \text{if } |l_2 - l_2'| = 1 \text{ and } l_1 = l_1' \\ V_0 & \text{if } l_1 - l_1' = 1 \text{ and } l_2 - l_2' = 1 \\ V_0 & \text{if } l_1 - l_1' = -1 \text{ and } l_2 - l_2' = -1 \\ 0 & \text{else.} \end{cases} \tag{2.46}$$

This matrix can be solved numerically by truncating it at a maximum $l_{\max}$, such that $-l_{\max} \leq l_1, l_2 \leq l_{\max}$. With a matrix of the size $l_{\max}$, the eigenenergies of the lowest $(2l_{\max}+1)^2$ bands can be calculated. Since we are again mostly interested in the lowest bands we restrict ourselves to $l_{\max} = 6$.

Fig. 2.5 shows the energies of the lowest six bands along the high symmetry path from Γ to M to K and back to Γ. Let us first focus on the lowest two bands shown in blue. These bands always touch each other at the K and K' points. Due to the linear dispersion relation around them, they are also referred to as Dirac points [93].

Their presence is protected by inversion, time-reversal and C_3 symmetries of the lattice which means that the Dirac points must be present at the K and K' points even for very shallow lattice depths [94, 95]. The bandwidth of the lowest two bands decreases with increasing lattice depth, but contrary to the findings in a one-dimensional optical lattice the separation between the two bands decreases. This can be understood from the unit cell of the honeycomb lattice. Compared to the 1D case each unit cell contains two lattice sites which results in a splitting of each band into two bands. Let us now focus on the group of the four red bands of Fig. 2.5. From the two atomic unit cell one expects the excited band to split as discussed already for the lowest band. Due to the two-dimensionality of the honeycomb lattice each lattice site can be expanded by a 2D isotropic harmonic oscillator potential. For the harmonic oscillator potential, the first excited band is two-fold degenerate (the third band is three-fold degenerate and so on) [82]. Therefore, the first excited band manifold is split into a total of four individual bands. These bands are called the p-bands in analogy to atomic orbitals. The two lowest bands are hence referred to as the s-bands.

2.3 Floquet theory

In this section, we will discuss general properties and peculiarities of time-periodic Hamiltonians. We will show that the eigenenergies in such a driven system are not uniquely defined anymore, which will, later on, be the central element of our discussion of heating rates in driven optical lattices. Furthermore, we will show that the time evolution of a state under the influence of a time-periodic Hamiltonian can be determined by a time-independent Hamiltonian, the so-called Floquet Hamiltonian if we look at the state evolution in a stroboscopic way. In the last part of this section, we will give specific examples on how the driving alters the band structure of a one-dimensional lattice. This chapter closely follows the ideas and nomenclature presented in reference [96].

2.3.1 General properties of time-periodic Hamiltonians

Let us consider a system that is described by a time-periodic Hamiltonian $\hat{H}(t) = \hat{H}(t+T)$, with period T. According to the Floquet theorem the solutions of the time-dependent Schrödinger equation

$$i\hbar\frac{\partial}{\partial t}\left|\psi(t)\right\rangle = \hat{H}(t)\left|\psi(t)\right\rangle \tag{2.47}$$

are the so-called Floquet states [97–99]

$$\left|\psi_n(t)\right\rangle = e^{-i\varepsilon_n t/\hbar}\left|u_n(t)\right\rangle . \tag{2.48}$$

Here, the Floquet modes $|u_n(t)\rangle$ have the same time periodicity as the time-dependent Hamiltonian $\hat{H}(t)$. This structure of the Floquet state shows close similarities to the Bloch states introduced in Eq. 2.26, which are periodic in space compared to the here described periodicity in time. By inserting the Floquet state defined in Eq. 2.48 into the Schrödinger equation one obtains the equation

$$\hat{Q}(t)\,|u_n(t)\rangle = \varepsilon_n\,|u_n(t)\rangle\,. \tag{2.49}$$

Here we have introduced the quasienergy operator $\hat{Q}(t) = \hat{H}(t) - i\hbar\frac{\partial}{\partial t}$.[5] The eigenenergies ε_n determined by the solutions of Eq. 2.49 are, however, not uniquely defined. This becomes evident when multiplying a global phase term to the Floquet modes, such that

$$|u_{n,m}(t)\rangle \equiv e^{-im\omega t}\,|u_n(t)\rangle \quad \text{with} \quad m \in \mathbb{Z}. \tag{2.50}$$

Here $\omega = 2\pi/T$ denotes the frequency of the system. Inserting this expression into Eq. 2.49 the new eigenenergies are given by

$$\varepsilon_{n,m} = \varepsilon_n + m\hbar\omega. \tag{2.51}$$

However, the corresponding Floquet state does not alter by this transformation since

$$|\psi_{n,m}(t)\rangle = e^{-i\varepsilon_{n,m}t/\hbar}\,|u_{n,m}(t)\rangle = e^{-i\varepsilon_n t/\hbar}\,|u_n(t)\rangle = |\psi_n(t)\rangle\,, \tag{2.52}$$

and hence all solutions given by Eqs. (2.50) and (2.51) are physically equivalent. Because of this property, the eigenenergies ε_n are only defined modulo $\hbar\omega$ and are thus termed quasienergies. Another consequence of this periodicity in quasienergy is that the spectrum of the quasienergy operator is comprised of an infinite number of bands extending towards positive and negative quasienergies. In close analogy to the Brillouin zone introduced in section 2.2.1, we can restrict the quasienergies to lie within the "Floquet zone" $]-\hbar\omega/2, \hbar\omega/2]$.

2.3.2 Time-independent treatment of the quasienergy operator

The quasienergy operator as well as the Floquet modes, introduced in the previous section, still carry a time dependence. However, we can get rid of these time dependencies by extending the Hilbert space to $\mathcal{F} = \mathcal{H} \otimes \mathcal{T}$ [100]. Here $\mathcal{H}$ represents the physical state space and $\mathcal{T}$ the space of time-periodic, complex-valued functions with period T. We shall refer to this new Hilbert space $\mathcal{F}$ as the Floquet space. The scalar product in this new Floquet space is defined by the time-averaged scalar product of $\mathcal{H}$ and reads

[5] This Hamiltonian is sometimes referred to as the Floquet Hamiltonian in the literature.

$$\langle\langle u|v\rangle\rangle = \frac{1}{T}\int_0^T \mathrm{d}t\, \langle u(t)|v(t)\rangle\,. \tag{2.53}$$

States that are an element of $\mathcal{F}$ are indicated by a double ket $|u\rangle\rangle$, whereas the corresponding state at time t in $\mathcal{H}$ is denoted by $|u(t)\rangle$. Furthermore, we will mark operators that act in $\mathcal{F}$ by an overbar, to be able to distinguish them from operators that act in $\mathcal{H}$. The orthogonal basis states $|\alpha m\rangle\rangle$ of $\mathcal{F}$ can be constructed from time-periodic states $|\alpha\rangle\, e^{im\omega t}$ in $\mathcal{H}$, where $|\alpha\rangle$ forms a complete orthogonal basis in $\mathcal{H}$ and m can take any integer value. With these ingredients, one can rewrite Eq. 2.49 in Floquet space as

$$\bar{Q}|u_{n,m}\rangle\rangle = \varepsilon_{nm}|u_{n,m}\rangle\rangle. \tag{2.54}$$

Now the time-dependent problem of Eq. 2.49 in $\mathcal{H}$ is reduced to the eigenvalue problem of $\bar{Q}$ in $\mathcal{F}$. This eigenvalue problem can be solved by diagonalizing the quasienergy operator.

Within the new basis $|\alpha m\rangle\rangle$, the matrix elements of the quasienergy operator are given by

$$\begin{aligned}\langle\langle \alpha' m'|\bar{Q}|\alpha m\rangle\rangle &= \frac{1}{T}\int_0^T \mathrm{d}t\, e^{-i(m'-m)\omega t}\,\langle\alpha'|\hat{H}(t) + m\hbar\omega|\alpha\rangle \\ &= \langle\alpha'|\hat{H}^{(m'-m)}|\alpha\rangle + \delta_{m'm}\delta_{\alpha'\alpha}m\hbar\omega. \end{aligned}\tag{2.55}$$

Here

$$\hat{H}^{(m)} = \frac{1}{T}\int_0^T e^{-im\omega t}\hat{H}(t)\mathrm{d}t \tag{2.56}$$

denotes the m^{th} Fourier component of the Fourier decomposition of $\hat{H}(t)$. The matrix representation of the quasienergy operator has a clear block structure

$$\langle\langle \alpha' m' | \bar{Q} | \alpha m \rangle\rangle = \left(\begin{array}{c|ccccc|c} . & . & . & . & . & . & . \\ \hline . & \hat{H}^{(0)} + 2\hbar\omega & \hat{H}^{(1)} & \hat{H}^{(2)} & \hat{H}^{(3)} & \hat{H}^{(4)} & . \\ . & \hat{H}^{(-1)} & \hat{H}^{(0)} + \hbar\omega & \hat{H}^{(1)} & \hat{H}^{(2)} & \hat{H}^{(3)} & . \\ . & \hat{H}^{(-2)} & \hat{H}^{(-1)} & \hat{H}^{(0)} & \hat{H}^{(1)} & \hat{H}^{(2)} & . \\ . & \hat{H}^{(-3)} & \hat{H}^{(-2)} & \hat{H}^{(-1)} & \hat{H}^{(0)} - \hbar\omega & \hat{H}^{(1)} & . \\ . & \hat{H}^{(-4)} & \hat{H}^{(-3)} & \hat{H}^{(-2)} & \hat{H}^{(-1)} & \hat{H}^{(0)} - 2\hbar\omega & . \\ \hline . & . & . & . & . & . & . \end{array}\right). \tag{2.57}$$

The diagonal blocks of this matrix are given by the time-average of the Hamiltonian $\hat{H}(t)$, shifted by integer multiples of $\hbar\omega$ from each other. The off-diagonal blocks can be regarded as coupling terms between different m-sectors. This Hamiltonian shows close similarities to the dressed-atom picture of a quantum system driven by coherent radiation [101]. Due to this similarity, the index m is often referred to as the photon number and the coupling matrix elements $\hat{H}^{(m)}$ are said to describe m-photon processes. To obtain the quasienergies and Floquet states of $\bar{Q}$ one can diagonalize the matrix defined in Eq. 2.57 numerically by truncating the matrix after a given m-sector. This procedure is similar to the determination of the energy bands and Bloch waves in an optical lattice, described in section 2.2.1. However, there is also a different option to determine the quasienergies and Floquet states of the system which we will discuss in the next sections.

2.3.3 The Floquet Hamiltonian and Floquet engineering

In section 2.3.1, we have seen that the eigenstates of a time-periodic Hamiltonian with period T are themselves time-periodic with the same periodicity. In general, the time evolution of a state $|\psi(t)\rangle = \hat{U}(t, t_0)\,|\psi(t_0)\rangle$ is described by the time-evolution operator $\hat{U}(t, t_0)$. Its general form is given by

$$\hat{U}(t, t_0) = \hat{\mathcal{T}} e^{-\frac{i}{\hbar}\int_{t_0}^{t} \mathrm{d}t' \hat{H}(t')}, \tag{2.58}$$

where $\hat{\mathcal{T}}$ denotes the time-ordering operator. In the special case where the Hamiltonian $\hat{H}(t)$ is periodic in time, one can construct an effective, time-independent Hamiltonian that yields the same time-evolution as $\hat{H}(t)$ over the course of one period. This time-independent Hamiltonian is given by [96]

$$\hat{H}_{\text{eff}} = \hat{U}^{\dagger}_{\text{eff}}(t)\hat{H}(t)\hat{U}_{\text{eff}}(t) - i\hbar\hat{U}^{\dagger}_{\text{eff}}(t)\dot{\hat{U}}_{\text{eff}}(t), \tag{2.59}$$

where $\hat{U}_{\text{eff}}(t) = \hat{U}_{\text{eff}}(t+T)$ is a time-periodic unitary operator with period T. One can now rewrite the time evolution operator in terms of this effective Hamiltonian and obtains [98]

$$\hat{U}(t,t_0) = \hat{U}_{\text{eff}}(t) e^{-\frac{i}{\hbar}(t-t_0)\hat{H}_{\text{eff}}} \hat{U}^{\dagger}_{\text{eff}}(t_0). \tag{2.60}$$

This equation illustrates that the time evolution of a Floquet system is composed of two components. On the one hand, we have the so-called micromotion operator $\hat{U}_{\text{eff}}(t)$, which describes the time evolution within one driving period and on the other hand, we have the time-independent effective Hamiltonian $\hat{H}_{\text{eff}}$, which describes the unitary time evolution of the state for the duration $(t - t_0)$.

The micromotion operator, as well as the corresponding effective Hamiltonian, are, however, not uniquely defined. One can, for example, construct a new micromotion operator $\hat{U}'_{\text{eff}}(t)$ by multiplying an arbitrary time-independent unitary operator from the right[6]. By choosing this time-independent operator to be $\hat{U}_{\text{eff}}(t_0)$, the new micromotion operator $\hat{U}'_{\text{eff}}(t) = \hat{U}_{\text{eff}}(t)\hat{U}^{\dagger}_{\text{eff}}(t_0)$ becomes the identity matrix whenever $t = t_0 + nT$, with n being an integer. Inserting this new micromotion operator into Eq. 2.59, the newly obtained effective Hamiltonian reads $\hat{H}_{\text{F}} = \hat{U}_{\text{eff}}(t_0)\hat{H}_{\text{eff}}\hat{U}^{\dagger}_{\text{eff}}(t_0)$ and is termed the Floquet Hamiltonian[7]. With this new micromotion operator the time evolution operator defined in Eq. 2.60 becomes

$$\hat{U}(t,t_0) = \hat{U}_{\text{eff}}(t)\hat{U}^{\dagger}_{\text{eff}}(t_0) e^{-\frac{i}{\hbar}(t-t_0)\hat{H}_F}. \tag{2.61}$$

For the special case, where one is only interested in the time evolution over complete periods T, such that $t = t_0 + nT$, Eq. 2.61 reduces to

$$\hat{U}(t_0+T,t_0) = e^{-\frac{i}{\hbar}\hat{H}_F T}. \tag{2.62}$$

This expression is the definition of the time evolution operator for a time-independent Hamiltonian, which shows the elegance of the concept of the Floquet Hamiltonian. It reproduces the time evolution generated by the time-dependent Hamiltonian $\hat{H}(t) = \hat{H}(t+T)$ over one period. Thus, by looking at the system in a stroboscopic fashion, the system seems to behave as if it is governed by the time-independent Floquet Hamiltonian.

One can also turn this argument around: by actively shaping the time periodicity of a Hamiltonian one can mimic a Floquet Hamiltonian of desired properties. This concept is called Floquet engineering. To be able to implement such engineered Hamiltonians, the system, wherein this engineering should take place, needs to fulfill certain criteria. Most importantly, it needs to allow the implementation of

[6] Note that the corresponding Floquet states do not change under such transformations since they are eigenstates of the uniquely defined time-evolution operator.

[7] As already mentioned before, the term Floquet Hamiltonian is sometimes used to describe the quasienergy operator $\hat{Q}$.

time-periodic driving schemes. In addition, the system should be well isolated from its environment to reduce dissipative processes while the system is being driven. Furthermore, it has to be possible to compute the corresponding Floquet Hamiltonian, at least within reasonable approximations, and its resulting description of the system should stay valid on experimentally relevant time scales. The above considerations make ultracold quantum gases an ideal candidate for Floquet engineering, as they are well isolated from their environment and provide a large toolbox of control parameters and manipulation schemes.

Within the field of ultracold quantum gases, Floquet engineering already enabled the creation of Hamiltonians that would not have been possible in static systems. Some prime examples of such engineered Hamiltonians in optical lattice systems are the suppression and inversion of tunneling matrix elements in optical lattices [10], the dynamic control of the superfluid to bosonic Mott insulator transition [48] or the implementation of kinetic frustration [102]. One of the most intriguing achievements of this newly emerging field was the creation of artificial gauge fields for neutral atoms, as well as the creation of topological band structures in optical lattice systems [53–55, 58–62, 68, 103–106].

These examples show that the field of Floquet engineering holds large prospects for the future. However, one also has to state that Floquet systems have intrinsic problems. Even though one can describe the shaken system by an effective static Hamiltonian, its properties are generally quite different to a "real" static Hamiltonian. One prime example is that the energy of a driven system is not uniquely defined anymore. As a result, energy is not conserved which can eventually lead to dramatic heating rates of the system. This topic will be discussed in detail in chapters 4 and 5 where we measure and determine the different kinds of heating processes that appear in driven optical lattice systems.

2.3.4 Determination of the band structure of a driven lattice system

In this section, we will describe how one can determine the Floquet Hamiltonian and the band structure of a shaken one-dimensional optical lattice. Throughout this thesis, whenever we speak of a shaken lattice, we mean a periodic back and forth acceleration of the lattice. In the previous section, we have seen that the time evolution of a physical state in a driven system can be described by a time-independent Floquet Hamiltonian if we look at the time evolution in a stroboscopic fashion. Looking at Eq. 2.62, we find that the Floquet Hamiltonian itself still depends on the initial time t_0 but as this dependence is based on a unitary transformation, the spectrum of the Hamiltonian is independent of t_0. Consequently, we can set $t_0 = 0$ and write the time evolution operator as

$$\hat{U}(T,0) \equiv \hat{U}(T) = \hat{\mathcal{T}} e^{-\frac{i}{\hbar}\int_0^T \mathrm{d}t' \hat{H}(t')} = e^{-\frac{i}{\hbar}\hat{H}_F T}. \tag{2.63}$$

In the case of a shaken one-dimensional optical lattice, one can directly evaluate the time evolution operator numerically[8] as it is defined in the center part of Eq. 2.63.[9] The single-particle Hamiltonian of the shaken system is, in the reference frame comoving with the shaken lattice, given by

$$\hat{H}(t) = \frac{\hat{p}^2}{2M} + V_0 \cos^2(k_L x) - F_0 \sin(\omega t). \tag{2.64}$$

Here the last term describes the external, time-periodic forcing of the lattice. As this Hamiltonian is periodic in space as well as in time, the corresponding eigenstates and eigenenergies will be both periodic in momentum as well as in energy, see Fig. 2.6 (a). Therefore, driven lattice systems are sometimes referred to as spatiotemporal crystals [107]. By using the identity $\sin(\omega t) = 1/(2i)(e^{i\omega t} - e^{-i\omega t})$ one can rewrite the Hamiltonian of Eq. 2.64 as

$$\hat{H}(t) = \sum_{m=-1}^{1} \hat{H}_m e^{im\omega t}, \tag{2.65}$$

where $\hat{H}_0$ corresponds to the static lattice Hamiltonian defined in Eq. 2.25 and $\hat{H}_{\pm 1} = \pm F_0/(2i)$. From section 2.2.1 we know already how to determine the band structure of the static lattice Hamiltonian numerically. This same technique can be used to determine the band structure of the driven Hamiltonian. To make the numerical evaluation of $\hat{H}(t)$ tractable, we first restrict ourselves to the lowest n bands of the static Hamiltonian and project the modulation Hamiltonians $\hat{H}_{\pm 1}$ onto the subspace of these n bands. By breaking the time evolution over one period into N discrete steps

$$0 = t_0 < t_1 < \ldots < t_{N-1} < t_N = T, \tag{2.66}$$

we can approximate the time evolution operator by

$$\hat{U}(T) \approx \prod_{i=0}^{N} e^{-\frac{i}{\hbar}\hat{H}(t_i)(t_{i+1}-t_i)}. \tag{2.67}$$

[8] This direct numerical evaluation of the time evolution operator is also feasible in the case of a shaken honeycomb lattice.

[9] In section 2.3.2 we have shown that one can, in principle, also determine the quasienergies of a driven system by numerically diagonalizing the quasienergy operator defined in Eq. 2.57. This picture of the quasienergy operator will become important later on when we determine the heating channels in the driven lattice system.

This approximation can get arbitrarily precise for a large number of time steps and is thus only limited by computational power. According to Eq. 2.63 we can determine the Floquet Hamiltonian by taking the logarithm of Eq. 2.67

$$\hat{H}_F = \frac{i\hbar}{T} \log\left(\hat{U}(T)\right). \tag{2.68}$$

By numerically diagonalizing this equation, the band structure of the driven one-dimensional lattice can be obtained. Since the complex logarithm is multivalued [108], one directly regains the property that the quasienergies are only defined modulo $\hbar\omega$. This peculiarity is illustrated in Fig. 2.6 (a). The left plot of Fig. 2.6 (a) shows the lowest three bands of a static lattice with a lattice depth of $11E_r$. The right plot shows the same band structure within the Floquet picture, with a driving frequency of $\omega = 0.5E_r/\hbar$ and a vanishing driving force F_0. As this band structure is periodic in energy, we can arbitrarily set its zero point. In order to make the lowest band of the static Hamiltonian appear as the lowest band in the Floquet picture, at least in the limit of a negligible driving force, we subtract the energy $E_0^{(0)}$, which corresponds to the energy of the lowest band in the static lattice at quasimomentum $q = 0$, from the right side of Eq. 2.68.

The advantage of determining the band structure with the presented method is that once the Hamiltonian $\hat{H}(t)$ of the system is given, there are no further approximations involved and one is only limited by computational power. Given a time-dependent Hamiltonian defined in an n-dimensional Hilbert space, the determination of its Floquet Hamiltonian with this technique requires the exponentiation and multiplication of $n \times n$ matrices. Each exponentiation has a computational complexity of $O(n^3)$ [109], whereas the multiplication of two matrices has a computational complexity of approximately $O(n^2)$ [110]. Depending on the size of the matrix this approach might not be feasible anymore. However, there are also other methods available with which one can approximately determine the Floquet Hamiltonian. If, for example, the energy scale $\hbar\omega$ of the driving is much larger than the typical energy scale of the system, one can approximate the Floquet Hamiltonian within a high-frequency approximation [63, 111–113]

$$\hat{H}_\mathrm{F} \approx \sum_{\mu=1}^{\mu_\mathrm{cut}} \hat{H}_\mathrm{F}^{(\mu)}. \tag{2.69}$$

The leading orders of this approximation are given by

$$\begin{aligned}
\hat{H}_{\mathrm{F}}^{(1)} &= \hat{H}^{(0)}, \\
\hat{H}_{\mathrm{F}}^{(2)} &= \sum_{m\neq 0} \frac{\hat{H}^{(m)}\hat{H}^{(-m)}}{m\hbar\omega}, \\
\hat{H}_{\mathrm{F}}^{(3)} &= \sum_{m\neq 0} \left(\frac{\left[\hat{H}^{(-m)}, \left[\hat{H}^{(0)}, \hat{H}^{(m)}\right]\right]}{2(m\hbar\omega)^2} + \sum_{m'\neq 0,m} \frac{\left[\hat{H}^{(-m')}, \left[\hat{H}^{(m'-m)}, \hat{H^{(m)}}\right]\right]}{3mm'(\hbar\omega)^2} \right),
\end{aligned} \tag{2.70}$$

with Fourier components $H^{(m)}$ as defined in Eq. 2.56. This method has the advantage that no matrix exponents have to be evaluated, which makes the theoretical evaluation much more practicable. Another type of high-frequency expansion with which one can approximate the Floquet Hamiltonian is the Floquet-Magnus expansion [114–116], which exhibits similar terms than the high-frequency approximation described above.

We have seen that the determination of the full effective Hamiltonian of a driven system can be very complex. Especially if the driven system is comprised of many interacting particles, it might even be impossible to write down an explicit expression for the effective Hamiltonian. In this sense, if one employs the external driving to mimic a desired Hamiltonian $\hat{H}_{\mathrm{des}}$, the main challenge is to find a driving scheme where the lowest order(s) of the high-frequency expansion of the real driving Hamiltonian correspond(s) to the desired Hamiltonian. The physical properties of the driven system can thus be regarded as an approximation to the properties of the desired system and not the other way round.

In the following two sections we will discuss two different shaking regimes in a one-dimensional lattice. At first, we will look at shaking frequencies much smaller than the band gap to the first excited band and then at shaking frequencies that are larger than the band gap. We will see that the resulting band structures exhibit fundamentally different features in these two shaking regimes.

2.3.5 Driving frequencies well below the band gap

Figure 2.6 (b) shows the resulting band structure of the driven one-dimensional lattice when the shaking frequency is much smaller than the band gap Δ_{10} between the lowest band and first excited band. To keep the figures clear, we restrict the band structure calculation to the lowest two bands. Note that this restriction will lead to wrong predictions of the band structure for large driving forces but it correctly

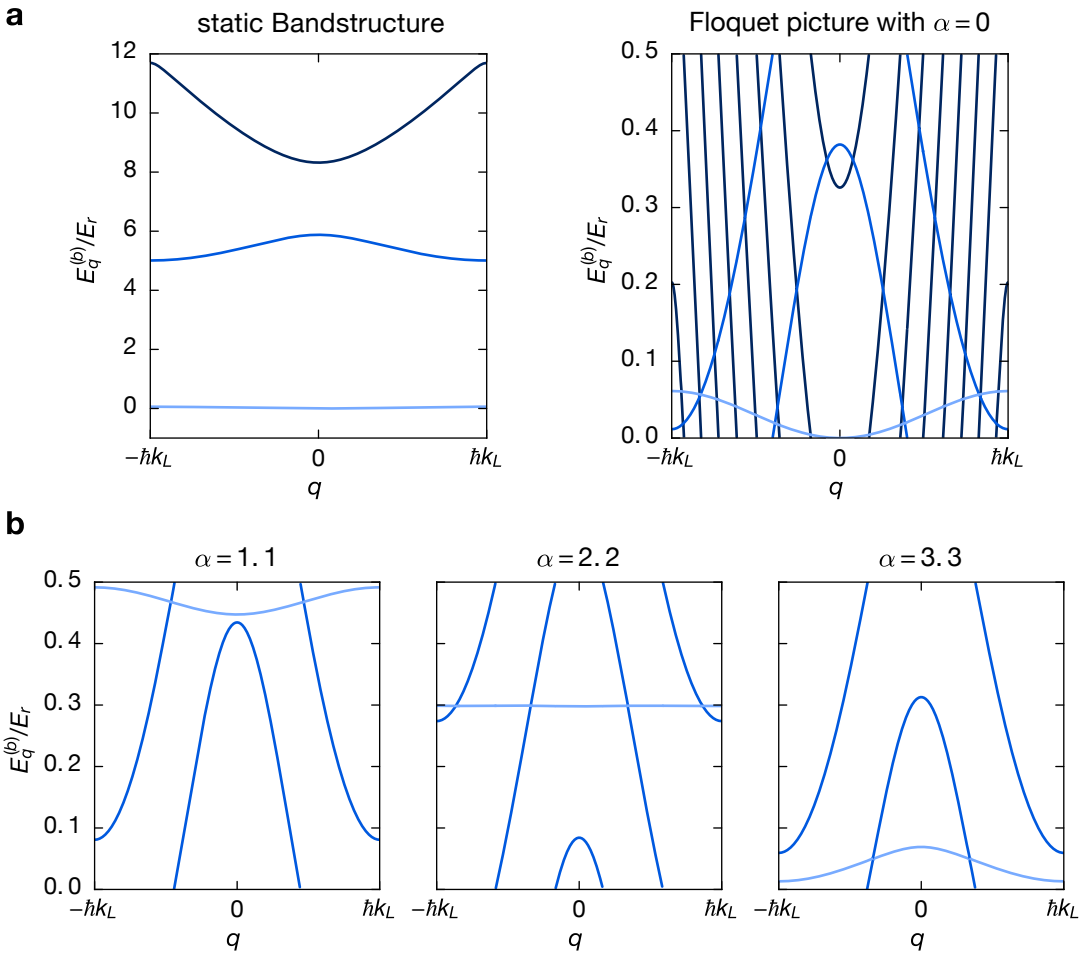

Figure 2.6: **Floquet band structure for driving frequencies well below the band gap.** **(a)** The left plot shows the band structure of a static, one-dimensional lattice with a lattice depth of $11E_r$. The right plot shows the band structure within the Floquet picture in the limit of zero driving strength when the lattice is shaken with a frequency $\omega = 0.5E_r/\hbar$. The band structure is now periodic both in momentum as well as in energy. **(b)** Bandstructure for three different driving strengths $\alpha \equiv dF_0/(\hbar\omega)$. For reasons of visibility we only take the lowest two bands of the static lattice into account, when performing the Floquet band structure calculation. This will, however, lead to wrong results if the driving strength α becomes large. However, within the range plotted here, the behavior of the lowest band is reproduced correctly. From left to right one can see that the bandwidth of the lowest band first decreases and for $\alpha > 2.4$ the band structure even flips over. This behavior can be described by a Bessel function renormalization of the tunneling matrix element of the lowest band.

shows the structure of how the driving will alter the band structure[10].

Let us at this point comment on the future notation of energy bands. We will refer to the band which is adiabatically connected[11] to the lowest band in the static lattice, as the lowest band in the Floquet picture. However, keep in mind that the quasienergy in a Floquet system is cyclic and technically speaking, the concept of a lowest lying energy band does not make sense anymore. However, to avoid lengthy descriptions, we will use the established notations for static energy bands also in the Floquet picture. In this sense, the first excited band in the Floquet picture is the band that is adiabatically connected to the first excited band in the static lattice.

Starting from the left plot of Fig. 2.6 (b), one can see that the lowest band gets more and more modified the stronger the driving becomes. At first, the bandwidth of the lowest band decreases before it becomes completely flat and then bends over such that the lowest band exhibits a maximum at $q = 0$. To understand this behavior in an intuitive way, let us consider the following single-particle model. If the band gap to the first excited band is very large, corresponding to a deep tight-binding regime, one can assume that the dynamics of the system is restricted to the lowest band, even in the presence of the external driving. Within this approximation, one finds that the solutions of the corresponding Schrödinger equation are given by the so-called Houston states. These states exhibit a time-dependent quasimomentum $q(t)$ that is described by [11, 118]

$$q(t) = -\frac{F_0}{\hbar\omega}\cos(\omega t), \tag{2.71}$$

where we have assumed that the initial quasimomentum at $t = 0$ was $q = 0$. As expected intuitively, the periodic external force leads to a periodically changing quasimomentum. Since we assumed the lattice to be deep, the tight-binding approximation applies and we can express the dispersion relation of the lowest band by

$$E^{(0)}(q) = -2J_0\cos(dq). \tag{2.72}$$

Inserting the time-dependent quasimomentum of Eq. 2.71 into the above equation leads to a time-dependent dispersion relation. In the limit where the shaking frequency ω is much larger than the typical energy scale of the lowest band ($\hbar\omega \gg J_0$), the effective band structure can be obtained by time-averaging the tight-binding band structure over one driving cycle

[10] Fig. 2.7 shows the band structure calculation for the lowest five bands, for the same driving parameters.

[11] This means that the lowest band in the Floquet picture is the one which is connected to the lowest band in the static lattice when the shaking amplitude of the drive is ramped up slowly. Note that due to the quasienergy spectrum such an adiabatic connection is not always possible [117]. Especially for very large driving strengths, one can observe a strong mixing of bands which makes an unambiguous assignment of the individual bands impossible.

$$E_{\text{eff}}(q) = \frac{1}{T}\int_0^T \mathrm{d}t\, E^{(0)}(q(t)) = -2J_{\text{eff}}\cos(dq). \tag{2.73}$$

Here, we have introduced the effective tunneling matrix element J_{eff}, which is given by the bare tunneling matrix element J_0 rescaled by the zeroth-order Bessel function of the first kind $\mathcal{J}_0$

$$J_{\text{eff}} = J_0\mathcal{J}_0\left(\frac{dF_0}{\hbar\omega}\right) = J_0\mathcal{J}_0(\alpha). \tag{2.74}$$

From this equation one can see that the amount of rescaling of the lowest band is governed by the dimensionless forcing strength $\alpha \equiv dF_0/(\hbar\omega)$, which we will use throughout the rest of this thesis to characterize the strength of the driving. Figure 2.7 (c) shows the dependence of the zeroth-order Bessel function on the driving strength α. With this gained knowledge we can interpret the results we obtained in Fig. 2.6 (b). For increasing driving strengths α, the tunneling matrix element of the lowest band decreases, resulting in a smaller bandwidth. At $\alpha \approx 2.4$ the Bessel function becomes zero leading to a flat band as can be observed in the center plot of Fig. 2.6 (b). By increasing α even further, the Bessel function becomes negative, leading to a negative tunneling matrix element and thus to an inversion of the lowest band.

At these large values of α one cannot neglect the impact of higher lying bands anymore and has to take them into account. Figure 2.7 (a) shows the resulting Floquet band structure for $\alpha = 3.8$ at the same driving frequency as in Fig. 2.6, when taking into account the lowest five bands of the static band structure. Due to the interplay of the involved bands, the resulting band structure looks much more complicated than before. The inversion of the lowest band is again nicely visible but, in addition, also the first excited band has flipped around and exhibits an opposite curvature compared to the static lattice case. This behavior was not visible in Fig. 2.6 because higher lying bands were not taken into account. At this driving strength of $\alpha = 3.8$, the first excited band is already quite distorted due to strong couplings to other higher lying excited bands. As the band gap to these higher lying bands is much smaller than for the lowest band, their coupling to the first excited band is much stronger. However, if one zooms into the lowest band as shown in Fig. 2.7 (b), one can also see avoided crossings appearing in the lowest band. At these avoided crossings, multiphoton-like couplings between the involved bands lead to strong excitations of atoms into the higher lying band [107]. This typically leads to strong atom number losses and heating, which eventually reduces the lifetime of the condensate [119]. We will address this topic of multiphoton excitations in more detail in chapter 4.

There have already been several experiments that observed the expected Bessel function rescaling of the tunneling matrix element. The dynamic suppression of

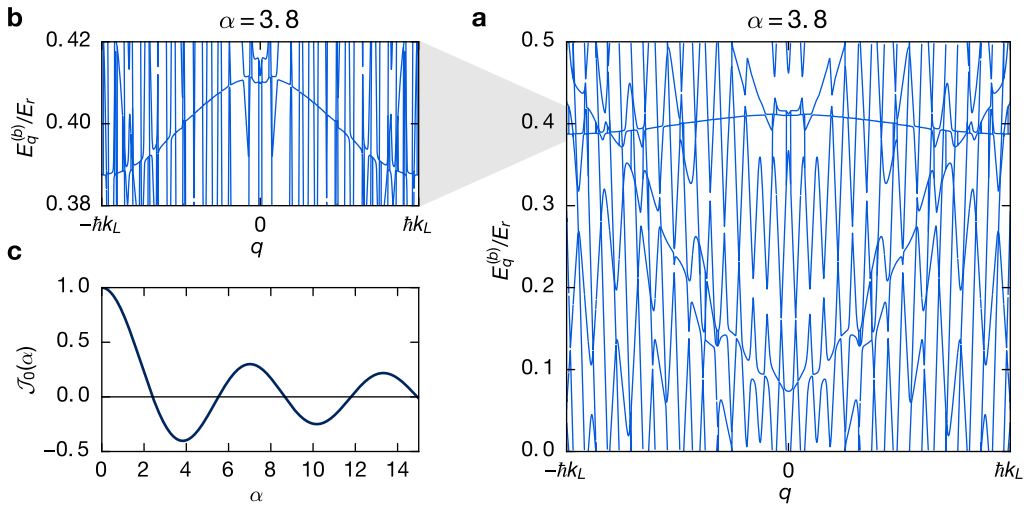

Figure 2.7: **Floquet band structure and Bessel function.** **(a)** Floquet band structure for a driving frequency of $\omega = 0.5\,E_r/\hbar$, as in Fig. 2.6, and $\alpha = 3.8$ but this time taking into account the lowest five bands of the static lattice. One can see the inversion of the lowest band as already expected from the tight-binding approximation. Furthermore, one can observe an inversion of the first excited band, which, however, is already strongly distorted due to strong couplings with higher lying excited bands. **(b)** Zoom into the lowest band. One can see multiple avoided crossings distorting the lowest band. At these avoided crossings strong excitations to higher lying bands can be expected. **(c)** Dependence of the zeroth order Bessel function on the driving strength α. Within a high frequency tight-binding approximation the tunneling matrix element of the lowest band can be expressed as $J_{\text{eff}} = J_0\mathcal{J}_0(\alpha)$.

tunneling when the Bessel function becomes zero was observed in references [9, 10, 44]. It was shown that this rescaling of the tunneling matrix element even holds true in the strongly correlated regime, where interactions between particles cannot be neglected anymore [47]. This property enabled the observation of the superfluid to Mott insulator transition in a shaken optical lattice [48]. Furthermore, the already mentioned experiments that create artificial gauge fields or topological band structures work in this driving regime [53–55, 58–62, 68, 103–106]. This type of Bessel function rescaling of shaken quantum systems is not limited to shaken lattices but appears for example, also in atoms subject to an off-resonant external rf-field where the Landé g-factor is altered by the same Bessel function type modification [120].

2.3.6 Driving frequencies above the band gap

In this section, we will take a closer look at the resulting Floquet band structure when the shaking frequency is larger than the band gap that separates the lowest band from the first excited band. Figure 2.8 shows the band structure for three different driving strengths α at a shaking frequency of $\omega = 7.5E_r/\hbar$ (compare to Fig. 2.6 (a)). One can observe clear differences to the band structure we obtained for the low-frequency case discussed before. Even for $\alpha > 2.4$ no inversion of the lowest band is observed anymore, which means that the Bessel function rescaling of the tunneling matrix element is not a valid description anymore. One can understand this new behavior also in an intuitive way. Remember that it was important for the previous discussion that the dynamics of the atoms is restricted to the lowest band. However, in the shaking regime we discuss now, the atoms are accelerated so fast back and forth that one can no longer assume that the atoms stay adiabatically in the lowest band.

Instead of the Bessel function rescaling one rather observes the appearance of a quartic point in the lowest band, followed by a double-well-like structure when α is increased even further. This appearing double-well-like structure is due to a hybridization between the rather narrow lowest band and the first excited band. The minima of this structure shift further towards the Brillouin zone edge the larger the driving strength becomes. At $\alpha \gtrsim 1.4$ the minima of the double-well structure merge with an avoided crossing to an excited band. Increasing the driving strength beyond this point does not shift the minima further out, but only enhances the coupling to higher lying excited bands which leads to a heavily distorted lower band. As already mentioned before, these avoided crossings between bands lead to strong excitations into higher lying bands and should, therefore, be avoided. As the minima of the lowest band merge with such an avoided crossings, the driving strength at this shaking frequency should be restricted to values smaller than approximately 1.4. One should also note that apart from strong distortions at large values of α, the shape of the dispersion relation of the excited bands is mostly unaffected by the

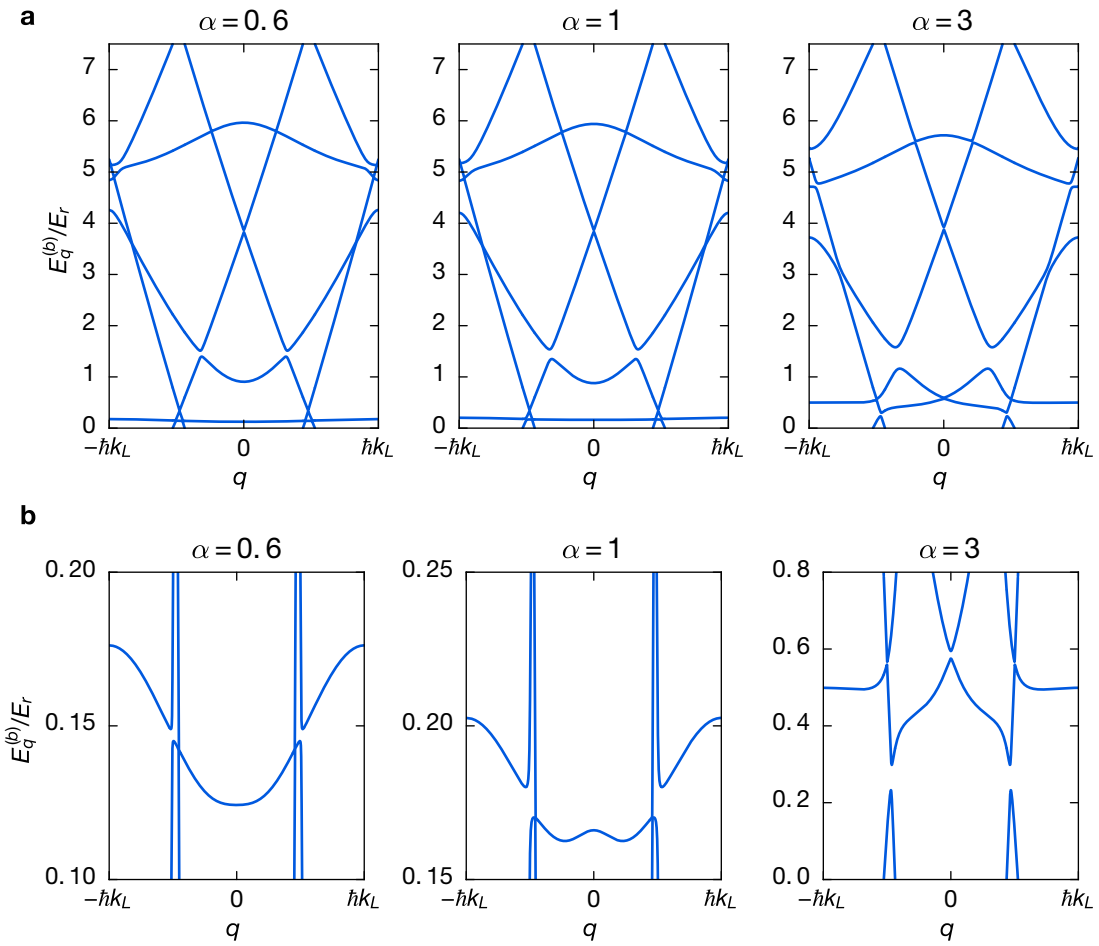

Figure 2.8: **Floquet band structure for large driving frequencies. (a)** Floquet band structure for a driving frequency of $\omega = 7.5\,E_r/\hbar$ when taking into account the lowest five bands of the static lattice. The shaking frequency lies in the band gap between the first and second excited band of the static lattice. From left to right the driving strength is increased. **(b)** Zoom into the lowest band. One can see the appearance of a double-well structure in the lowest band for driving strengths larger than approximately 0.6. For large values of α the minima positions of the lowest band merge with an avoided crossing which appears due to strong couplings to higher lying excited bands. Note the different energy scales in the plots.

shaking.

This appearing double-well structure in the lowest band has been observed experimentally [44] and was utilized to study the formation of symmetry-broken domains [45, 46].

Chapter 3

Experimental setup

In this chapter, we present an overview of the experimental setup and also introduce important manipulation techniques with which we can alter certain properties of the condensate. We start in section 3.1 by describing how far detuned light can be used to create conservative potentials in which cold atoms can be trapped. Afterwards, we will discuss properties of the crossed-beam dipole trap and describe how the two different lattice structures used in the context of this thesis, a one-dimensional lattice of "pancakes" and a honeycomb lattice, can be created by interfering multiple laser beams.

In section 3.2, the different cooling stages needed in order to create a BEC are described. Furthermore, we will show how the interaction strength between atoms can be tuned via Feshbach resonances.

Different detection techniques are discussed in section 3.3. At first, we will focus on absorption imaging from which all information about the BEC is obtained. Afterwards, we will discuss differences in the imaging technique that have to be considered when imaging the atoms at large magnetic offset fields. To infer information about the occupied momentum state of the atoms inside the lattice, two different detection techniques are available. By suddenly switching off the lattice potential we can infer the magnitude of the plane wave coefficients of the occupied Bloch wave of the atoms. This technique can be used to balance the intensities of the individual lattice beams. When slowly ramping down the lattice beams the momentum distribution, as well as the Bloch band occupied by the atoms, can be determined. Concluding this section, we will describe how periodic forcing of the lattice is implemented by frequency shifting one or multiple lattice beams.

In the last section of this chapter (3.4), we will characterize relevant properties of our system. We will start by determining the harmonic trapping frequencies followed by an atom number calibration. Both parameters will be important later on when we want to compare the measured heating rates in a driven optical lattice to the theoretical prediction. We will then discuss two techniques to determine the lattice depth and point out their differences. Lastly, we will show how one can infer the momentum spread of the condensate in the lattice by performing Bloch oscillations.

3.1 Optical potentials

Neutral atoms can be captured and trapped in intense light fields. The underlying effect, the so-called AC-Stark effect, creates a dipole potential through the interaction of the oscillating electric field of the laser light with the induced dipole moment of the atom. In the first part of this section, we will give a short overview of the theoretical background of optical dipole potentials. Afterwards, we will discuss the implementation of a crossed-beam dipole trap and optical lattices. In particular, we will focus on a one-dimensional optical lattice and a hexagonal lattice.

3.1.1 Optical dipole potentials

The interaction between the oscillating electric field of a laser beam and the induced dipole moment of the atom results in a dipole potential that is, for Alkali atoms, given by [121]

$$V_{\mathrm{dip}}(\boldsymbol{r}) = \frac{\pi c^2}{2}\left(\frac{\Gamma_{D2}}{\omega_{D2}^3}\frac{2+\mathcal{P}g_F m_F}{\Delta_{D2}} + \frac{\Gamma_{D1}}{\omega_{D1}^3}\frac{1-\mathcal{P}g_F m_F}{\Delta_{D1}}\right) I(\boldsymbol{r}). \tag{3.1}$$

Here $\Gamma_{D1(D2)}$ are the natural line widths of either the D1 or D2 transition, $\omega_{D1(D2)}$ the resonance frequency of the D1 (D2) transition, c the speed of light, $I(r)$ the intensity of the laser beam, g_F the Landé factor, m_F the magnetic quantum number and $\mathcal{P}$ characterizes the polarization of the laser beam. Linearly polarized light is described by $\mathcal{P} = 0$ and $\sigma^{\pm}$ polarized light is given by $\mathcal{P} = \pm 1$. Note that Eq. 3.1 is only valid for large detunings $\Delta_{D1(D2)}$, when the excited state hyperfine structure is not resolved. In this case, the detunings $\Delta_{D1(D2)}$ are given by

$$\frac{1}{\Delta_{D1(D2)}} = \frac{1}{\omega_L - \omega_{D1(D2)}} + \frac{1}{\omega_L + \omega_{D1(D2)}} \tag{3.2}$$

where ω_L is the laser frequency. Note that for large detunings the second term of the above equation can usually be neglected within a rotating-wave approximation [122]. If the laser frequency is larger (blue detuned) than the resonance frequency of the atoms, the dipole potential $V_{\mathrm{dip}}(\boldsymbol{r})$ becomes positive and hence, due to the repelling character of the potential, atoms want to sit at the intensity minima of the laser beam. For red-detuned light, when the laser frequency is smaller than the atomic resonance frequency, $V_{\mathrm{dip}}(\boldsymbol{r})$ becomes negative leading to an attractive potential. When using red-detuned laser light, it is important to increase the detuning as far as possible to reduce photon scattering events that heat up the atom cloud and would eventually lead to significant loss rates of atoms. Since the dipole potential scales like $V_{\mathrm{dip}}(\boldsymbol{r}) \propto 1/\Delta$ and the photon scattering rate scales like $\Gamma_{\mathrm{sc}} \propto 1/\Delta^2$ [121] it is favorable to use intense but far-detuned laser beams to create optical potentials.

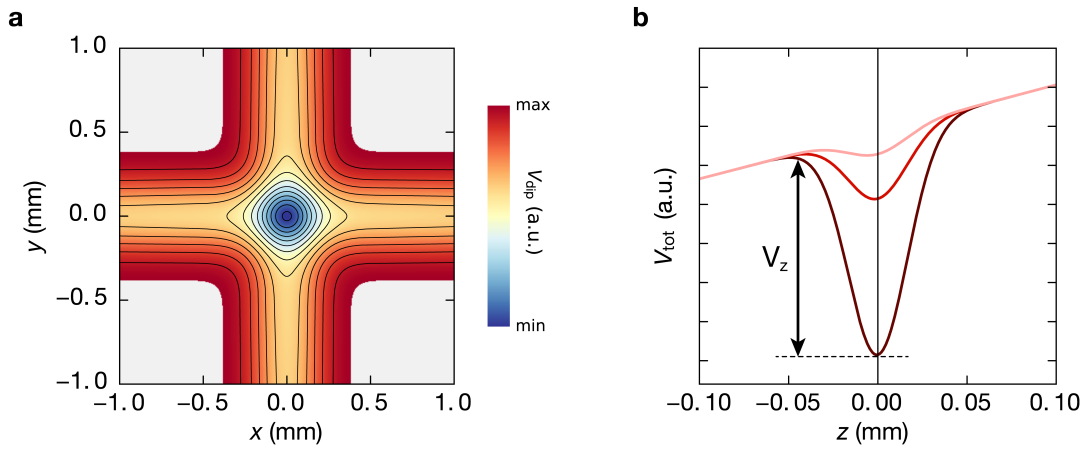

Figure 3.1: **Dipole trap potential. (a)** 2D-plot of the dipole potential resulting from the overlap of two Gaussian beams. In the center of the trap, the potential can be approximated by a harmonic oscillator potential. Some areas of the dipole potential that lie above a certain threshold value have been masked for better visibility. **(b)** Trapping potential along the vertical z-direction for three different intensities of the dipole beams (darker colors represent higher intensity). One can see that the minimum position of the potential shifts to lower z-values for weaker intensities. This gravitational sag is dependent on the mass of the trapped atoms, enabling the selective evaporation of the heavier ^{87}Rb atoms as discussed later in section 3.2.3. For the dark red curve, the minimum trapping depth along the vertical direction (V_z) is indicated by the black arrow.

3.1.2 Crossed-beam dipole trap

The optical dipole trap is formed by overlapping two Gaussian laser beams. The beams propagate in the x-y-plane and intersect each other at an 90° angle in their foci, see Fig. 3.1 (a). One can describe the intensity profile of a Gaussian beam propagating along the x-direction by

$$I(x) = \frac{2P}{\pi w_y(x) w_z(x)} e^{-2\left(\frac{y^2}{w_y^2(x)} - \frac{z^2}{w_z^2(x)}\right)}, \tag{3.3}$$

where P is the power of the laser beam and $w_y(x)$ and $w_z(x)$ are the widths along the y and z-direction. Their dependence on the x position is given by

$$w_{y,z}(x) = w_{0;y,z}\sqrt{1 + \left(\frac{x}{x_{R;y,z}}\right)}, \tag{3.4}$$

where $w_{0;y,z}$ is the waist of the beam and

$$x_{R;y,z} = \frac{\pi w_{0;y,z}^2}{\lambda} \tag{3.5}$$

is the Rayleigh range, a measure of how fast the beam diverges after its focus. To avoid any interference of the crossing beams their polarizations are set orthogonal to each other with an additional detuning of several tens of MHz between the beams. The total intensity profile is hence given by the sum of the individual intensities of the beams. The beam profiles of the two beams propagating in the x-y-plane are strongly elliptic with waists of approximately $w_{0;x,y} \approx 300\,\mu$m and $w_{0;z} \approx 35\,\mu$m. In the center of the trap, the resulting Gaussian potential can be approximated by a harmonic oscillator potential, see Eq. 2.21. The relation between the beam parameters and the corresponding harmonic trapping frequencies can be obtained by Taylor expanding the Gaussian potential around the center of the trap which yields

$$\omega_r = \sqrt{\frac{4V_{\mathrm{dip}}(0)}{Mw_r^2}} \quad \text{and} \quad \omega_z = \sqrt{\frac{8V_{\mathrm{dip}}(0)}{Mw_{0;z}^2}}, \tag{3.6}$$

where $w_{0;x} = w_{0;y} = w_r$. Figure 3.1 (a) shows the resulting trapping potential and Fig. 3.1 (b) a crosscut of the potential along the vertical direction. Along this direction, not only the dipole potential acts on the atoms but also earth's gravitational field, leading to

$$V_{\mathrm{tot}}(z) = V_{\mathrm{dip}}(z) + Mgz. \tag{3.7}$$

The gravitational potential leads to a shift of the minimum of $V_{\mathrm{tot}}(z)$, the so-called gravitational sag and additionally reduces the effective depth of the potential along the vertical direction, see Fig. 3.1 (b). This reduction of the trap depth is dependent on the mass of the atoms and will be exploited later on to selectively remove ^{87}Rb atoms from the dipole trap during evaporation.

3.1.3 Creating the 1D optical lattice

The one-dimensional lattice is created by interfering two free-running, coplanar laser beams with an out-of-plane polarization that intersect each other at an angle of $\theta = 120°$, see Fig. 3.2. Like the dipole trap beams, the lattice beams are strongly elliptic with waists in the horizontal direction of approximately $400\,\mu$m and $100\,\mu$m in the vertical direction. Since the extent of the lattice beams is much larger than the size of the BEC one can approximate them as two interfering plane waves with electric fields $E_1 \propto \exp(i(\omega t + k_L x))$ and $E_2 \propto \exp(i((\omega + \Delta\omega)t - k_L x))$. Here $k_L = 2\pi \sin(\theta/2)/\lambda$ is the projection of the wave vector of the laser beam with

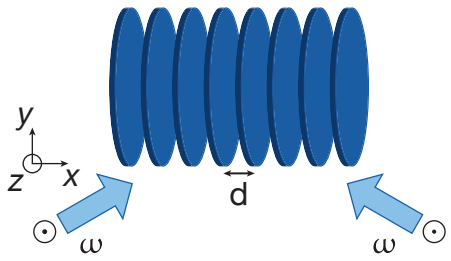

Figure 3.2: **Sketch of the one-dimensional optical lattice.** Two blue-detuned laser beams with out-of-plane polarization intersect each other at a 120° angle to form a one-dimensional lattice of "pancakes". Due to the blue-detuned laser beams, atoms are trapped in the nodes of the interference pattern.

wavelength λ onto the x-axis[1]. The resulting lattice potential, according to Eq. 3.1, can thus be expressed as

$$V_L(x) = V_0 \cos^2\left(k_L x - \frac{\Delta\omega}{2}t\right). \tag{3.8}$$

If the two laser beams have equal frequencies, corresponding to $\Delta\omega = 0$, one obtains a static one-dimensional optical lattice potential. Due to the finite extent of the lattice beams the created interference pattern has a "pancake" like shape as illustrated in Fig. 3.2. Later on in section 3.3.5 we will describe how an active control of $\Delta\omega$ creates an inertial force on the atoms trapped in the lattice. In our setup we use laser light at $\lambda = 736.8\,\mathrm{nm}$ which is blue-detuned compared to the D1 and D2 transitions of ^{39}K which results in the atoms sitting at the intensity minima of the interference pattern. Because of the Gaussian beam profile of the lattice beams, one obtains a spatially-dependent trapping potential which leads to a weak anti-confining potential that counteracts the confining part of the dipole trap [123, 124], see section 3.4.1. We have to take this anti-confining effect into account as the overall harmonic trapping frequencies enter the calculation of interaction dependent heating rates in chapters 4 and 5. Other experiments have exploited this tuning method to cancel out the overall horizontal confining potential leading to a homogeneous lattice system [125, 126]. Note that this tuning method is not available for red-detuned lattices where the attractive nature of the potential leads an additional confinement.

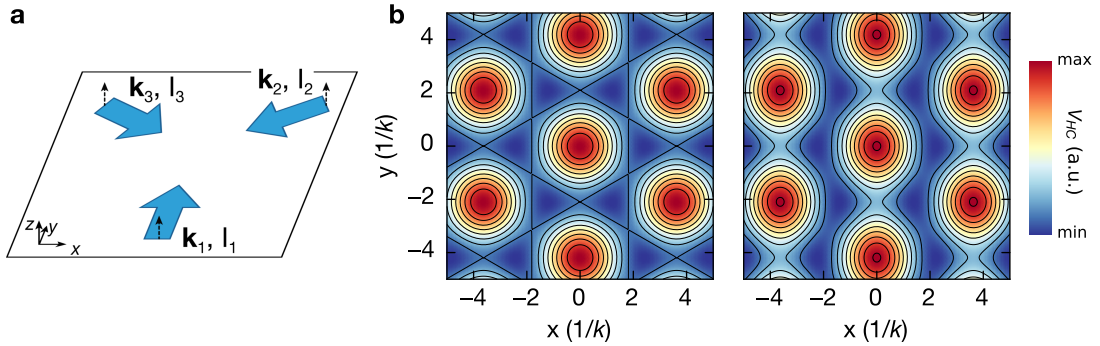

Figure 3.3: **Honeycomb potential. (a)** Sketch of the three lattice beams that interfere with each other under a 120° angle to create the honeycomb lattice. The beams propagate in the x-y-plane with out of plane polarization indicated by the dashed black arrows. Each of the individual beams is labeled with its wave vector $\boldsymbol{k}_i$ and intensity I_i. **(b) Left:** Potential landscape when all three beams have equal intensities. One can clearly observe the hexagonal structure of the potential minima. **Right:** Potential landscape for $I_1 = 0.7I_{2,3}$.

3.1.4 The honeycomb optical lattice

To create an optical honeycomb lattice we interfere three free-running, co-planar laser beams at an angle of 120°, see Fig. 3.3 (a). The polarization of each beam is aligned such that it points out of the x-y-plane resulting in the potential landscape shown in Fig. 3.3 (b). The intensity minima are aligned in a hexagonal pattern whereas the intensity maxima describe a triangular lattice structure. As for the one-dimensional lattice, the wavelength is chosen to be $\lambda = 736.8\,\text{nm}$ which is blue detuned to the resonance frequency of ^{39}K. In order to calculate the resulting interference pattern, one can approximate each lattice beam again by a plane wave, resulting in[2]

$$I_{HC}(\boldsymbol{r}) \propto \left| \sum_{n=1}^{3} \sqrt{I_n} e^{-i\boldsymbol{k}_n \boldsymbol{r}} \right|^2 . \tag{3.9}$$

[1]Since $\Delta\omega \ll \omega$ the change in frequency of the lattice beam has no effect on the magnitude of the wave vector.

[2]Note that we assume a simplified model where all beams are purely s-polarized as indicated in Fig. 3.3 (a). In general the polarization of the beams can be tilted leading to the generalized interference pattern $I(\boldsymbol{r}) = I^s(\boldsymbol{r}) + I^p(\boldsymbol{r})$. Here $I^s(\boldsymbol{r})$ is the interference pattern as shown in Eq. 3.9 and $I^p(\boldsymbol{r})$ has the same structure as Eq. 3.9 but the plane wave part is shifted by a phase. By tilting the polarization of the beams, an offset between the A and B lattice sites of the honeycomb lattice can be created. For more information about the polarization dependent part of the potential refer to [89, 90].

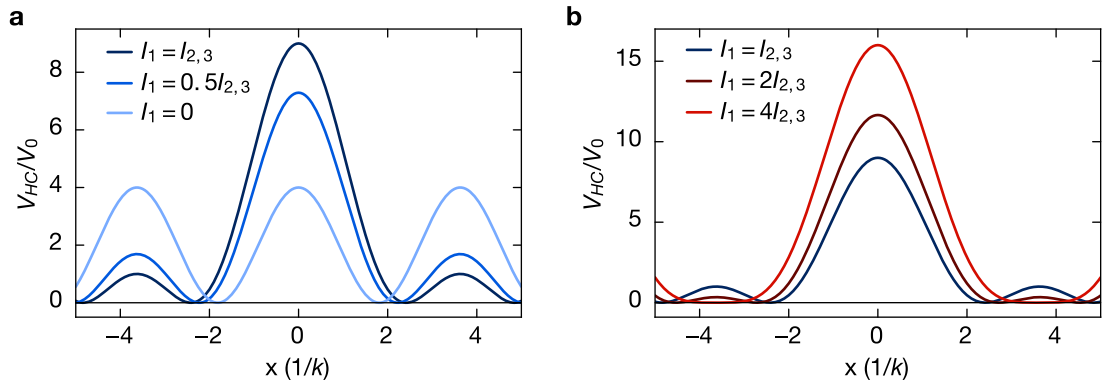

Figure 3.4: **Cross-cut of the honeycomb potential.** **(a)** Cross-cuts of the honeycomb potential at $y = 0$ for three different intensities $I_1 \leq I_{2,3}$. The potential barrier between two minima in the balanced honeycomb lattice corresponds to the potential V_0 created by a single beam. For increasing imbalance the positions of the potential minima shift and the potential barrier increases. For a vanishing intensity I_1 one recovers the one-dimensional lattice. **(b)** Cross-cuts for intensities I_1 larger than $I_{2,3}$. Here the minima move closer to each other until they merge at an imbalance factor of four. In this extreme limit, the lattice structure resembles that of a rhomboid.

Here $\boldsymbol{r} \equiv (x, y)$ is defined to lie within the x-y-plane and $\boldsymbol{k}_n$ are the wave vectors of the lattice beams which were already mentioned in section 2.2.4

$$\begin{aligned} \boldsymbol{k}_1 &= k\,(0,1) \\ \boldsymbol{k}_2 &= k\left(-\frac{\sqrt{3}}{2}, -\frac{1}{2}\right) \\ \boldsymbol{k}_3 &= k\left(\frac{\sqrt{3}}{2}, -\frac{1}{2}\right), \end{aligned}$$

with $k = 2\pi/\lambda$. By inserting the intensity pattern of Eq. 3.9 into Eq. 3.1 one obtains the lattice potential of the honeycomb lattice already mentioned in Eq. 2.37. For equal beam intensities this equation simplifies to

$$V_{HC}(\boldsymbol{r}) = 3V_0 + 2V_0 \cos((\boldsymbol{b}_1 - \boldsymbol{b}_2)\boldsymbol{r}) + 2V_0 \cos(\boldsymbol{b}_2\boldsymbol{r}) + 2V_0 \cos(\boldsymbol{b}_1\boldsymbol{r}), \tag{3.10}$$

where $\boldsymbol{b}_1 = \boldsymbol{k}_1 - \boldsymbol{k}_2$ and $\boldsymbol{b}_2 = \boldsymbol{k}_3 - \boldsymbol{k}_1$ are the primitive reciprocal lattice vectors.

The left plot of Fig. 3.3 (b) shows the real space lattice structure for equal beam intensities. If the intensity I_1 of beam one is lowered (right plot of Fig. 3.3 (b)),

the potential wells between the individual lattice minima are not equal anymore, leading to non-isotropic tunneling and the loss of the rotational symmetry of the lattice. Figure 3.4 (a) shows a cross cut of the potential along the x-direction for different beam imbalances. If $I_1 < I_{2,3}$, the lattice minima move further apart from each other. In the extreme case of $I_1 = 0$, one recovers the one-dimensional lattice discussed in the previous section. On the other hand, if $I_1 > I_{2,3}$, the potential minima move closer to each other until they merge, see Fig. 3.4 (b), leading to a rhombic lattice structure.

3.2 Creation of a BEC

In this section, we will give a brief overview of the different cooling steps necessary to create a BEC in our apparatus. Since the vacuum setup and all cooling stages have already been described in great detail, in whole or in part in the following references [89, 90, 124, 127, 128], we will only focus on the most relevant topics in order to present a comprehensible overview of the setup.

3.2.1 Magneto-optical trap

The initial cooling stage for ^{39}K and ^{87}Rb is a shared dual-species $2D^+$ magneto-optical trap (MOT) [129–131]. After this precooling stage, the atoms enter a 3D-MOT [132] through a differential pumping section. We load the ^{87}Rb MOT for 8 s almost to saturation while the ^{39}K MOT is only turned on during the last 0.6 s of the MOT phase. Figure 3.5 shows the hyperfine level structure of ^{39}K and ^{87}Rb together with the relevant transitions used in the experiment. Note that the hyperfine splitting of the excited state manifold of ^{39}K is much smaller than for ^{87}Rb. In fact, the typical detunings of the cooling transition of ^{39}K exceed the hyperfine splitting of the entire excited state manifold[3], which therefore remains unresolved. Hence, the cooling transition for ^{39}K cannot be regarded as closed and the distinction between a cooling and a repump transition for ^{39}K is somewhat arbitrary since both of them are red detuned compared to the excited state manifold.

At the end of the MOT phase, we compress the MOT [133] by increasing the quadrupole gradient and changing the detunings of the lasers in order to increase the density of the two atom clouds. Afterwards, the quadrupole field is switched off and the atoms undergo polarization gradient cooling [132] to reach sub-Doppler temperatures. Due to the small hyperfine splitting in the excited states of ^{39}K, sub-Doppler cooling is not very efficient [134]. To increase the efficiency of the ^{39}K molasses the repump and cooling intensities are reduced during the molasses phase compared to the MOT phase [135, 136]. Another concept to increase the efficiency

[3] The optimal value for the detuning of the cooling transition $F = 2 \rightarrow F' = 3$ for ^{39}K is approximately 40 MHz in our setup.

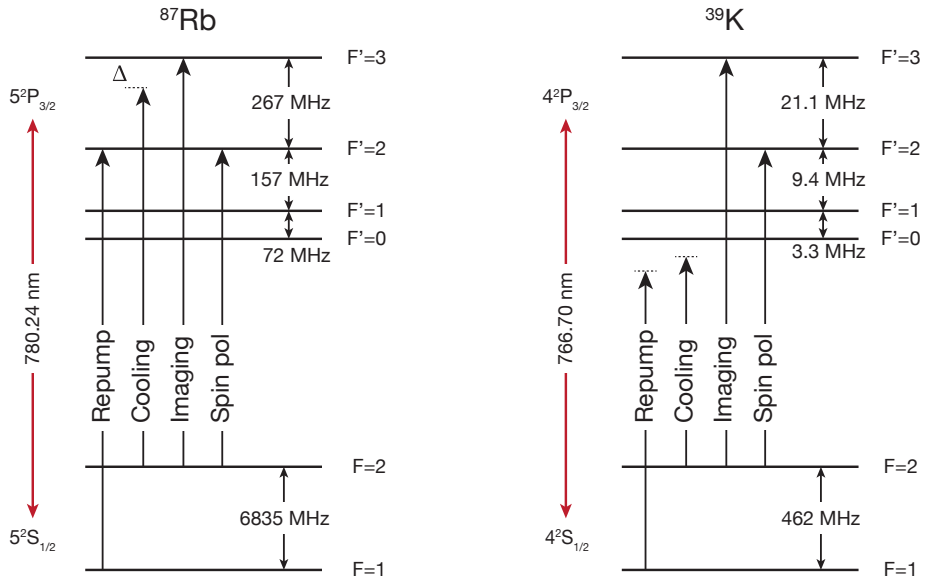

Figure 3.5: **Hyperfine level structure of the D2 lines of ^{87}Rb and ^{39}K.** The arrows depict the utilized transitions for ^{39}K and ^{87}Rb. Due to the small hyperfine splitting of the excited state manifold of ^{39}K, both the repump and cooling transitions are red detuned. The data was taken from [138] and [139].

of the molasses would be the implementation of a gray molasses scheme [137]. After the molasses we spin-polarize the atoms into their $|F = 2, m_F = 2\rangle$ hyperfine state to be able to trap them efficiently in a quadrupole trap and transport them into the science cell.

3.2.2 Magnetic transport and microwave evaporation

Neutral atoms in a magnetic-sensitive m_F state experience a Zeeman energy shift in the presence of an external magnetic field. For weak magnetic fields $B(\boldsymbol{r})$, this potential energy is given by

$$E_Z(\boldsymbol{r}) = \mu_B g_F m_F \left|B(\boldsymbol{r})\right|, \tag{3.11}$$

where μ_B is Bohr's magneton. This energy shift can be exploited to trap atoms in a magnetic quadrupole field which is created by two coils in the anti-Helmholtz configuration [140]. To be able to trap the atoms in the center of the quadrupole field, they need to be in a weak field seeking state which increases its energy with increasing magnetic field strength. To this end, we trap both ^{87}Rb and ^{39}K in their $|F = 2, m_F = 2\rangle$ state since this state experiences the largest Zeeman energy shift and thus a tighter confinement of the atoms can be achieved at a fixed magnetic field strength. This property can additionally be exploited to remove unwanted

^{87}Rb atoms in the $|F = 2, m_F = 1\rangle$ state that have not been transferred by the spin polarization pulse.

After the molasses, atoms are recaptured in a quadrupole field whose gradient is low enough such that only ^{87}Rb atoms in the $m_F = 2$ state stay trapped. This cleaning method does, however, not work for ^{39}K due to its much lighter mass and we have to rely on a good efficiency of the spin polarization pulse for ^{39}K. In fact, we found that the spin polarization efficiency of ^{39}K dramatically changed during the day due to polarization drifts of the spin polarization beam which were induced by the acousto-optic modulator (AOM) that switches the power of the beam. We found that these polarization drifts heavily depend on the temperature of the AOM, leading to strong fluctuations in the resulting ^{39}K atom number. We circumvented this problem by actively stabilizing the power of the spin polarization pulse on the experimental table with a standard closed-loop PID controller.

After the spin polarization pulse, the atoms are transported into the science cell by a magnetic transport [141]. During this transport, we lose about 80% of the ^{87}Rb atoms and more than 90% of the ^{39}K atoms. Most atoms get lost while entering the differential pumping section between the MOT chamber and the science cell. This is most likely due to the small radius of the differential pumping section together with a small mismatch between the centers of the differential pumping section and the quadrupole trap. Nevertheless, we can transport enough atoms to get large BECs of both ^{87}Rb and ^{39}K[4].

Once the atoms arrive in the science cell, we further cool them down by forced microwave evaporation in a plugged quadrupole trap. To prevent Majorana losses, the center of the quadrupole trap is plugged with a blue-detuned laser beam [15, 142]. Owing to the large differences in the hyperfine splitting between the $|F = 2\rangle$ and $|F = 1\rangle$ ground state manifold of ^{39}K and ^{87}Rb, see Fig. 3.5, we can selectively remove ^{87}Rb atoms from the quadrupole trap by driving the microwave transition between the trapped $|F = 2, m_F = 2\rangle$ state and the anti-trapped state $|F = 1, m_F = 1\rangle$. The ^{39}K atoms are sympathetically cooled by the ^{87}Rb atoms during this part of the evaporation. As the inter-species scattering length is rather small with $a_{\text{Rb-K}} = 36a_0$, where a_0 is Bohr's radius, the evaporation becomes inefficient when reaching the low μK regime [143]. Additionally, this small inter-species scattering length demands a slow evaporation ramp, of in our case 11 s, to keep both species in thermal equilibrium.

3.2.3 Evaporative cooling in an optical dipole trap

At the end of the microwave evaporation, we transfer the atoms into a crossed-beam dipole trap at a wavelength of $\lambda_D = 1064\,\text{nm}$. The loading of the dipole trap is done

[4] We were also able to create a degenerate Fermi gas of approximately 3×10^5 ^{40}K atoms at a temperature of $T \sim 0.15T_F$, where T_F is the Fermi temperature. For more details see [89]

by slowly increasing the power of the dipole beams and lowering the gradient of the quadrupole trap at the same time. To ensure that the atoms remain spin-polarized in the dipole trap we turn on a weak offset field of $1\,G$ along the vertical direction, before completely turning off the quadrupole trap. To avoid inelastic spin-changing collisions during the evaporation in the dipole trap, we transfer both species into their absolute ground state $|F = 1, m_F = 1\rangle$ via a microwave sweep for ^{87}Rb and a RF-sweep for ^{39}K. To remove atoms that have not been transferred into the $F = 1$ manifold, we shine in a light pulse that is resonant on the $F = 2 \rightarrow F' = 3$ transition.

Compared to the quadrupole trap one has the advantage that one can tune the interactions between ^{87}Rb and ^{39}K in the dipole trap via a broad Feshbach resonance at around $318\,G$ [144], see Fig. 3.6 (a) and section 3.2.4. We increase the scattering length between ^{87}Rb and ^{39}K to $a_{\text{Rb-K}} \sim 90\,a_0$ and continue the evaporation by lowering the intensities of the dipole beams. As ^{87}Rb is almost twice as heavy as ^{39}K, it experiences a shallower trapping potential than ^{39}K and we can again selectively remove ^{87}Rb atoms from the trap. Once almost all ^{87}Rb atoms are evaporated from the trap we change the magnetic field to address the Feshbach resonance for ^{39}K atoms at around $400\,G$ [145], see Fig. 3.6 (a). In the last step of the evaporation, we increase the scattering length to $a_{\text{K-K}} = 150\,a_0$ and continue the evaporation with ^{39}K alone. Since during most parts of the evaporation ^{39}K is sympathetically cooled by ^{87}Rb only a comparatively small amount of ^{39}K atoms are lost during the evaporation.

At the end of the evaporation, we reduce the scattering length to $a_{\text{K-K}} = 45\,a_0$ to avoid unnecessary losses while holding the atoms in the shallow dipole trap. To make the trapping potential along the horizontal directions more homogeneous and less sensitive to the overlap between the two other dipole beams, we ramp up the intensity of a third beam that propagates along the vertical direction. This beam has a waist of approximately $130\,\mu$m. After a hold time of 550 ms in the shallow dipole trap we ramp the scattering length in 50 ms to its desired value. We have checked that this ramping duration is long enough to not induce any breathing motions of the BEC [146, 147]. Furthermore, we have verified that no atoms are lost during the ramp of the Feshbach field. Finally, after having set the scattering length of the atoms, we adiabatically ramp up the lattice beams in 100 ms to the desired lattice depth. Afterwards, the atoms occupy the lowest energy band of the lattice at zero quasimomentum.

3.2.4 Feshbach resonances

Feshbach resonances are a useful tool for cold atoms experiments to tune the scattering length a and thus the interaction strength between atoms [148, 149]. The underlying physical concept of a Feshbach resonance is illustrated in Fig. 3.6 (b).

Consider two different molecular potential curves that describe the interaction between two particles. The lower lying curve represents the so-called open or entrance

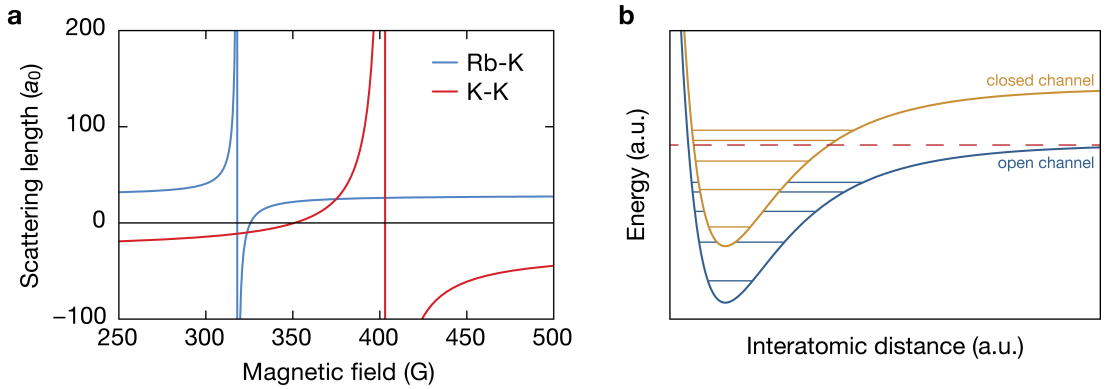

Figure 3.6: **Feshbach resonance.** **(a)** Calculated scattering lengths between ^{87}Rb and ^{39}K in their absolute ground state $|F = 1, m_F = 1\rangle$ are shown by the blue line. The red line shows the calculated intraspecies scattering lengths between ^{39}K atoms in their absolute ground state. **(b)** Two molecular potentials are illustrated in orange and blue for the closed and open channel, respectively. At ultracold temperatures, the total energy of the colliding atoms lies just above the asymptotic value of the open channel and is illustrated by the red dashed line. The closed channel potential can be moved relative to the open channel via a magnetic offset field. If the energy of a bound state in the closed channel approaches the total energy of the scattering atoms, a strong coupling between the two channels arises which leads to an enhanced scattering length.

channel, which asymptotically connects to two free atoms for large interatomic separations. Since the kinetic energy of two ultracold colliding atoms is very small, their total energy will lie just above the asymptotic value of the open channel. The other potential curve represents the so-called closed channel, whose asymptotic energy lies above the total energy of the colliding atoms. Suppose that this channel possesses bound molecular states close to the asymptotic value of the open channel. If the spin arrangement of the two atoms in this channel is different to the one in the open channel but has the same total projection onto the quantization axis, it will possess a different magnetic moment than the open channel. Thereby, one can shift the energy levels of the bound molecular levels and the continuum level with respect to each other by applying an external homogeneous magnetic field.

A Feshbach resonance occurs whenever the energy of a bound molecular level in the closed channel matches the energy of the colliding atoms [150]. In this case, even a weak coupling between the two channels leads to a strong enhancement of the scattering length which diverges directly on resonance [151, 152]. For a magnetically tunable Feshbach resonance, the dependence of the s-wave scattering length on the applied magnetic field is described by [153]

$$a(B) = a_{bg}\left(1 - \frac{\Delta}{B - B_0}\right), \tag{3.12}$$

where a_{bg} is the background scattering length, Δ is the width of the resonance and B_0 is the position of the resonance.

3.3 Detection and manipulation techniques

In order to obtain information about the atoms, one needs to take an image of them. At first, we will describe the absorption imaging technique were one images the shadow that is cast by the atoms on a camera. Afterwards, we will describe what one has to consider when imaging atoms at a large magnetic offset field. We continue by showing two different methods with which one can determine the state of the atoms in the lattice. Concluding this section, we will delineate how atoms can be moved within the band structure by accelerating the lattice structure.

3.3.1 Absorption imaging

To determine the spatial density distribution of a BEC one has to take an image of the atoms. One of the most common imaging techniques is absorption imaging [28], where a resonant light beam is shone onto the atoms and the shadow cast by the illuminated BEC is imaged by a charge-coupled-device (CCD) camera. If the intensity of the imaging beam is much weaker than the saturation intensity I_S of

the chosen atomic transition, one can describe the intensity profile of the imaging beam after having passed through the BEC by the Lambert-Beer law [154]

$$\begin{aligned} I(x,y) &= I_0 e^{-\sigma_0 \int n(x,y,z)\mathrm{d}z} \\ &= I_0 e^{-\sigma_0 n_{\mathrm{col}}(x,y)}. \end{aligned} \tag{3.13}$$

Here we have assumed that the imaging beam propagates along the z-direction and that the density of the condensate is described by $n(x,y,z)$. For a two-level atom, the resonant scattering cross section is given by $\sigma_0 = 3\lambda^2/2\pi$. Thus, the local column density $n_{\mathrm{col}}(x,y)$ is given by

$$n_{\mathrm{col}}(x,y) = -\frac{1}{\sigma_0} \ln \frac{I_f(x,y)}{I_i(x,y)}. \tag{3.14}$$

To extract the column density a total of four images are taken with the CCD camera. In the first image $\mathcal{I}_1$, the atoms are present and the imaging beam is on. Afterwards, we take a second picture $\mathcal{I}_2$, where we only turn on the imaging beam but no atoms are present. In addition, we take two dark images where we do not turn the imaging beam on. These dark images are then subtracted from their corresponding images $\mathcal{I}_1$ and $\mathcal{I}_2$ to be able to remove any stray light from the pictures that might fall onto the camera. After the subtraction of the stray light, the images exhibit the intensity distributions $I_f(x,y)$ with atoms and $I_i(x,y)$ without atoms.

As we will see in chapter 3.4.2, it is sometimes necessary to image the atoms with intensities much larger than the saturation intensity. In this case, the local column density defined in Eq. 3.14 gets modified and reads [155]

$$n_{\mathrm{col}}(x,y) = -\alpha \ln \frac{I_f(x,y)}{I_i(x,y)} + \frac{I_i(x,y) - I_f(x,y)}{I_S}. \tag{3.15}$$

Here, the dimensionless quantity α accounts for multiple corrections of the resonant scattering cross section σ_0. These corrections include experimental imperfections, as for example impurities of the polarization of the imaging beam but also takes into account that the level structure of the atom in the ground as well as in the excited state manifold of the optical transition is more complicated than a two-level atom.

As the camera only counts the number of photons that reach the CCD chip one can recast Eq. 3.15 in terms of the counts $\mathcal{C}$ per pixel as

$$n_{\mathrm{col}}(x,y) = -\alpha^* \ln \frac{\mathcal{C}_f(x,y)}{\mathcal{C}_i(x,y)} + \beta^*(\mathcal{C}_i(x,y) - \mathcal{C}_f(x,y)). \tag{3.16}$$

A thorough determination of the absolute values of α^* and β^* is tedious and great care has to be taken in calibrating filters and photon number losses in the imaging path [155]. However, this calibration can be simplified when imaging a cloud of

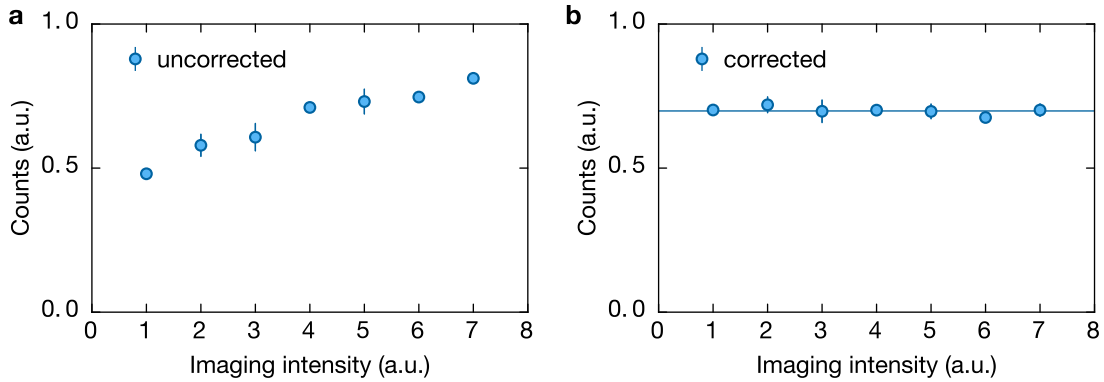

Figure 3.7: **Calibration of high intensity imaging. (a)** Sum of pixel values when analyzing the data according to Eq. 3.14. Even though the actual atom number is constant for all imaging intensities, one obtains different numbers of counts for different imaging intensities. **(b)** Sum of pixel values when analyzing the data according to Eq. 3.16. Now the number of measured counts stays constant when varying the imaging intensity. Counts in (a) and (b) have been scaled to lie within the same interval. Error bars indicate the standard error of the mean from at least three measurements per data point and the solid line is a guide to the eye.

well-known density [156]. The main purpose of high-intensity imaging for us is the determination of the atom number from *in-situ* measurements, see section 3.4.2, where it is important to keep the imaging duration as short as possible. Since we only need the correct cloud shape but not the absolute value of the column density to extract the atom number it is sufficient to determine the fraction α^*/β^*.

The correct ratio of α^*/β^* leads to an imaging intensity independent value of $n_{\mathrm{col}}(x, y)$ and is determined by imaging the atomic cloud with different intensities of the imaging beam. This calibration technique requires that the total number of scattered photons needs to be small to not heat or push the cloud. To this end we keep the imaging duration below $4.5\,\mu$s where the diffusive expansion of the cloud (see also section 3.4.2 and Fig. 3.14) is still well below the resolution limit of approximately $1\,\mu$m of our objective [89]. Figure 3.7 (a) shows the measured counts of pixel values when evaluating the pictures according to the low intensity expression defined in Eq. 3.14. By taking into account the high intensity corrections according to Eq. 3.16 the number of pixel counts stays constant for different imaging intensities, see Fig. 3.7 (b).

Depending on which quantity we want to extract from the images, there are two main options on when to take the image of the atoms. One can either image them *in-situ* or one can release them from all trapping potentials and image them after a certain time-of-flight (TOF), during which the atoms can expand freely. The former method can be used to determine the real space density distribution of the BEC

inside the trap which has been exploited to study, for example, the incompressibility of fermionic or bosonic Mott insulators [157, 158]. *In-situ* imaging has also been used to measure density-density correlation functions [31, 159–161] or to extract various equations of state [162–164]. We use *in-situ* imaging to determine the atom number of the condensate from a measurement of the Thomas-Fermi radius, see section 3.4.2. Whilst the resolution of approximately 1 μm of our imaging system is too small to resolve single lattice sites, other experiments have been realized already a few years ago where single-site resolution of bosonic atoms is feasible [31, 32, 165]. Recently, only within a few months, several experiments also succeeded to image fermionic atoms on the single-site level [33–37].

TOF pictures, on the other hand, exhibit the momentum distribution of the cloud. For a sufficiently long TOF, the cloud width directly reveals the momentum distribution of the BEC inside the trap. This so-called far-field is reached once the cloud width in TOF is large compared to the initial cloud size inside the trap. For the typical TOF used in this thesis, this condition is not fulfilled and the resulting absorption image will be a convolution between real space and momentum space. Nevertheless, TOF imaging is used later on to reliably differentiate between condensed atoms with a quasimomentum close to $\boldsymbol{q} = 0$ and excited thermal atoms which have a quasimomentum that is usually much larger than zero, see chapter 5. Other application areas of TOF imaging in our experiment are for example the calibration of the lattice depth, see section 3.4.3, or the balancing of the lattice beam powers, see section 3.3.3.

3.3.2 High magnetic field imaging

To determine the atom number of our system, see chapter 3.4.2, we take *in-situ* images of the condensate in the dipole trap and measure its Thomas-Fermi radius for different scattering lengths. This measurement requires that one has to image the atoms in the presence of a large magnetic offset field of $B \sim 400\,\mathrm{G}$. For weak magnetic fields, the coupling between the total electron angular momentum $\hat{J}$ and nuclear angular momentum $\hat{I}$ results in the total atomic angular momentum $\hat{F} = \hat{J} + \hat{I}$. The magnitude of $\hat{F}$ can take values between

$$|J - I| \leq F \leq J + I \tag{3.17}$$

where F, J and I are the quantum numbers associated with the operators $\hat{F}$, $\hat{J}$ and $\hat{I}$. For weak magnetic fields, where F is still a good quantum number, the energy shift of the different m_F sublevels is given by Eq. 3.11. However, for large magnetic fields, when the energy shift becomes larger than the hyperfine energy shift[5] [138]

[5]Note that we will neglect terms proportional to the magnetic quadrupole constant and higher lying terms since they are at least two orders of magnitude smaller than the magnetic dipole constant [139].

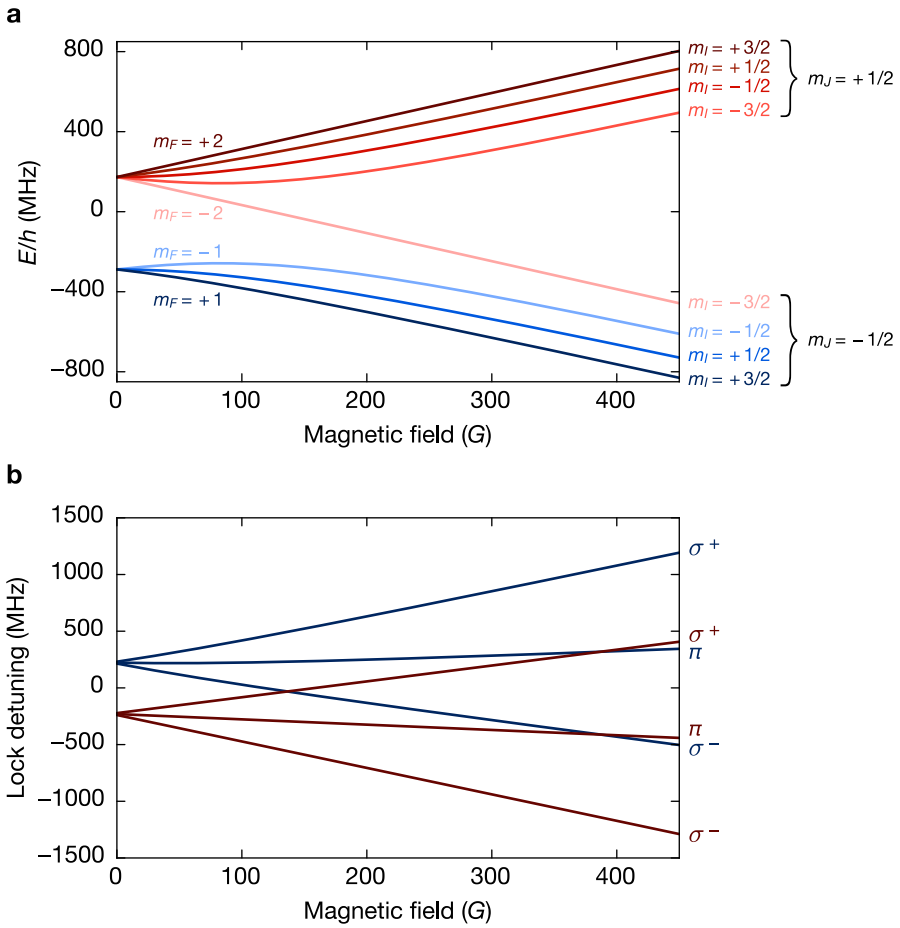

Figure 3.8: **Level scheme of ^{39}K in an external magnetic field. (a)** Ground level hyperfine structure of ^{39}K in an external magnetic field. For small magnetic fields, the levels are grouped according to their F value. Blue colors correspond to states in the $F = 1$ manifold and red colors to states in the $F = 2$ manifold. The lightness of the curves illustrate the different m_F sublevels. For large magnetic fields in the hyperfine Paschen-Back regime, the levels group according to their m_J value. **(b)** Laser lock detunings for two relevant states from the ground state manifold to states in the excited state manifold. Since the imaging light keeps the nuclear angular momentum unaffected, only states with $\Delta m_J = 0, \pm 1$ can be addressed by the imaging light with respective polarizations of $\pi, \sigma^{\pm}$. The color coding is the same as in (a) with the blue lines corresponding to the state $|F = 1, m_F = 1\rangle$ (repumper transition at zero field) and the red lines to the state $|F = 2, m_F = 2\rangle$ (imaging transition at zero magnetic field). The three branches show the detunings for different laser light polarizations. In the experiment, we use the lowest (σ^-) blue branch for imaging since it addresses a cyclic transition.

$$\Delta E_{\text{hfs}} = \frac{1}{2} A_{\text{hfs}}(F(F+1) - I(I+1) - J(J+1)), \tag{3.18}$$

with A_{hfs} being the magnetic dipole constant, F will not be a good quantum number anymore. In this regime, the electron and nuclear angular momenta decouple and the good quantum numbers are given by J and I. The energy shift is now given by the (hyperfine) Paschen-Back formula [138]

$$E_{PB}(B) = A_{\text{hfs}} m_J m_I + \mu_B (g_J m_J + g_I m_I) B. \tag{3.19}$$

For intermediate magnetic field strengths, the energy shift cannot, in general, be calculated easily. However, in the case of $J = 1/2$, which applies to the $4^2S_{1/2}$ ground state manifold of ^{39}K, there exists an analytical expression of the energy shift, the so-called Breit-Rabi formula [166]

$$E_{BR} = -\frac{A_{\text{hfs}}}{4} + g_I \mu_B m_F B \pm \frac{A_{\text{hfs}}(I+1/2)}{2} \left(1 + \frac{4 m_F X}{2I+1} + X^2\right)^{1/2}, \tag{3.20}$$

with the sign convention $m_F = m_I \pm m_J$ and

$$X = \frac{(g_J - g_I)\mu_B B}{A_{\text{hfs}}(I+1/2)}. \tag{3.21}$$

Figure 3.8 (a) shows the level structure of the ground state manifold of ^{39}K in the relevant magnetic field range of our experiment. For large magnetic fields, one can see that the states regroup according to their electron angular momentum.

As we have seen in section 3.2.3, the ^{39}K atoms are prepared in their absolute ground state $|F = 1, m_F = 1\rangle$. At large magnetic fields this state is represented by $|m_J = -1/2, m_I = +3/2\rangle$. Since the imaging light does not change the nuclear angular momentum of the atoms, only states in the $4^2P_{3/2}$ excited state manifold with $m_J = -3/2, \pm 1/2$ and $m_I = +3/2$ can be addressed by the imaging light. Figure 3.8 (b) shows the corresponding lock detunings of the imaging laser (negative lock detunings) and repump laser (positive lock detuning) compared to the reference laser of ^{39}K. The blue lines show the necessary laser detunings to address atoms originally in the $|F = 1, m_F = 1\rangle$ manifold. For high-field imaging, we use the lowest branch which is addressed by laser light with σ^- polarization. This has two advantages: first of all the transition $|m_J = -1/2, m_I = +3/2\rangle \rightarrow |m'_J = -3/2, m'_I = +3/2\rangle$ is cyclic since atoms from the excited state manifold can only decay back into the state $|m_J = -1/2, m_I = +3/2\rangle$ whereas the other possible decay into $|m_J = +1/2, m_I = +3/2\rangle$ in the ground state manifold is dipole forbidden. For completeness, the lock frequencies for this state are shown in red, see Fig. 3.8 (b). Setting up a beam that addresses the transition from

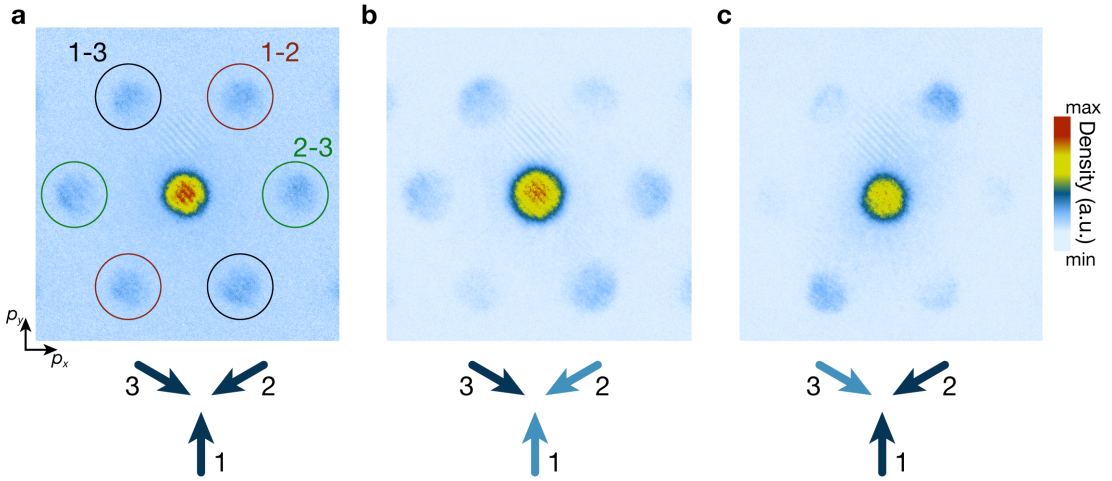

Figure 3.9: **Beam power balancing.** The images show TOF pictures of the condensate after a sudden shut-off of all confining potentials. **(a)** For balanced lattice beam intensities at the atoms position, the plane wave coefficients $c_n^{(b,q)}$ for each pairwise combination of beams have the same magnitude, leading to equal populations in each Bragg peak. The different pairs of Bragg peaks, resulting from the interference of their corresponding lattice beams, are encircled with different colors. **(b)** If for example, beam 3 is stronger, indicated by the darker colored arrow than the other two beams, the pairs of Bragg peaks which include contributions from beam 3 will be more pronounced than the Bragg peaks resulting from the interference of beams 1 and 2. **(c)** Vice versa, a lower intensity of beam 3 will lead to less pronounced Bragg peaks.

$|m_J = +1/2, m_I = +3/2\rangle$ to $|m_J = -1/2, m_I = +3/2\rangle$ in the excited state manifold could serve as a possible repump beam if needed in the future. The second and rather technical advantage of using σ^- polarized light is that we can directly use the imaging beam to address the atoms without the need of an additional repump laser. For imaging the atoms at zero magnetic field the atoms first have to be pumped into the $F = 2$ manifold by a repump laser since the imaging happens on the $F = 2 \rightarrow F' = 3$ transition, see Fig. 3.5.

3.3.3 Lattice detection: free-space projection and power balancing

In section 2.2.1 we have shown that the eigenstates of a single particle in a lattice structure are given by Bloch states as defined in Eq. 2.26. In a simplified picture, we can assume that a condensate occupies such a single Bloch state in the lattice. When suddenly switching off all trapping potentials this Bloch state gets projected onto the

real space momentum states which are given by plane waves. Consequently, as the Bloch state is composed of a sum of plane waves shifted by reciprocal lattice vectors, when imaging the atoms after a certain TOF one only observes atoms at distinct momenta that are separated from each other by a reciprocal lattice vector[6]. The fractional number of atoms in each momentum peak, which are commonly referred to as Bragg peaks, directly represents the magnitude of the plane wave coefficients $c_n^{(b,q)}$ of the Bloch wave, defined in Eq. 2.27.

This property can be used to balance the intensities of the lattice beams at the position of the atoms. For all experiments conducted in this thesis, it is desirable to work in a well-balanced lattice structure. This means that the intensity profiles of all lattice beams at the atoms positions should be equal. The correct balancing between all three lattice beams can be determined by adiabatically loading the BEC into the honeycomb lattice at $q = \Gamma$, followed by a sudden shut-off of all trapping potentials. If the lattice is well balanced, the plane wave coefficients have the same magnitude for all pairs of lattice beams, which consequently results in Bragg peaks of equal magnitude. If one beam is weaker than the other two beams the plane wave decomposition will not be symmetric anymore. The lattice potential created by the interference of the two stronger beams will be deeper than the lattice potential created by the interference of the stronger beams with the weaker beam. Hence, the two Bragg peaks resulting from the interference of the stronger beams will have a larger magnitude than the other four Bragg peaks, see Fig. 3.9. With this method, a power imbalance between the beams of more than 5% can reliably be detected. The lattice is rebalanced every day to compensate for slow drifts in the pointing of the lattice beams.

Keep in mind that the plane wave decomposition of the Bloch states was formulated for single particles. Hence, the Bragg peaks are only visible for a phase coherent BEC that macroscopically occupies a single particle eigenstate. For very deep lattices each lattice site can be regarded as isolated from its environment and the phase coherence of atoms on different lattice sites will get lost, resulting in the vanishing of the Bragg peaks. This property was used to probe the superfluid to Mott insulator transition [21] or generally probe the phase coherence of a lattice system [167, 170–172].

[6]Note that this simplified picture does not take into account the real space distribution of the BEC. To intuitively understand how the real space extent of the BEC will affect the Bragg peaks one can compare this situation to the well-known interference pattern created by a grating illuminated by a laser beam. The envelope of the interference pattern is given by the slit size of the grating, whereas the sharpness of each interference peak will increase for larger beam sizes or consequently an increasing number of illuminated slits of the grating. The analogon of the slit size is the extent of the Wannier function in the lattice, whereas the analogon of the laser beam size is the real space extent of the BEC. More information on how the real space extent of the BEC affects the Bragg peaks can be found, for example, in [167, 168]. For a complete description of the TOF pattern also the finite TOF has to be taken into account, analogously to the near-field diffraction regime in optics [169].

3.3.4 Lattice detection: band mapping

Another detection technique for atoms trapped in an optical lattice is called band mapping. Here the power of the lattice beams is ramped down slowly compared to the band gap to higher lying bands but fast compared to the tunneling matrix element of the band the atoms are occupying [170, 173]. These conditions ensure that no atoms are transferred between individual bands during the band mapping process and that atoms have no time to redistribute their quasimomentum within the band they are occupying. Hence, the band structure of the lattice is adiabatically transferred to the free space dispersion relation. Atoms with a quasimomentum q that are initially located in the bth band of the lattice are mapped onto a state with real space momentum $|p| = |q| + \hbar k_L(b-1)$ in the b^{th} Brillouin zone which is illustrated in Fig. 3.10. Thus, the band mapped pictures directly show which band and what quasimomentum the atoms were occupying the lattice. However, there is also a caveat as some momentum states in different bands are mapped onto the same free space momentum state and are thus indistinguishable from each other, see Fig. 3.10. Another limitation is the real space extent of the BEC which is illustrated in Fig. 3.10 (c). Due to the rather short TOF of only 3.5 ms, which was chosen here to be able to resolve multiple Brillouin zones at once, the real space extent of the BEC almost covers half of the Brillouin zone. Whereas it was sufficient in this case to reliably determine between atoms in the different bands, a proper determination of the actual quasimomentum of the particles within the Brillouin zone is hampered. To resolve the quasimomentum distribution within a single band, a longer TOF has to be chosen which increases the resolution in momentum space.

Band mapping together with a long TOF of 15 ms is our standard technique to determine the remaining atom number in the condensate after a certain shaking duration, see section 4.3.1. At this TOF the spatial extent of the first Brillouin zone is on the order of the chip size of the CCD camera.

3.3.5 Lattice manipulation: homogeneous force and periodic driving

In section 3.1.3 we have shown how a one-dimensional optical lattice potential can be created by interfering two free-running laser beams. If the two laser beams have equal frequencies one obtains a static lattice potential. For a fixed frequency difference between the two beams, the lattice potential will move with a constant velocity in space. From Eq. 3.8 one can see that the lattice potential will have moved by the lattice spacing d, whenever the phase difference between the two beams becomes $\Delta\omega t/2 = \pi$. Consequently, the lattice is moving with a constant velocity of

$$v_L = d\frac{\Delta\omega}{2\pi} = d\Delta\nu, \tag{3.22}$$

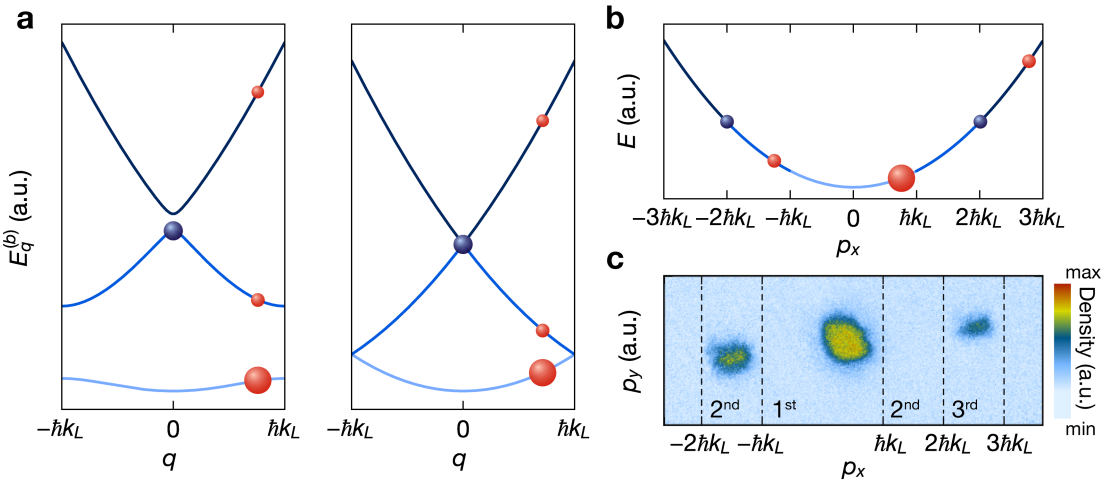

Figure 3.10: **Band mapping. (a)** The left plot shows two condensates, indicated by the red and blue spheres, occupying two different momentum states in an optical lattice. While the blue atoms sit at a quasimomentum $q = 0$ in the second band, the red atoms sit at a quasimomentum $q > 0$ with some additional population in the second and third band, indicated by the smaller red spheres. When band mapping these atoms, they are adiabatically transferred to the free-particle momentum states (right plot). **(b)** Extended zone scheme of the free space dispersion relation of (a). One can see that atoms initially in the first excited band are mapped onto the second Brillouin zone in the extended zone scheme whereas atoms initially in the second excited band are mapped onto the third Brillouin zone. However, the mapping is not always unambiguous, as can be seen for the blue atoms. Whereas their momentum is well-defined one cannot distinguish if the atoms were initially in the second or third band. **(c)** Absorption image of a BEC with a similar quasimomentum and band occupation as indicated by the red spheres in (a) and (b). The image has been taken after 3.5 ms TOF. The dashed lines mark the Brillouin zone edges. One can clearly distinguish between atoms in the first, second and third band even though the real space extent of the condensate still dominates over its momentum distribution.

with $\Delta\nu = 2\pi\Delta\omega$. We can tune the frequency of each lattice beam via individual acousto-optic modulators[7]. If the frequency difference between the beams is linearly changing in time, the lattice is accelerated with a constant acceleration. In this case, the atoms will feel a constant force along the lattice direction in the reference frame co-moving with the lattice. To understand the origin of this force, let us write down the Hamiltonian in the lab frame as

$$\hat{H}(t) = \frac{\hat{p}^2}{2M} + V_L(\hat{x} - x(t)). \tag{3.23}$$

Here $\hat{p}$ and $\hat{x}$ are the momentum and position operators, respectively and $V_L(x)$ is the lattice potential at $t = 0$ with $x(t) = v_L t$. To project the Hamiltonian into the frame co-moving with the lattice, one has to perform a unitary transformation with

$$\hat{U}(t) = e^{-iM\dot{x}(t)\hat{x}/\hbar} e^{ix(t)\hat{p}/\hbar}. \tag{3.24}$$

This transformation takes into account that both the position as well as the momentum of the atoms are changing. The wave function in the frame co-moving with the lattice is then given by $\tilde{\psi} = \hat{U}\psi$ obeying the time-dependent Schrödinger equation $i\hbar\dot{\tilde{\psi}} = \tilde{H}\tilde{\psi}$. The Hamiltonian $\tilde{H}$ is given by

$$\tilde{H} = \hat{U}\hat{H}\hat{U}^\dagger + i\hbar\dot{\hat{U}}\hat{U}^\dagger = \frac{\hat{p}^2}{2M} + V_L(x) + M\ddot{x}(t)\cdot\hat{x} - \frac{M\dot{x}(t)^2}{2}. \tag{3.25}$$

Here the last term $M\dot{x}(t)^2/2$ describes the energy offset arising from the kinetic energy of the atoms in the moving lattice and the term $F_x(t) = -M\ddot{x}(t)$ describes the force the atoms experience in the frame co-moving with the lattice. Hence, we can write down the magnitude of the force the atoms experience due to the accelerating lattice as

$$F(t) = M\frac{\partial v_L}{\partial t} = Md\frac{\Delta\nu}{\Delta t}. \tag{3.26}$$

Since the momentum of the atoms is restricted to values within the first Brillouin zone one can observe Bloch oscillations in momentum space when applying a constant force F [174]. We will use these Bloch oscillations later in section 3.4.4 to determine the momentum spread of the condensate. Note that the detection of the atoms after a certain TOF happens in the lab frame and not in the frame co-moving with the lattice. Therefore, the atoms seem to stay stationary in the images at first until they acquire a momentum large enough to get Bragg reflected at the Brillouin zone edge, see Fig. 3.11. This can be understood by looking at Eq. 3.25 again. The force the atoms feel inside the accelerated lattice $F_x(t) = -M\ddot{x}(t)$ is opposite to the movement of the lattice. Since their real space momentum is a combination of their quasimomentum and the momentum they acquire due to the moving lattice

[7]For details on the lattice setup refer to [89].

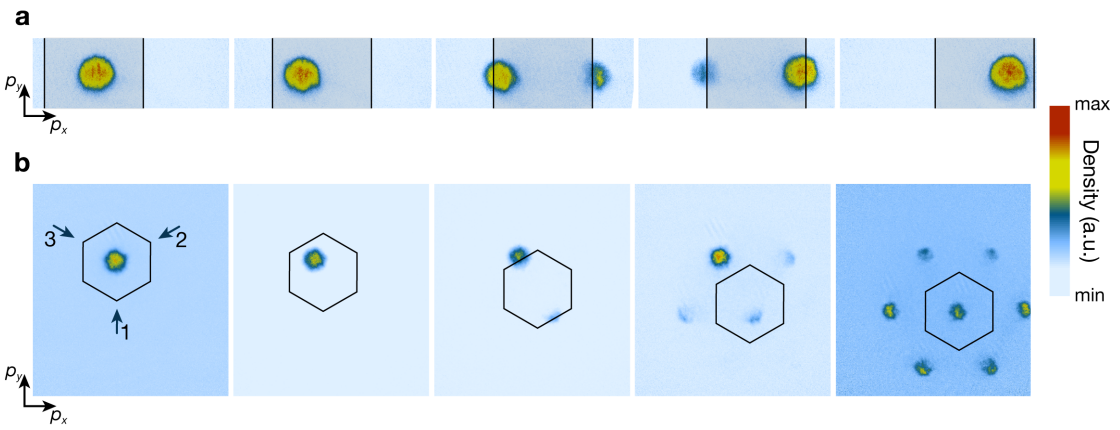

Figure 3.11: **Bloch oscillations.** **(a)** Adiabatic Bloch oscillations in a one-dimensional lattice. The images are obtained by band mapping the atoms and image them after TOF. The first Brillouin zone is highlighted by the gray shading and the borders are illustrated by the black lines. For quasimomenta q smaller than $\hbar k_L$ the atoms seem stationary as the lattice acceleration moves the Brillouin zone. Once the atoms reach the zone edge they get Bragg reflected (second and third picture). Afterwards, they seem stationary again until they reach the next zone edge. **(b)** Non-adiabatic Bloch oscillations in a honeycomb lattice. The images are obtained by band mapping the atoms. By changing the frequencies of beam 1 and 3 in opposite directions one can accelerate the atoms towards the M point. The lattice beams are depicted as dark blue arrows in the left picture. The acceleration was chosen such that a large fraction of the condensate gets excited to the second band in the vicinity of the Brillouin zone edge.

they seem stationary until they reach the Brillouin zone edge. There the atoms get Bragg reflected to the opposite zone edge which results in a sudden change of the real space momentum which can be detected in TOF images. Now the atoms seem stationary again until they reach the next Brillouin zone edge.

The discussion so far focused on a constant acceleration of the lattice. To shake the position of the lattice, the frequency difference between the beams is periodically modulated by $\Delta\nu = \nu_0 \sin(\omega t)$, where ν_0 is the frequency amplitude of the drive. Hence the atoms will feel a periodic force

$$F_x(t) = M d \nu_0 \omega \cos(\omega t) = F_0 \cos(\omega t) \tag{3.27}$$

In section 2.3.5 it was shown that the relevant parameter which determines the effect of the shaking on the band structure is the driving strength α. In terms of

the experimental shaking parameters it is given by

$$\alpha = \frac{Md^2\nu_0}{\hbar} = \frac{\hbar\pi^2}{2E_r}\nu_0. \tag{3.28}$$

Creating a force on the atoms via lattice acceleration also works in the honeycomb lattice. Here, the acceleration will be along the propagation direction of the beam whose frequency is modulated in time. By changing the frequency of two beams simultaneously one can accelerate the atoms in any arbitrary direction in the lattice plane. For example by changing the frequency of beam 1 as fast as for beam 3 but in the opposite direction the atoms get accelerated towards the M point, see Fig. 3.11 (b). Furthermore, by sinusoidally changing the frequency of two beams with a phase offset of 60° to each other one can shake the atoms along a circular path.

3.4 Characterization of the experimental setup

In this section, we will characterize the most important properties of our system. We start by measuring the harmonic trapping frequencies in the dipole trap, as they will be a necessary ingredient in the determination of the total atom number in our system. By taking *in-situ* images of the condensate we can determine the Thomas-Fermi radius of the cloud from which we can infer the total atom number. We will then show different methods to determine the lattice depth. In the last part of this section, we will describe how the momentum spread of the condensate can be measured via Bloch oscillations.

3.4.1 Determination of the harmonic trapping frequencies

The harmonic trapping frequencies of the dipole trap will play a crucial part in the method used to determine the atom number of our system, see section 3.4.2. Furthermore, the trapping frequencies in the presence of the one-dimensional lattice will be crucial in the calculation of the theoretically expected scattering rates in a periodically driven optical lattice, see section 4.2.4.

In section 3.1.2 we saw that the central part of the dipole trap potential can be approximated by a harmonic oscillator potential, which in turn is characterized by its harmonic trapping frequencies. We can measure these trapping frequencies by exciting a sloshing motion of the BEC inside the dipole trap. To this end we slowly ramp up the power of one of the two dipole beams, effectively creating an elliptic trapping potential. Then, by quickly ramping the power of the beam back to its normal value, which results in an almost sudden change in the trapping geometry, the atoms experience a kick and start oscillating in the potential. We observe this oscillating motion by taking TOF pictures of the BEC for different hold durations

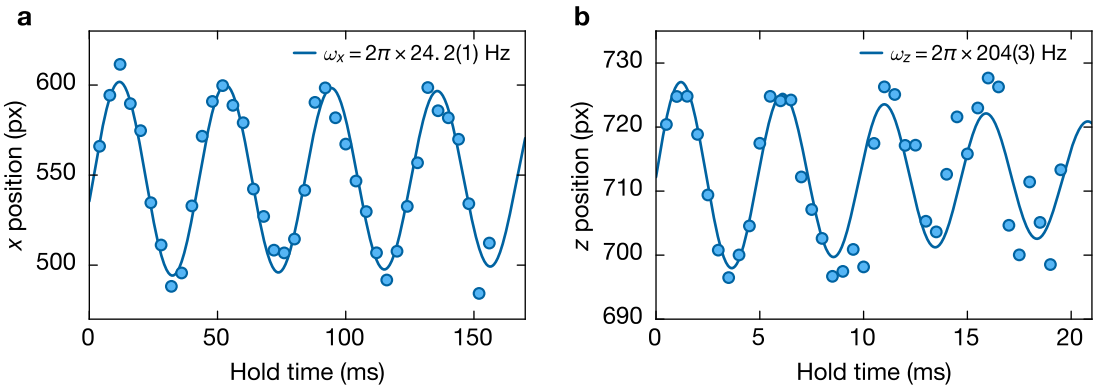

Figure 3.12: **Calibration of the harmonic trapping frequencies. (a)** Measured position of the BEC along the x-axis after giving it a kick within the dipole trap. By fitting the data with a sinusoidal function, one can extract the harmonic trapping frequencies of the dipole trap. **(b)** Oscillations along the z-axis after giving the atoms a kick in the dipole trap. Due to the ellipticity of the dipole trap beams the trapping frequency along the vertical direction is almost a factor of 10 larger than in the horizontal plane.

in the dipole trap. Figure 3.12 (a) shows the obtained data along the horizontal x-direction. We measure frequencies of $\omega_x = 2\pi \times 24.2(1)$ Hz and $\omega_y = 2\pi \times 27.6(4)$ Hz. The trapping frequency along the vertical direction is measured by imaging the atoms from the side. Due to the large asymmetry of the trapping potential, the trapping frequency along the vertical direction is almost a factor of ten larger than in the horizontal direction and we measure a frequency of $\omega_z = 2\pi \times 204(3)$ Hz, see Fig. 3.12 (b).

To calculate the theoretically expected scattering rates in a shaken one-dimensional lattice, see section 4.2.4, one needs to determine the harmonic trapping frequencies in the presence of the optical lattice. Due to the anti-confinement induced by the spatially-dependent lattice potential, the harmonic trapping frequencies in the presence of the lattice will be smaller than the ones in the dipole trap alone. However, the technique of kicking the atoms to determine the harmonic trapping frequencies only works for the vertical direction, where no lattice potential is present. In this direction we measure a frequency of $\omega_z = 2\pi \times 186(3)$ Hz. In the horizontal directions, the induced oscillations damp very quickly which makes it impossible to extract the trapping frequencies reliably. To determine the horizontal trapping frequency perpendicular to the lattice direction, we model the anti-confinement induced by the lattice. In the center of the trap, the spatial dependence of the lattice depth can be described by

$$V(y) = V_0 e^{-2y^2/w_{L,y}^2}, \tag{3.29}$$

where $w_{L,y}$ is the projection of the waists of the two lattice beams onto the y-axis, see inset Fig. 3.13 (b). Figure 3.13 (a) shows the spatial dependence of the energies of the lowest two bands along the y-axis for an 11 E_r deep lattice. One can see that the bandwidth increases away from the trap center due to the decreasing lattice depth induced by the Gaussian beam shape of the lattice beams. This effect leads to an effective anti-confinement. To visualize this anti-confining effect, also the pure dipole trap potential is plotted in Fig. 3.13 (a). Note that this type of anti-confinement appears for red and blue-detuned lattices. However, in a red-detuned lattice, atoms sit at the intensity maxima and therefore experience an additional confining dipole potential which is much stronger than the anti-confining effect due to the finite size of the lattice beams. In a blue-detuned lattice, atoms sit at the intensity minima where the transverse dipole potential vanishes and therefore the effect of the anti-confinement is noticeable. However, if the intensities of the two lattice beams are not perfectly equal, there will be no perfect destructive interference at the nodes of the standing wave potential, leading to an additional anti-confinement. The anti-confinement induced by this dipole potential is, however, even for large intensity mismatches of 10% between the beams, more than an order of magnitude smaller than the anti-confinement induced by the spatially dependent lattice depth.

By modeling the trapping potential with the measured waists of the dipole and lattice beams, we can estimate the trapping frequency along the y-direction in the presence of the lattice to be $\omega_y = 2\pi \times 26.5\,\mathrm{Hz}$. The trapping frequency along the x-direction is inferred by taking *in-situ* images of the BEC inside the lattice. According to Eq. 2.24, the fraction between R^y_{TF} and R^x_{TF} is given by

$$\frac{R^y_{TF}}{R^x_{TF}} = \frac{\omega_x}{\omega_y} \tag{3.30}$$

which should be constant over the whole range of scattering lengths measured. Figure 3.13 (b) shows that the fraction is indeed constant and one can extract a ratio between the trapping frequencies of $\omega_x \sim 0.737\omega_y$. Hence, we estimate the trapping frequency along the x-direction in the presence of the lattice to be $\omega_x = 2\pi \times 19.5\,\mathrm{Hz}$.

3.4.2 Atom number calibration

In section 2.1.3 we have seen that the density distribution of a BEC inside a harmonic trap can be described by the Thomas-Fermi density distribution. Solving Eq. 2.24 for the atom number N one obtains

$$N = \frac{(R^i_{TF})^5 M^2 \omega_i^5}{15a\hbar^2\bar{\omega}^3}, \quad \text{with } i = x, y, z. \tag{3.31}$$

Since the harmonic trapping frequencies can be precisely determined as shown in section 3.4.1, the atom number can be obtained by carefully measuring the Thomas-Fermi radius for various scattering lengths. To this end, we image the BEC in the

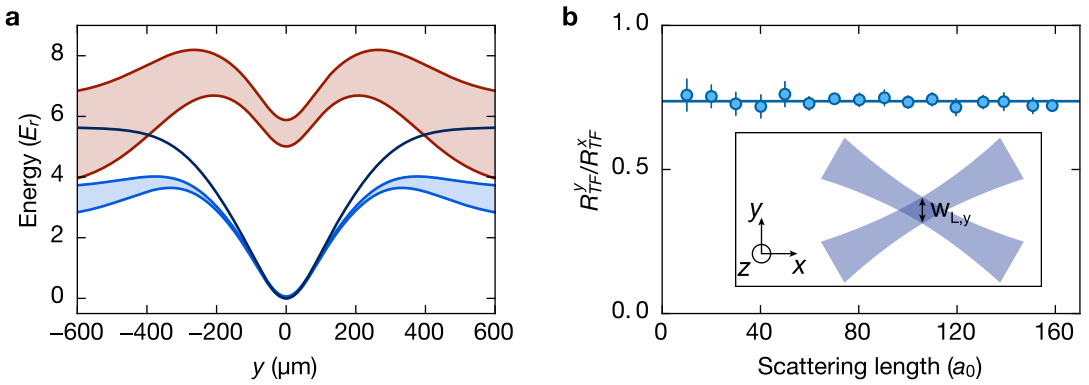

Figure 3.13: **Spatial dependence of the band structure. (a)** Spatial dependence of the bandwidth of the lowest two bands along the y-direction perpendicular to the lattice. The energies of the lowest band are illustrated in light blue and the energies of the first excited band in red. Due to the Gaussian shape of the lattice beams, the bandwidth of the individual bands increases further away from the center of the trap. The dark blue line illustrates the pure dipole potential. One can see that the presence of the lattice leads to a reduced overall confinement. **(b)** Fraction of the Thomas-Fermi radii along the x- and y-axis. The horizontal line indicates the mean value of the measured fractions R^y_{TF}/R^x_{TF}. Error bars indicate the standard error of the mean from four measurements per data point, respectively. The inset shows the two lattice beams in light blue. The arrow indicates the effective waist of the lattice beams along the y-axis.

dipole trap *in-situ*. To reliably determine the Thomas-Fermi radius one has to keep in mind that the imaging pulse increases the size of the BEC due to photon scattering events. For atoms initially at rest, the velocity in the horizontal x-y-plane, after n photon scattering events, is given by [132]

$$v_{xy} = v_{\mathrm{rec}}\sqrt{n}. \tag{3.32}$$

Here $v_{\mathrm{rec}} = h/(M\lambda)$ is the recoil velocity which atoms acquire after a scattering event with a photon of wavelength λ. From Eq. 3.32 it becomes clear that the total number of scattered photons has to be small and, at the same time, the imaging duration needs to be short to be able to reliably determine the size of the condensate. This poses a technical challenge in our setup. To properly resolve the BEC *in-situ*, the magnification of the imaging system is, with approximately 16, quite large. Therefore, the atoms have to be imaged with high intensities such that each pixel of the CCD camera collects enough photons that a workable image can be retrieved from the camera. This results in an imaging intensity I that is far above the saturation intensity (here $I \sim 600 I_{\mathrm{sat}}$) and hence the column density $n_{\mathrm{col}}(x, y)$ is given by Eq. 3.15. Note that by properly determining the parameter α^*, the atom number could also be directly determined from the fits of the BEC. Since we are only interested in the Thomas-Fermi radius and not the absolute height of the column density the lack of knowledge of the absolute value of α^* poses no problem for us. Figure 3.14 shows the measured Gaussian standard deviation of the condensate for different imaging durations. The solid line shows the theoretically expected spread of the condensate width in the horizontal plane according to

$$s_{xy} = s_0 + \int v_{xy}(t)\mathrm{d}t = s_0 + v_{\mathrm{rec}}\sqrt{\Gamma/2 \cdot t}, \tag{3.33}$$

where s_0 is the initial Gaussian standard deviation of the BEC. We get very good agreement between the measured and expected widths for imaging durations smaller than $10\,\mu$s. The discrepancy for larger imaging durations can be explained by the velocity of the atoms getting closer to the Doppler off-resonant velocity $v_d = 2\pi\Gamma/\lambda$, leading to a reduced photon scattering rate.

For the atom number calibration we choose an imaging duration of $3\,\mu$s which turned out to be a good compromise between the signal to noise ratio of the image and the BEC not increasing notably in size, yet. Figure 3.15 (a) shows the measured Thomas-Fermi radii along the x- and y-direction for different scattering lengths. The solid lines show a fit to the data according to Eq. 3.31. The cloud exhibits a slight asymmetry due to different trapping frequencies along the x- and y-direction. The fits yield atom numbers of $4.2(1)\times10^5$ and $3.8(2)\times10^5$, respectively. Figure 3.15 (c,d) show two crosscuts of the BEC at scattering lengths of $40\,a_0$ and $140\,a_0$ together with a Thomas-Fermi density distribution fit to the data. One can see that the Thomas-Fermi approximation describes the density profile of the condensate very

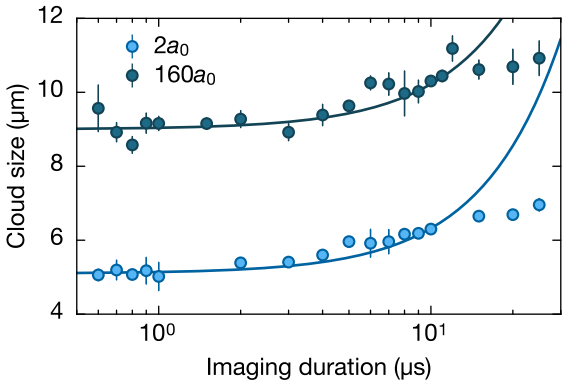

Figure 3.14: ***In-situ* size versus imaging duration.** The Gaussian standard deviations of the BEC for $2\,a_0$ (light blue) and $160\,a_0$ (dark blue) are plotted for different imaging durations. Error bars depict the standard deviation of the mean from at least three individual measurements per data point. For increasing imaging durations the condensate starts to expand in the horizontal plane due to the absorption of photons. The solid lines show the expected size of the condensate. For longer imaging pulse durations the increasing discrepancy between theory and the measured values can be explained by a reduced photon scattering rate because the imaging light becomes off-resonant.

well.

To double check this atom number calibration, we additionally determine the atom number from a Gaussian variational ansatz. This ansatz is reasonable because the dipole trap can be approximated by a harmonic oscillator potential, whose ground state wavefunction is a Gaussian. Since the interaction energy of the BEC is still weak in the dipole trap, the density profile of the condensate is reasonably well described by a Gaussian density profile. This is illustrated in Fig. 3.15 (c,d) where the crosscuts of the BEC are shown together with a Gaussian fit.

As a starting point of the variational ansatz let us assume that the wave function of the condensate is given by

$$\Psi(x,y,z) = \frac{\sqrt{N_0}}{\sqrt{\pi^{3/2}\sigma_x\sigma_y\sigma_z}} e^{-\frac{x^2}{2\sigma_x}-\frac{y^2}{2\sigma_y}-\frac{z^2}{2\sigma_z}}. \tag{3.34}$$

Hence, the number of condensed atoms N_0 is given by

$$N_0 = \int \mathrm{d}x\,\mathrm{d}y\,\mathrm{d}z\,|\Psi(x,y,z)|^2\,. \tag{3.35}$$

The widths $\sigma_{x,y,z}$ of the condensate can be determined by minimizing the total energy $E_{\mathrm{tot}} = E_{\mathrm{kin}} + E_{\mathrm{pot}} + E_{\mathrm{int}}$. The respective expression for the individual energies are given by

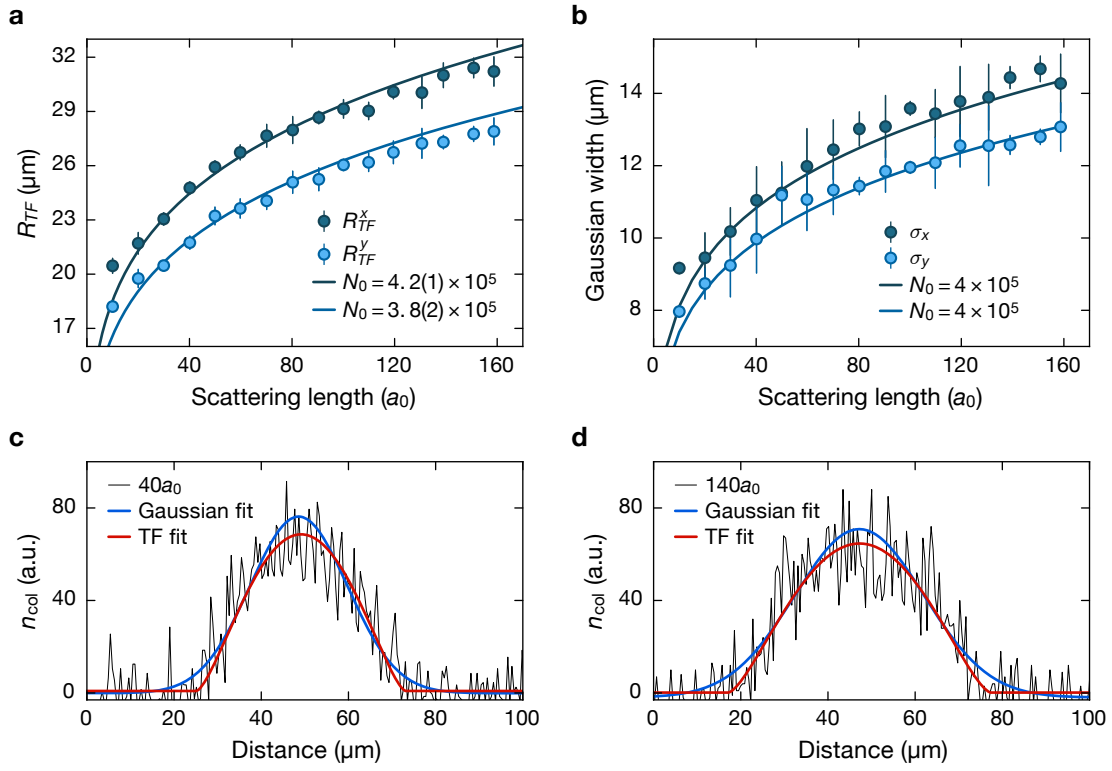

Figure 3.15: **Atom number calibration.** **(a)** *In-situ* Thomas-Fermi radius for different scattering lengths. Since the trapping potential is slightly asymmetric, the condensate is not perfectly round but elliptic. By fitting Eq. 3.31 to the data we can extract the atom number of the BEC. Error bars indicate the standard deviation of the mean for six individual measurements per data point. **(b)** Gaussian fits to the same data as in (a). The solid lines are the numerically estimated Gaussian widths $\sigma_{x,y}$ for a condensate of $N_0 = 4 \times 10^5$ atoms. We get excellent agreement between the data points and the theoretical prediction. **(c)** Crosscut of the condensate for a scattering length of $40\,a_0$. The solid red line is the corresponding Thomas-Fermi fit to the data and the blue line a Gaussian fit. **(d)** Crosscuts and fits for a scattering length of $140\,a_0$.

$$
\begin{aligned}
E_{\text{kin}} &= -\frac{\hbar^2}{2M}\int \mathrm{d}x\,\mathrm{d}y\,\mathrm{d}z\,\Psi(x,y,z)\nabla^2\Psi(x,y,z),\\
E_{\text{pot}} &= \int \mathrm{d}x\,\mathrm{d}y\,\mathrm{d}z\left(\frac{1}{2}M\omega_x^2x^2+\frac{1}{2}M\omega_y^2y^2+\frac{1}{2}M\omega_z^2z^2\right)|\Psi(x,y,z)|^2,\\
E_{\text{int}} &= \frac{4\pi\hbar^2a}{M}\int \mathrm{d}x\,\mathrm{d}y\,\mathrm{d}z\,|\Psi(x,y,z)|^4.
\end{aligned}
\tag{3.36}
$$

Solving these equations individually, one obtains that the total energy of the condensate is given by

$$
\begin{aligned}
E_{\text{tot}} = \frac{\hbar^2N_0\left(\sigma_y^2\sigma_z^2+\sigma_x^2\left(\sigma_y^2+\sigma_z^2\right)\right)}{4M\sigma_x^2\sigma_y^2\sigma_z^2} &+ \frac{1}{4}MN_0\left(\omega_x^2\sigma_x^2+\omega_y^2\sigma_y^2+\omega_z^2\sigma_z^2\right)\\
&+ \frac{2\hbar^2aN_0^2}{\sqrt{2\pi}M\sigma_x\sigma_y\sigma_z}.
\end{aligned}
\tag{3.37}
$$

By minimizing the total energy for the different widths of the cloud

$$
\frac{\partial E_{\text{tot}}}{\partial\sigma_{x,y,z}} = 0, \tag{3.38}
$$

one obtains three expressions for the individual widths of the BEC which are of the form

$$
\frac{4a\hbar^2N^2}{\sqrt{2\pi}\sigma_x\sigma_y\sigma_z} = NM^2\sigma_{x,y,z}^2\omega_{x,y,z}^2 - \frac{\hbar^2N}{\sigma_{x,y,z}^2}. \tag{3.39}
$$

These expressions can be solved numerically. Figure 3.15 (b) shows the measured Gaussian widths of the BEC together with the numerically expected widths for a condensate with $N_0 = 4\times10^5$ atoms. We get excellent agreement between the data and the numerical prediction. This method based on a Gaussian variational ansatz corroborates the atom number we already obtained from the Thomas-Fermi approximation.

3.4.3 Lattice depth calibration

The lattice depth can be determined via multiple different techniques. For a one-dimensional lattice, we mainly use the technique of lattice diffraction since it is straightforward to implement and conduct and only requires a rough knowledge of the expected lattice depth. One can also calibrate the lattice depth by shaking the lattice and measuring the amount of excitations to higher lying bands. This technique was used to confirm the lattice depth obtained via lattice diffraction. In

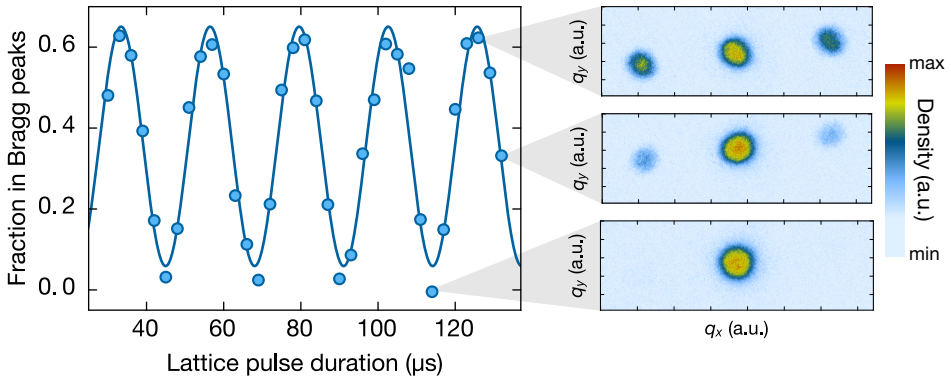

Figure 3.16: **Lattice depth calibration via lattice diffraction.** The fraction of atoms in the first order Bragg peaks is plotted for different lattice hold times. The solid line is a sinusoidal fit to the data. The fitted frequency of 43.4(2) kHz can be compared to a numerical band structure calculation, yielding a lattice depth of 6.93(6) E_r.

the following sections, we will describe each technique in detail and will illuminate their individual (dis-)advantages.

Lattice depth calibration via lattice diffraction

After evaporation in the dipole trap, the atoms condense in a state with zero momentum, which can be approximated by a plane wave state $|\psi(t=0)\rangle = |q_0\rangle$, where $q_0 = 0$. By pulsing on the lattice potential, the free-space momentum state $|q_0\rangle$ is projected onto the Bloch state basis $|\phi_q^{(b)}\rangle$ defined in section 2.2.1. After the projection, the time evolution of the state $|\psi(t)\rangle$ is determined by

$$|\psi(t)\rangle = \sum_{b=1}^{\infty} |\phi_{q_0}^{(b)}\rangle \langle \phi_{q_0}^{(b)} | q_0 \rangle \, e^{-iE_{q_0}^{(b)} t/\hbar}. \tag{3.40}$$

Due to parity conservation only Bloch states with odd band number index can be occupied when pulsing on the lattice. Additionally, for small lattice depths, only Bloch states of the first and third band have a significant overlap with the initial plane wave state $|q_0\rangle$ and contributions from higher lying bands can be neglected [175].

After a certain hold time t_h in the lattice, we suddenly switch it off again, resulting in the wave function being projected back onto the free-space momentum states $|q_0 + 2k_L i\rangle$, where $i = 0, \pm 1$. By varying the hold time in the lattice the contributions of each plane wave component oscillates according to Eq. 3.40 with an oscillation frequency $\nu_B = E_0^{(2)} - E_0^{(0)}/h$, that is given by the energy difference between the lowest Bloch band and second excited Bloch band at $q = 0$. This oscil-

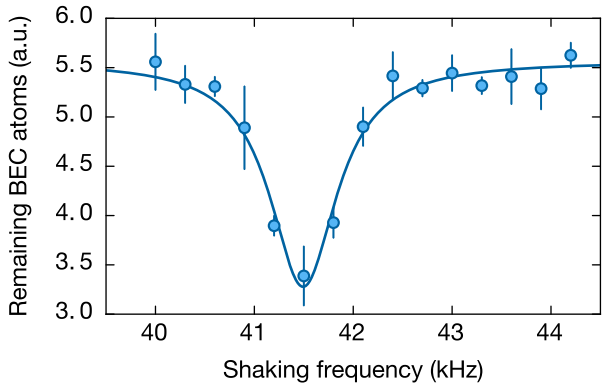

Figure 3.17: **Lattice depth calibration via lattice shaking.** By periodically modulating the lattice, atoms can be transferred to the first excited band when the shaking frequency coincides with the band gap. To keep the band structure unaffected from the modulation, a driving strength of $\alpha = 0.01$ is chosen. The fitted center frequency of $\nu_c = 41.49(4)$ kHz corresponds to a lattice depth of $10.94(3)\, E_r$. The lattice depth was calibrated beforehand with the lattice diffraction technique at $7\, E_R$ and the lattice beam powers were scaled accordingly to yield a lattice depth of $11\, E_r$.

lation can be observed experimentally by imaging the atoms after a certain TOF, see Fig. 3.16. By fitting a sinusoidal function to the data, one can extract the oscillation frequency and can compare the result to a numerical band structure calculation.

In a one-dimensional lattice, we usually calibrate the lattice depth in a $7\, E_r$ deep lattice where the occupation of higher lying bands with $b \geq 4$ is negligible. From this measurement, we obtain a calibration value between the programmed lattice beam powers and the corresponding lattice depth. By simply scaling the beam powers according to this calibration value we can set the lattice depth to any desired value. Most experiments in this thesis were conducted in a one-dimensional lattice with a lattice depth of $11\, E_r$. We have verified independently via frequency modulation spectroscopy, see the following chapter, that the scaling of the lattice beam power works as expected.

This diffraction of atoms by an optical lattice is also referred to as the Kapitza-Dirac effect [176].

Lattice depth calibration via periodic modulation

Another method from which one can infer the lattice depth is by periodically driving the lattice at the resonance frequency to the first excited band. This modulation excites atoms from the lowest band to the first excited band via a single-photon transition. These excitations can be measured by imaging the atoms after a certain TOF using the band mapping technique. However, great care has to be taken to

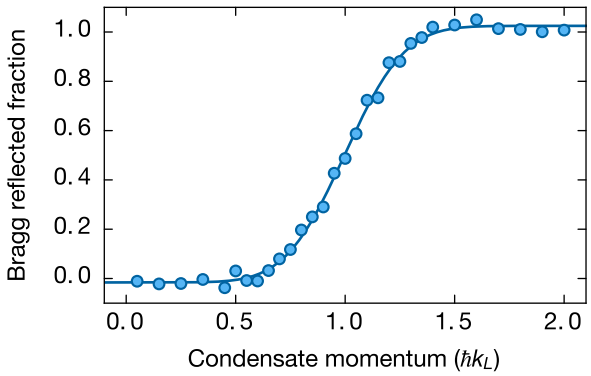

Figure 3.18: **Momentum spread.** The data points show the fraction of condensate atoms that got Bragg reflected at the Brillouin zone edge. To obtain this data, we constantly accelerate the condensate for a variable time. By fitting an error function to the data, we can extract the momentum spread of cloud of $\Delta q = 0.21(1)\hbar k_L$. The measurement was performed at a scattering length of $120\,a_0$.

keep the driving strength α as low as possible. In section 2.3.6 it was shown that the Floquet bands will start to repel each other for increasing driving strengths, leading to a double-well-like structure in the lowest band which would compromise the measurement. Furthermore, avoided crossings to other higher lying bands could occur which would negatively affect the measurement. To this end we set the driving strength to $\alpha = 0.01$, essentially leaving the static band structure unaffected. Figure 3.17 shows a measurement of the lattice depth with this method. Right before this measurement we calibrated the beam powers with the lattice diffraction technique introduced in the previous section and scaled the beam powers such that we obtain an $11\,E_r$ deep lattice. We get excellent agreement between the two measurement techniques. Since the periodic modulation technique is more time-consuming and requires a rough knowledge of the expected lattice depth, it was only used to validate the results obtained from the lattice diffraction technique.

3.4.4 Determination the condensate's momentum spread

As the real space extent of the BEC exceeds its momentum spread even for the longest accessible TOF in our current setup, we cannot directly infer the momentum spread from TOF pictures. Therefore, we estimate the momentum spread differently by performing Bloch oscillations in the lattice. In section 3.3.5, we have described that accelerated atoms get Bragg reflected once they reach the edge of the Brillouin zone. This Bragg reflection results in a sudden change of the real space momentum, which can be clearly observed in band mapped TOF images, see Fig. 3.11. To initiate the Bloch oscillations, we constantly accelerate the one-dimensional lattice

by linearly changing the frequency of one lattice beam. Furthermore, we make sure that we keep the acceleration slow enough, such that no atoms get excited to the second band close to the band edge. For the analysis of the data, we assume that the momentum distribution of the condensate is given by a Gaussian function. With this assumption, the increase of the Bragg reflected fraction of atoms can be described by an error function. Figure 3.18 shows the measured fraction of Bragg reflected atoms at the Brillouin zone edge together with an error function fit. From this fit, we obtain a momentum spread of the condensate of $\Delta q = 0.21(1)\hbar k_L$. For the subsequent part of this thesis, we will assume that the condensate has a momentum spread of $\Delta q = 0.2\,\hbar k_L$ inside the lattice.

Chapter 4

Theoretical and experimental background to determine heating rates

Floquet engineering has become a versatile tool to engineer novel band structures. However, many of the experiments conducted so far have suffered from strong heating [10, 11, 58, 60, 61]. Whenever possible, interactions between particles have been reduced to minimize the heating rates as for example in the experiments conducted in [45, 68]. In this chapter, we will delineate how heating rates in a driven optical lattice system can be estimated. We focus the analysis on a one-dimensional optical lattice with two weakly confined transverse directions. Our findings can also be extended to a two-dimensional lattice like the honeycomb lattice where only one transverse direction is present. In a three-dimensional lattice structure, the heating processes described here should be absent due to the lack of a transverse direction. We start this chapter by establishing a general formalism from which heating rates in optical lattices with transverse directions can be estimated. In the second part, we will describe the experimental sequence and procedures to determine the shaking induced heating rates experimentally.

4.1 Heating and loss mechanisms in Floquet band structures

In section 2.3 it was shown that the energy of a Floquet system is only defined modulo $\hbar\omega$, where ω is the driving frequency of the system. This property of Floquet systems enables the resonant coupling between energetically distant states, leading to a lack of energy conservation. Therefore, it is generally expected that many-body Floquet systems heat up and approach an infinite temperature state in the long-time limit [71, 72, 74–78, 113, 177–185]. It was predicted [186–188] and recently shown in an experiment [189] that heating can be suppressed in many-body localized (MBL) systems for properly chosen driving frequencies. However, it is unclear if

such a strategy based on MBL can be used to stabilize strongly correlated phases such as fractional quantum Hall phases. The main consensus, therefore, is to find experimental setups and/or driving schemes in which heating appears on a long enough time-scale [180, 182, 183, 190–192].

There are two main heating mechanisms present in shaken optical lattice systems: single-particle heating and interaction dependent two-particle heating. Single-particle heating occurs whenever the shaking frequency ω fulfills the resonance condition for an l-"photon" transition

$$l\hbar\omega \approx \varepsilon^{(b)}(q) - \varepsilon^{(0)}(q), \tag{4.1}$$

where l is an integer. Within the Floquet picture, this resonance condition is equivalent to the band energies $\varepsilon_l^{(0)}(q) = \varepsilon^{(0)}(q) + l\hbar\omega$ and $\varepsilon_0^{(b)}(q) = \varepsilon^{(b)}(q)$ becoming (almost) degenerate[1]. These multiphoton transitions to higher lying excited bands conserve the quasimomentum of the particles and can happen even for driving frequencies that are much smaller than the band gap Δ_{b0} to the bth band in the static lattice. Multiphoton resonances have already been studied both theoretically [181] and experimentally [119] and it was shown that they are exponentially suppressed for large numbers of photons l if the driving strength stays below a certain threshold value. As these transitions only occur at specific shaking frequencies, they form sharp resonance features where the lifetime of the system is strongly reduced. Therefore, single-particle multiphoton transitions can easily be avoided by either choosing shaking frequencies that lie between individual multiphoton resonances or by choosing frequencies that are very small compared to the band gap to the first excited band.

The other form of heating in shaken optical lattice systems appears due to interaction dependent (two-particle) scattering processes. This two-particle heating mechanism is not restricted to specific shaking frequencies and is always present for systems with finite interactions. In the following sections we will describe the underlying physics of interaction driven heating in Floquet systems.

4.2 General formalism for heating with interaction effects

In the absence of single-particle heating processes, the dominant heating channels are given by interaction induced *resonant scattering processes* between different Floquet-Bloch states. Such resonant excitation processes have already been studied theoretically [74–78, 179] and will be the basis for our theoretical estimation of heating

[1] Note that the two bands do not have to be perfectly degenerate but can exhibit a small detuning. Multiphoton resonances occur as long as this detuning is smaller or comparable to the coupling matrix element that couples states from these two bands.

rates in a driven one-dimensional optical lattice. First, we will introduce the Hamiltonian that describes our shaken lattice system and present the notation for the following sections. After introducing the system, we will derive a general form of the scattering rate of particles out of the condensate by employing Fermi's golden rule. At first, we will neglect the external potential of the dipole trap and consider a translationally invariant system. The trap is subsequently included by using a local-density approximation based on the Thomas-Fermi approximation.

4.2.1 The Hamiltonian of the system

The Hamiltonian of weakly interacting bosonic particles in a driven optical lattice is given by the sum of the single particle Hamiltonian $\hat{H}_0(t)$ and the time-independent interaction Hamiltonian $\hat{H}_{\text{int}}$

$$\hat{H}(t) = \hat{H}_0(t) + \hat{H}_{\text{int}}. \tag{4.2}$$

The single particle Hamiltonian is defined as

$$\hat{H}_0(t) = \int \mathrm{d}\boldsymbol{r}\, \hat{\Psi}^\dagger(\boldsymbol{r}) h(\boldsymbol{r}, t) \hat{\Psi}(\boldsymbol{r}), \tag{4.3}$$

with $\hat{\Psi}(\boldsymbol{r})$ and $\hat{\Psi}^\dagger(\boldsymbol{r})$ being the bosonic field operators that annihilate or create a boson at position $\boldsymbol{r}$ and

$$h(\boldsymbol{r}, t) = -\frac{\hbar^2}{2M}\nabla^2 + V_L(\boldsymbol{r}) - \boldsymbol{F}(t)\cdot\boldsymbol{r} + V_{\text{dip}}(\boldsymbol{r}). \tag{4.4}$$

Here $V_L(\boldsymbol{r}) = V_0 \cos^2(k_L x)$ is a one-dimensional lattice potential, $V_{\text{dip}}(\boldsymbol{r})$ describes the external trapping potential of the dipole trap and $\boldsymbol{F}(t) = -F_0 \cos(\omega t)\boldsymbol{e}_x = -Md\nu_0\omega\cos(\omega t)\boldsymbol{e}_x$[2] is a time-periodic force that arises due to the shaking of the lattice. The interaction Hamiltonian $\hat{H}_{\text{int}}$ is given by

$$\hat{H}_{\text{int}} = \frac{2\pi\hbar^2 a}{M} \int \mathrm{d}\boldsymbol{r}\, \hat{\Psi}^\dagger(\boldsymbol{r})\hat{\Psi}^\dagger(\boldsymbol{r})\hat{\Psi}(\boldsymbol{r})\hat{\Psi}(\boldsymbol{r}). \tag{4.5}$$

As already mentioned before, we will initially neglect the external trapping potential from the dipole trap and instead consider a translationally invariant system of linear extent L in all three directions together with periodic boundary conditions. Since the lattice potential is only along the x-direction, the single-particle Hamiltonian can be spatially separated. Along the lattice direction, the Hamiltonian reads

$$h_x(t) = -\frac{\hbar^2\partial_x^2}{2M} + V_0\cos^2(\pi x/d) + F_0\cos(\omega t). \tag{4.6}$$

[2] See section 3.3.5 for the derivation of this relation

From section 2.2.1 we know that the eigenstates of the static lattice system are given by Bloch states $|b, k_x\rangle$. Due to the finite extent L of the system, the quasimomentum wave number k_x can only take discrete values $k_x = 2\pi\xi_x/L$, with integers ξ_x such that $-\pi < dk_x \leq \pi$. Note that in the previous sections we always labeled quasimomentum by q. As we will now have to consider also scattered atoms that have different quasimomenta than the BEC and to avoid confusion later on, we will use q solely for the initial quasimomentum of the condensate in the lattice. In terms of the quasimomentum wave number k_x, the Bloch waves can be expressed as

$$\langle x|b, k_x\rangle = u_{k_x}^{(b)}(x)e^{ik_x x}, \tag{4.7}$$

with the lattice periodic part $u_{k_x}^{(b)}(x) = u_{k_x}^{(b)}(x + d)$ and $b = 0, 1, 2, \ldots$ indicating the band index. To describe interactions between particles that happen on a single lattice site, it is convenient to switch to the Wannier basis $|b, j\rangle$. Within this basis the Bloch waves can be expressed as

$$|b, k_x\rangle = \sqrt{\frac{d}{L}} \sum_{j=1}^{L/d} e^{ik_x jd} |b, j\rangle . \tag{4.8}$$

As was already shown in section 2.2.2 the Wannier wave function $\langle x|b, j\rangle = w_b(x-jd)$ is exponentially localized on a single lattice site j and obeys the relation $w_b(-x) = (-1)^b w_b(x)$.

Along the transverse directions $\boldsymbol{r}_\perp = (y, z)$, the eigenstates of the single particle Hamiltonian are given by plane waves

$$\langle \boldsymbol{r}_\perp|\boldsymbol{k}_\perp\rangle = \frac{1}{L} e^{i\boldsymbol{k}_\perp \cdot \boldsymbol{r}_\perp}. \tag{4.9}$$

Due to the finite extent of the system, the momentum wave numbers $\boldsymbol{k}_\perp = (k_y, k_z)$ can again only take discrete values $k_i = 2\pi\xi_i/L$, with ξ_i being an integer. The eigenenergies of the single particle Hamiltonian along the transverse direction are given by

$$E_\perp(\boldsymbol{k}_\perp) = \frac{\hbar^2 \boldsymbol{k}_\perp^2}{2M}. \tag{4.10}$$

The scattering processes, described further below, predominantly involve the lowest two bands of the lattice. Since all measurements were performed in an $11\, E_r$ deep lattice, the lowest two bands are well approximated by a tight binding model. The dispersion relation of the static lattice can thus be approximated by

$$E_b(k_x) \simeq \epsilon_b - 2J_b \cos(dk_x), \tag{4.11}$$

where J_b denotes the tunneling matrix element of the b^{th} band and ϵ_b denotes the band center energy. For bands with odd (even) band index b, one finds that the

tunneling matrix element J_b is positive (negative). Due to the large lattice depth, we can neglect the interaction between particles at different lattice sites. Therefore, we can write down the bosonic annihilation operator $\hat{\Psi}(\boldsymbol{r})$ within the Wannier basis as

$$\hat{\Psi}(\boldsymbol{r}) = \sum_{b,\boldsymbol{k}} \phi_{\boldsymbol{k}}^{(b)}(\boldsymbol{r}) \hat{a}_{b,\boldsymbol{k}}, \tag{4.12}$$

where $\hat{a}_{b,\boldsymbol{k}}$ is the annihilation operator for the single-particle state $|b, \boldsymbol{k}\rangle$ and

$$\phi_{\boldsymbol{k}}^{(b)}(\boldsymbol{r}) = \langle \boldsymbol{r}|b, \boldsymbol{k}\rangle = \sqrt{\frac{d}{L^3}} e^{i\boldsymbol{k}_\perp \cdot \boldsymbol{r}_\perp} \sum_{j=1}^{L/d} e^{ik_x jd} w_b(x - jd). \tag{4.13}$$

Thus, by taking into account only on-site interactions, the interaction Hamiltonian is expressed as

$$\hat{H}_{\text{int}} = \frac{g}{2L^3} {\sum_{\{b,\boldsymbol{k}\}}}' \zeta_{\{b\}} \hat{a}^\dagger_{b_4,\boldsymbol{k}_4} \hat{a}^\dagger_{b_3,\boldsymbol{k}_3} \hat{a}_{b_2,\boldsymbol{k}_2} \hat{a}_{b_1,\boldsymbol{k}_1}, \tag{4.14}$$

where the prime at the sum indicates that both momentum and quasimomentum have to be conserved and

$$\zeta_{\{b\}} \equiv \zeta_{b_4 b_3 b_2 b_1} = d \int \mathrm{d}x \, w_{b_4}(x) w_{b_3}(x) w_{b_2}(x) w_{b_1}(x). \tag{4.15}$$

Due to on-site parity conservation, $\zeta_{b_4 b_3 b_2 b_1}$ vanishes whenever $b_1 + b_2 - b_3 - b_4$ is odd. To avoid unnecessary lengthy notations, we abbreviate $\zeta_{0000} \equiv \zeta$.

4.2.2 Definition of heating within the Floquet picture

Recall from chapter 2.3 that the time evolution generated by the time-periodic Hamiltonian $\hat{H}(t) = \hat{H}(t+T)$ over one period T can be described by an effective Hamiltonian $\hat{H}_{\text{eff}}$ which is independent of time. This property of periodically driven systems is the cornerstone of Floquet engineering. Thus, by designing special driving schemes one can create effective Hamiltonians with properties that might not be implementable in static systems. However, for a driven many-body system, it is generally not possible to exactly calculate the effective Hamiltonian. In order to approximate the effective Hamiltonian, one can perform a suitable gauge transformation with a unitary operator $\hat{U}(t) = \hat{U}(t+T)$ on the Hamiltonian $\hat{H}(t)$ resulting in

$$\hat{H}'(t) = \hat{U}^\dagger(t) \hat{H}(t) \hat{U}(t) - i\hbar \hat{U}^\dagger(t) \dot{\hat{U}}(t) = \sum_m \hat{H}'^{(m)} e^{im\omega t}. \tag{4.16}$$

The gauge transformation is chosen in such a way that the Fourier components $\hat{H}'^{(m)}$ with $m \neq 0$ can be neglected on experimentally relevant timescales

$$\hat{H}_{\text{eff}} \approx \hat{H}_{\text{app}} \equiv \hat{H}'^{(0)}. \tag{4.17}$$

Recall from section 2.3.2 that the matrix elements of the quasienergy operator are given by

$$\langle\langle \alpha', m' | \bar{Q} | \alpha, m \rangle\rangle = \langle \alpha' | \hat{H}'^{(m'-m)} | \alpha \rangle + \delta_{m'm} \delta_{\alpha'\alpha} m\hbar\omega. \tag{4.18}$$

In the Floquet space picture, the approximation of neglecting Fourier components with $m \neq 0$ implies that we only keep the diagonal terms of the quasienergy operator $\bar{Q}$.

Two effects arise if we take into account the off-diagonal terms with $m \neq 0$. The first effect leads to corrections of the approximate effective Hamiltonian $\hat{H}_{\text{app}}$. These corrections result from a *perturbative* admixture of states within the subspaces with $m \neq 0$ to states within the subspace $m = 0$. Here the states in the different m-subspaces are quasienergetically distant to each other. These perturbative admixtures lead to a correction $\hat{H}_{\text{corr}}$ to the approximate effective Hamiltonian and can be calculated, for example, within a high-frequency expansion [63, 113].

The second effect that arises if we take into account the off-diagonal terms of the effective Hamiltonian is *heating*. Here states from different subspaces m couple *resonantly* to each other. These resonant couplings lead to a hybridization of states from the m subspace with states from subspaces $m' = m - l \neq 0$, where $l > 0$ corresponds to the number of absorbed photons. Since such resonant coupling processes correspond to dissipative processes where the system changes its energy by $l\hbar\omega$, they cannot be taken into account by adding a correction to the effective Hamiltonian and must be considered as heating.

4.2.3 Coupling matrix elements via perturbation theory

To be able to estimate the scattering rate of particles out of the condensate, we have to determine the matrix elements that resonantly couple states from different m-subspaces. These coupling matrix elements can be determined via perturbation theory in Floquet space. For this purpose let us define $|n\rangle$ as an eigenstate of $\hat{H}'^{(0)}$ with energy ε_n

$$\hat{H}'^{(0)} |n\rangle = \varepsilon_n |n\rangle , \tag{4.19}$$

and assume that the system is initially prepared in the ground state $|0\rangle$ of $\hat{H}'^{(0)}$. In Floquet space, the corresponding basis states of $|n\rangle$ are given by $|n, m\rangle\rangle$. When we neglect the off-diagonal terms of the quasienergy operator, the states $|n, m\rangle\rangle$ become eigenstates of the quasienergy operator with corresponding quasienergies

$\varepsilon_{n,m} = \varepsilon_n + m\hbar\omega$. According to the definition in the previous section, heating requires that there exists an excited state with energy ε_n modulo $\hbar\omega$ that is almost degenerate to the ground state with energy ε_0

$$\varepsilon_n = \varepsilon_0 + l\hbar\omega + \delta. \tag{4.20}$$

It is necessary that the detuning $|\delta|$ is small compared to the coupling matrix element $C^{(l)}_{n,0}$ that couples the state $|0,m\rangle\rangle$ and the excited state $|n,m-l\rangle\rangle$ via a l-photon process. For simplicity let us assume that the system is initially prepared in the ground state $|0,0\rangle\rangle$. The matrix element for a direct coupling process is then given by

$$C^{(l)1st}_{n,0} = \langle\langle n,m|\bar{Q}|0,0\rangle\rangle = \langle n|\hat{H}'^{(m)}|0\rangle\,, \tag{4.21}$$

where $m=-l$. However, it is also possible to couple the two states $|0,0\rangle\rangle$ and $|n,m\rangle\rangle$ indirectly via virtual intermediate states. For a single intermediate state $|n_1,m_1\rangle\rangle$ the coupling matrix element can be obtained via degenerate perturbation theory in 2nd-order and reads

$$C^{(l)2\mathrm{nd}}_{n,0} = {\sum_{n_1,m_1}}' \frac{\langle n|\hat{H}'^{(m-m_1)}|n_1\rangle\,\langle n_1|\hat{H}'^{(m_1)}|0\rangle}{\varepsilon_0 - (\varepsilon_{n_1} + m_1\hbar\omega)}. \tag{4.22}$$

The prime at the sum indicates that we only sum over intermediate states that are quasienergetically well separated from the initial state $|0,0\rangle\rangle$ and the final state $|n,m\rangle\rangle$. Furthermore, we have assumed that the detuning δ is much smaller than the energy in the denominator and can thus be neglected. In general, a pth-order process that happens via $p-1$ intermediate states $|n_i,m_i\rangle\rangle$ is given by a matrix element of order

$$C^{(l)p\mathrm{th}}_{n,0} \sim {\sum_{\{n_i,m_i\}}}' \frac{\langle n|\hat{H}'^{(m-m_{p-1})}|n_{p-1}\rangle\cdots\langle n_1|\hat{H}'^{(m_1)}|0\rangle}{(\varepsilon_0-\varepsilon_{n_{p-1}}-m_{p-1}\hbar\omega)\cdots(\varepsilon_0-\varepsilon_{n_1}-m_1\hbar\omega)}. \tag{4.23}$$

4.2.4 Determination of scattering rates

After having determined the coupling matrix elements between different Floquet states, we can calculate the scattering rate of atoms out of the condensate. To this end, let us assume that we start with an almost pure condensate of N_0 atoms. The condensate is initially prepared in the minimum of the lowest Floquet-Bloch band[3] and is described by the single-particle Floquet-Bloch state $|b=0,\boldsymbol{q}\rangle$. Note that

[3]We remark again that technically speaking there is no lowest Floquet-Bloch band due to the periodicity of the quasienergies. However, in order to simplify notation we will refer to the lowest Floquet-Bloch band as the one that is adiabatically connected to the lowest band in the static lattice system.

depending on the driving strength α and driving frequency ω, the minimum of the lowest Floquet-Bloch band will be at $\boldsymbol{q} \neq 0$ and hence atoms will condense into a state of finite quasimomentum. This state will be the initial state from which we will compute the coupling matrix elements. A general l-photon scattering process will transfer two atoms from the condensate into their new Floquet-Bloch states $|b, \boldsymbol{q}+\boldsymbol{k}\rangle$ and $|b', \boldsymbol{q}-\boldsymbol{k}\rangle$, respectively, where $\boldsymbol{k} = (k_x, \boldsymbol{k}_\perp)$. This process is described by the coupling matrix element $C^{(l)}_{b'b}(\boldsymbol{k}, \boldsymbol{q})$. Due to the free space along the perpendicular directions and since the interactions between particles are given by contact interaction, the matrix elements $C^{(l)}_{b'b}(\boldsymbol{k}, \boldsymbol{q})$ will be independent of the transverse momenta $\boldsymbol{k}_\perp$. From section 4.2.1 we know that the interactions are proportional to $N_0 g/L^3$. With this knowledge, we can express the coupling matrix element as

$$C^{(l)}_{b'b}(\boldsymbol{k}, \boldsymbol{q}) \equiv C^{(l)}_{b'b}(k_x, q) \equiv \frac{N_0 g}{L^3} c^{(l)}_{b'b}(k_x, q), \tag{4.24}$$

where $c^{(l)}_{b'b}(k_x, q)$ is a dimensionless factor that is independent of the system size. As the total energy of the system must be conserved during a l-photon scattering event, only states that obey the energy conservation condition

$$\varepsilon_b(q + k_x) + \varepsilon_{b'}(q - k_x) + 2E_\perp(\boldsymbol{k}_\perp) - 2\varepsilon_0(q) - l\hbar\omega = 0 \tag{4.25}$$

are accessible. Due to the continuum of transverse modes $\boldsymbol{k}_\perp$, the transverse energy $E_\perp(\boldsymbol{k}_\perp)$ can take any arbitrary non-negative value leading to the inequality

$$\varepsilon_b(q + k_x) + \varepsilon_{b'}(q - k_x) - 2\varepsilon_0(q) - l\hbar\omega < 0. \tag{4.26}$$

For convenience we define that $c^{(l)}_{b'b}(k_x, q) = 0$ whenever this resonance condition is not fulfilled.

With all these ingredients and by employing Fermi's golden rule, we can define the scattering rate Γ_l of particles out of the condensate resulting from an l-photon process as

$$\Gamma_l = 2\frac{1}{2}\sum_{k_x}\sum_{b,b'} \frac{2\pi}{\hbar} \left| C^{(l)}_{b'b}(k_x, q) \right|^2 \rho_\perp. \tag{4.27}$$

The prefactor two accounts for the fact that particles are always scattered pairwise out of the condensate whereas the prefactor $1/2$ takes into account that the interchange $(b, k_x) \leftrightarrow (b', -k_x)$ does not lead to a new target state. Furthermore, $\rho_\perp = ML^2/(2\pi\hbar^2)$ describes the 2D density of states for the transverse momenta [193]. By replacing the sum in Eq. 4.27 by an integral

$$\sum_{k_x} \to \frac{L}{2\pi} \int_{-\pi/d}^{\pi/d} \mathrm{d}k_x, \tag{4.28}$$

we obtain the general form of the l-photon scattering rate

$$\Gamma_l = 32 N_0 n_{2\mathrm{D}} a^2 \frac{E_r}{\hbar} \gamma_l. \tag{4.29}$$

Here $n_{2\mathrm{D}} = dN_0/L^3$ denotes the density of atoms in the 2D planes of the lattice. Furthermore, we have introduced the dimensionless scattering parameter

$$\gamma_l = \sum_{b,b'} \frac{d}{2\pi} \int_{-\pi/d}^{\pi/d} \mathrm{d}k_x \left| c_{b'b}^{(l)}(k_x) \right|^2. \tag{4.30}$$

So far we have neglected the external trapping potential created by the dipole trap. In a first step, we will replace the simplified homogeneous density of atoms $n_{2\mathrm{D}}$ by a Thomas-Fermi approximation. Compared to the Thomas-Fermi model introduced in section 2.1.3, we now have to take into account that the atoms are additionally trapped in a lattice. Due to the large lattice depth, we assume that the wave functions of the individual atoms are well described by Wannier functions in the lowest band. Within this approximation, we can assume that the order parameter of the condensate on the jth lattice site is given by $\psi_j = \sqrt{n_j(y,z)}$, where $n_j(y,z)$ denotes the two-dimensional condensate density in the jth minimum of the lattice. As before, we assume that interactions happen only on-site. With these considerations, the potential energy of the system is given by

$$E = \sum_j \int \mathrm{d}y \mathrm{d}z \left(\frac{\tilde{g}}{2d} n_j(y,z) + V_{\mathrm{dip}}(x,y,z) - \mu \right) n_j(y,z). \tag{4.31}$$

Here μ is the chemical potential and $\tilde{g} = g\zeta$ denotes the effective interaction of the atoms within the lattice and $V_{\mathrm{dip}} = 1/2M(\omega_x^2 x^2 + \omega_y^2 y^2 + \omega_z^2 z^2)$ is the harmonic approximation of the dipole potential, where the harmonic trapping frequencies $\omega_{x,y,z}$ are the ones we determined in the presence of the lattice potential. Since the size of the BEC is much larger than the lattice spacing, with the BEC occupying approximately 100 to 150 lattice sites, it is convenient to approximate the site index j by the continuous position $x = dj$. Within this approximation, we can replace the sum

$$\sum_j \frac{1}{d} \to \int \mathrm{d}x \tag{4.32}$$

and define the three-dimensional density of the condensate as $n(\boldsymbol{r}) = n_{x/d}(y,z)/d$. With these approximations we can determine the density distribution of the condensate according to the Thomas-Fermi approximation

$$n(\boldsymbol{r}) = \begin{cases} \frac{\mu - V_{\mathrm{dip}}(\boldsymbol{r})}{\tilde{g}} & \text{where } V_{\mathrm{dip}}(\boldsymbol{r}) < \mu, \\ 0 & \text{elsewhere.} \end{cases} \tag{4.33}$$

By integrating over the density profile (compare to section 2.1.3) we determine the chemical potential to be

$$\mu = \left(\frac{15\pi}{8} \zeta \frac{a}{d} \left(\frac{\hbar\bar{\omega}}{E_r} \right)^3 N_0 \right)^{2/5} E_r, \tag{4.34}$$

where $\bar{\omega}$ denotes the geometric mean of the trapping frequencies. According to Eq. 4.29, the scattering rate per volume Γ_l/L^3 scales like

$$\frac{\Gamma_l}{L^3} = 32\gamma_l d a^2 \frac{E_r}{\hbar} \left(\frac{N_0}{L^3} \right)^2. \tag{4.35}$$

Thus, within a local-density approximation and by replacing the homogeneous density N_0/L^3 by the Thomas-Fermi density distribution defined in Eq. 4.33, the total l-photon scattering rate is given by

$$\begin{aligned} \Gamma_l^{\mathrm{LDA}} &= 32\gamma_l d a^2 \frac{E_r}{\hbar} \int \mathrm{d}\boldsymbol{r} n^2(\boldsymbol{r}) \\ &= \frac{128}{105} \zeta^{-3/5} \left(\frac{15\pi}{8} \frac{a}{d} N_0 \right)^{7/5} \left(\frac{\hbar\bar{\omega}}{E_r} \right)^{6/5} \frac{E_r}{\hbar} \gamma_l. \end{aligned} \tag{4.36}$$

This equation is the basic equation from which we will infer the heating rates later on. Its general form is independent of the driving regime and the only variable that depends on the driving frequency and driving strength is the dimensionless scattering parameter γ_l, which we will determine later on when we take a closer look at the scattering processes in two different shaking regimes.

4.3 General experimental considerations

In this section, we will describe the experimental procedure from which we infer the heating rates of our system. We will show that the Thomas-Fermi approximation is indeed a valid approximation during most parts of the loss process induced by the shaking of the lattice. This property is a necessary ingredient to be able to compare the measured heating rates with the theoretically estimated scattering rates. Furthermore, we will introduce a fit function that directly allows us to extract the loss rates that solely originate from the shaken lattice. In the last subsection, we will determine the positions of the multiphoton single-particle resonances.

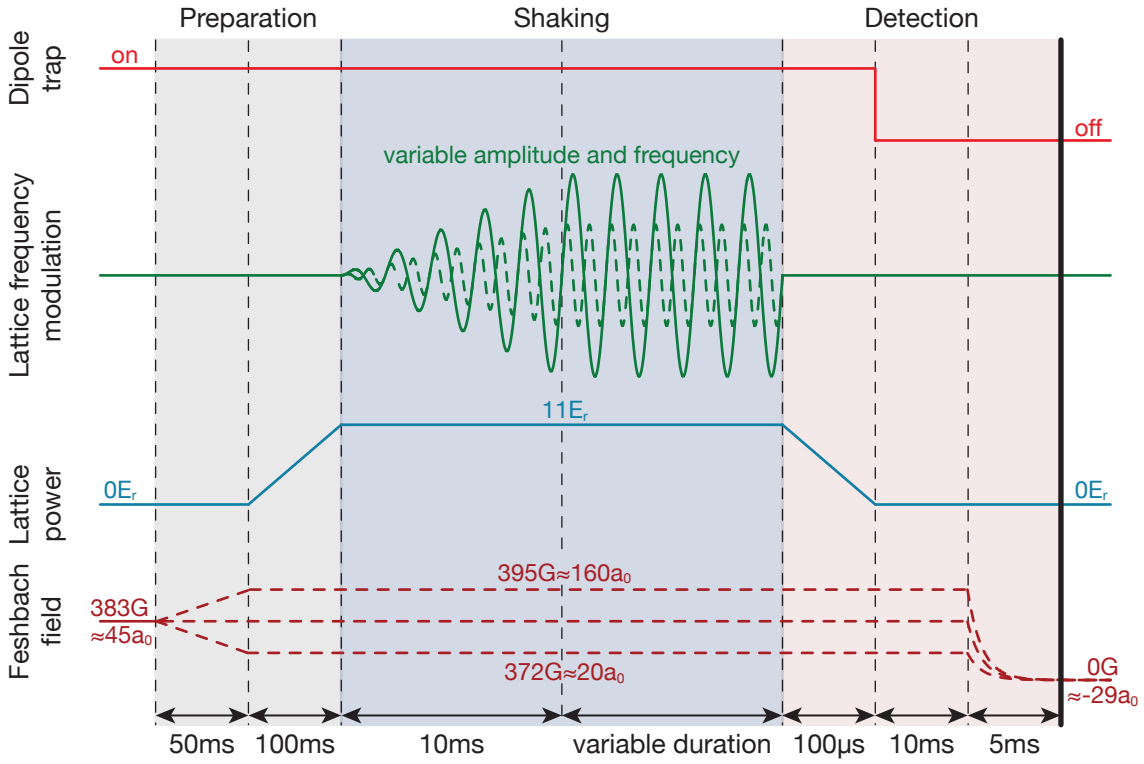

Figure 4.1: **Sketch of the experimental sequence.** The schematic shows the Feshbach field, lattice depth, dipole trap and the frequency modulation of one of the lattice beams over the course of the experimental sequence. The thick black line indicates the time at which the condensate is being imaged. For further details see text.

4.3.1 Experimental sequence

An overview of the general experimental sequence is given in Fig. 4.1. After having prepared a BEC of approximately 4×10^5 ^{39}K atoms in the dipole trap, we ramp the interaction of the atoms in 50 ms to its desired value. We have verified that this ramp time is long enough to be adiabatic and not induce any breathing modes within the BEC or even lead to atom number losses.

After having prepared the BEC at the desired interaction strength we ramp up the power of the lattice beams in 100 ms such that we reach a final lattice depth of 11 E_r. Directly after the loading into the lattice is completed, we start shaking the lattice by modulating the frequency of one of the two lattice beams via an AOM. In order to not create any initial excitations of the condensate, we always linearly ramp up the shaking amplitude in 10 ms to its final value. While longer ramp up durations might be favorable for extreme shaking parameters, we tried to keep the ramp up duration as short as possible to be able to perform reliable lifetime measurements

even when the BEC is short lived. We have checked that this ramp up duration is long enough to not create any strong, non-adiabatic excitations to higher bands even for the strongest forcing parameters used below.

After the ramp up of the modulation, we continue to shake the atoms for a variable duration. To determine the induced heating and losses of condensed atoms, we suddenly stop the modulation after an integer number of driving cycles. Immediately afterwards, we perform bandmapping in the static system and image the atoms after 15 ms TOF. This TOF is long enough to dilute any created thermal background such that we can reliably determine the remaining number of atoms in the condensate. For the first 10 ms of TOF we keep the Feshbach field at the value used during the shaking procedure, such that the BEC can expand at a fixed scattering length. This procedure is necessary as the background scattering length of ^{39}K is negative and a direct switch off of the Feshbach field would lead to distorted images. After 10 ms of TOF, the cloud has already expanded so much that the switch off of the magnetic field has no impact on the atoms anymore.

To count the remaining number of condensed atoms, we sum the pixel values of the image within a region of interest (ROI). This ROI is kept constant for all images in order to avoid counting possible artifacts that might arise from different ROIs. After 15 ms TOF any created thermal background is already strongly diluted and can be assumed to be almost homogeneous in the vicinity of the condensate. To avoid counting thermal atoms, we choose a second ROI, the so-called background ROI, that lies close to the main ROI. We then subtract the mean pixel value of this background ROI from every pixel value within the main ROI. The remaining number of condensed atoms is then extracted from the sum of pixel values by multiplying it by a scaling factor. This scaling factor is obtained by comparing the sum of pixel values of a condensate directly released from the dipole trap with the known total atom number obtained via the atom number calibration described in section 3.4.2.

4.3.2 Validity of the Thomas-Fermi ansatz

In section 4.2.4 we deduced a general form of interaction dependent scattering rates that occur in shaken optical lattices. There we assumed that the condensate is described by a Thomas-Fermi density distribution during (most parts of) the shaking process. This assumption is equivalent to the assumption that the condensate stays in a global thermal equilibrium with its environment throughout the heating process. According to the Thomas-Fermi density distribution this means that the ratio $\mathcal{R}^i = R^i_{TF}/N_0(t)^{1/5}$, with $i = x, y, z$, stays constant. We verify this behavior by measuring the *in-situ* Thomas-Fermi radius for various shaking durations. Directly afterwards, we repeat the same measurement but this time determine the remaining number of condensed atoms from TOF images. Figure 4.2 shows two exemplary measurements of $\mathcal{R}^i$ in two different shaking regimes. Note that we cannot measure the *in-situ* size of the condensate along the vertical direction. Thus, we have to assume that the

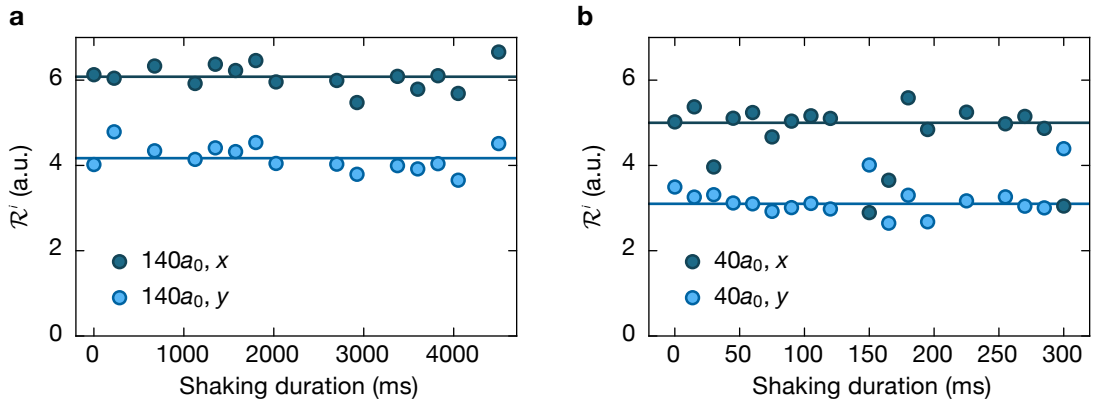

Figure 4.2: **Validity of Thomas-Fermi approximation. (a)** The ratio $\mathcal{R}^i = R^i_{TF}/N_0(t)^{1/5}$ is plotted versus shaking duration. Due to the asymmetry of the trapping potential, the Thomas-Fermi radii and therefore also $\mathcal{R}^i$ have slightly different values along the x-direction (dark blue points) and the y-direction (light blue points). The shaking frequency is $\omega = 2\pi \times 3.5\,\mathrm{kHz}$ with a driving strength of $\alpha = 0.44$ and a scattering length of $a = 140\,a_0$. The solid lines indicate the mean value of $\mathcal{R}^i$ over all shaking durations. **(b)** $\mathcal{R}^i$ for $\omega = 2\pi \times 53\,\mathrm{kHz}$, $\alpha = 1.3$ and $a = 40\,a_0$. Here, due to the large scattering of some data points, the solid lines are a guide to the eye. For both shaking parameters, the cloud is well described by a Thomas-Fermi density approximation, indicating thermal equilibrium during most parts of the loss process.

behavior in this direction is equivalent to the behavior in the horizontal directions. In Fig. 4.2 (a) we chose a shaking frequency of $\omega = 2\pi \times 3.5\,\mathrm{kHz}$ with a weak driving strength of $\alpha = 0.44$ and a scattering length of $a = 140\,a_0$. With these shaking parameters, the lifetime of the condensate in the shaken lattice is almost as long as the lifetime in the static lattice. Hence, we expect the system to stay in a global thermal equilibrium which is confirmed by the measurement as $\mathcal{R}^i$ stays constant during the shaking process. Figure 4.2 (b) shows a more extreme example. Here the shaking frequency is set to $\omega = 2\pi \times 53\,\mathrm{kHz}$[4] with a strong driving of $\alpha = 1.3$. For these shaking parameters, the lifetime of the condensate is already heavily reduced compared to the static case. Furthermore, we choose a scattering length of $a = 40\,a_0$ and thus thermalization processes due to collisions between particles take more time. Even for these more extreme shaking parameters, the system stays in global thermal equilibrium.

These measurements confirm that the system stays in a thermal equilibrium during most part of the shaking process and that the Thomas-Fermi density distribution is a valid approximation during the shaking process.

4.3.3 Extracting the loss rate

There are two different loss mechanisms occurring in our system. On the one hand, we have a background heating rate that defines the natural lifetime of the condensate. This heating comes from collisions with the hot background gas and also from three-particle recombination processes [194] which are enhanced in the vicinity of a Feshbach resonance [195]. We can observe this effect by a slightly reduced $1/e$ lifetime of the condensate from about 4.2 s at a scattering length of $20\,a_0$ to a lifetime of around 3.2 s at a scattering length of $160\,a_0$. The atom number losses due to these background heating channels are well described by the differential equation $\dot{N}_0 = -\kappa_{bg} N_0$.

The other heating mechanism stems from the shaking of the lattice. From the theoretically expected scattering rate defined in Eq. 4.36 we expect a particle-number independent loss rate κ. The loss of condensed particles can accordingly be described via the differential equation $\dot{N}_0 = -\kappa N_0^{7/5}$. As a good approximation, we can assume that these two loss mechanisms are independent of each other. Hence, the total loss rate of condensed particles is described by the differential equation $\dot{N}_0 = -\kappa_{bg} N_0 - \kappa N_0^{7/5}$, whose solution is given by

$$N_0(t) = N_0(0) \frac{e^{-t/\tau}}{\left(1 + N_0(0)^{2/5} \kappa\tau \left(1 - e^{-2t/(5\tau)}\right)\right)^{5/2}}. \tag{4.37}$$

Here $\tau = 1/\kappa_{bg}$ is the lifetime of the condensate in the static lattice. As this static lifetime changes with scattering length we measure it for every scattering length

[4] For details on why these shaking frequencies were chosen refer to section 4.3.4

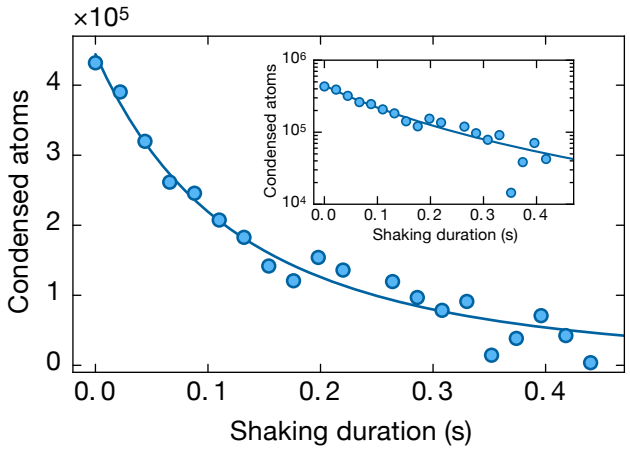

Figure 4.3: **Exemplary atom number decay versus shaking duration.** An example of a decay rate measurement. The driving strength is $\alpha = 1$ at a shaking frequency of $\omega = 2\pi \times 53\,\mathrm{kHz}$ and a scattering length of $a = 80\,a0$. The solid line is a fit to the data according to Eq. 4.37 with $N_0(0)$ and κ being the only fit parameters. The inset shows the same data on a logarithmic scale.

used further below. Therefore, the only fit parameters in Eq. 4.37 are the initial number of condensed atoms $N_0(0)$ and the driving induced loss rate κ.

Fig. 4.3 shows an exemplary decay rate measurement from which we infer the loss rate κ.

4.3.4 Single-particle multiphoton resonances

In section 4.1 we have seen that single-particle multiphoton resonances occur at specific shaking frequencies whenever the resonance condition

$$l\hbar\omega \approx \varepsilon_b(q) - \varepsilon_0(q), \tag{4.38}$$

is fulfilled. These single-particle resonances are independent of the interaction of the system and result in sharp resonance features, where the lifetime of the condensate in the shaken lattice is dramatically reduced [119, 181]. As we are interested in interaction dependent heating effects, it is crucial to avoid these single-particle resonances as they would spoil the measurements. To do so, we perform a frequency scan over a wide range of shaking frequencies. Therefore, we load a weakly interacting condensate with a scattering length of $a = 60\,a_0$ into the $11\,E_r$ lattice and start shaking the lattice with a driving strength of $\alpha \simeq 0.9$.

Figure 4.4 shows the normalized atom number after shaking the lattice for a fixed duration of 100 ms for driving frequencies below $0.7\,\omega_{10}$ and 50 ms for shaking frequencies above $0.7\,\omega_{10}$. Here $\omega_{10} = 2\pi \times 41.6\,\mathrm{kHz}$ denotes the first interband exci-

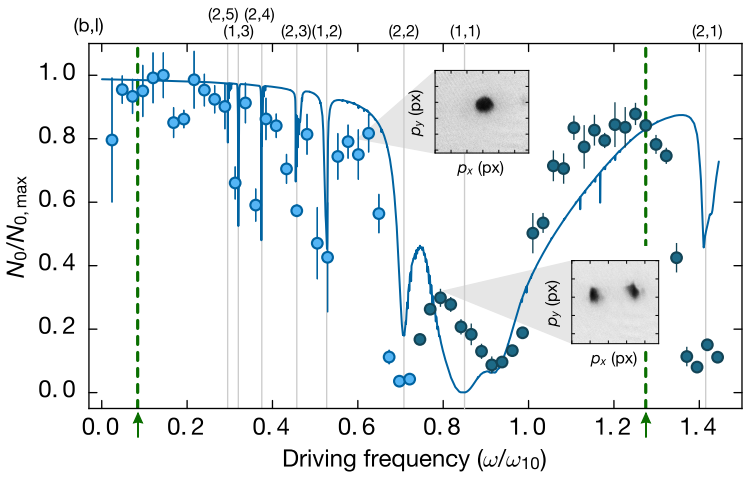

Figure 4.4: **Frequency scan.** Normalized atom number after shaking the lattice for 50 ms (for $\omega/\omega_{10} > 0.7$, marked in dark blue) or 100 ms (for $\omega/\omega_{10} < 0.7$, marked in light blue) with variable frequency at a driving strength of $\alpha \simeq 0.9$. Error bars indicate the standard error of the mean from four measurements per data point. The solid blue line shows the theoretically expected single-particle excitations to higher bands. Thin lines mark the resonance positions of multiphoton transitions with photon number l to higher lying bands b labeled by (b, l). Green dashed lines mark the frequencies used to study interaction dependent heating. In the frequency region from roughly $0.7\,\omega_{10}$ to $1.1\,\omega_{10}$ we observe a splitting of the BEC due to two degenerate minima in the lowest dressed band. This effect is included in the theory curve. The insets show raw quasimomentum images of the BEC.

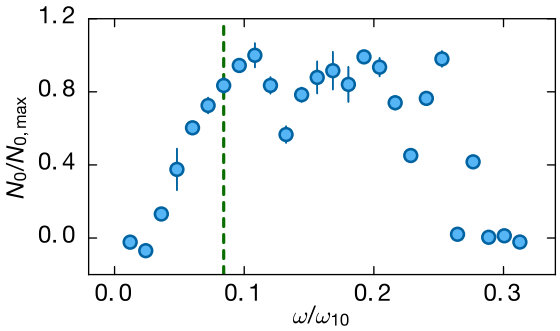

Figure 4.5: **Frequency scan at low shaking frequencies.** Zoom into the regime of small driving frequencies of Fig. 4.4 but with an increased driving strength of $\alpha = 2.2$ and a longer shaking duration of 200 ms to be able to better resolve multiphoton resonances with a large photon number l. The green dashed line marks the position at which we measure the interaction dependent heating rates. This shaking frequency lies well below the first observable multiphoton resonance at about $\omega \approx 0.13\,\omega_{10}$.

tation frequency from $b = 0$ to $b' = 1$ at zero momentum in the static lattice. To get a better resolution of the resonance positions we reduce the shaking duration for $\omega > 0.7\omega_{10}$ due to the overall larger heating rates in this regime. The solid blue line shows the result of a numerical single-particle simulation assuming a Gaussian width of the condensate in momentum space of $\Delta q = 0.2\pi/d$, see section 3.4.4. In the numerical simulation, the single-particle time evolution is integrated over time starting from the undriven Bloch state of the lowest band. The plotted line corresponds to the minimal encountered probability for remaining in this Bloch state during the time evolution. To include the momentum spread of the BEC, the result is averaged over a group of quasimomenta k_x representing the measured momentum distribution of the condensate. For a more detailed description of this numerical simulation refer to [119, 181].

At this driving strength of $\alpha \simeq 0.9$, we can observe clear resonance features that correspond to multiphoton excitations up to fifth order, see Fig. 4.4. For small shaking frequencies these multiphoton excitations are exponentially suppressed. Therefore, we perform a second frequency scan at low shaking frequencies with an increased driving strength of $\alpha = 2.2$. This driving strength is slightly larger than the largest α used later on in section 5.2. Figure 4.5 shows the frequency scan at this driving strength. We can observe a first multiphoton resonance appearing at around $0.13\,\omega_{10}$.

For our future analysis of interaction induced heating rates, we choose shaking frequencies of $\omega_l = 2\pi \times 3.5\,\mathrm{kHz} = 0.084\,\omega_{10}$ and $\omega_h = 2\pi \times 53\,\mathrm{kHz} = 1.27\,\omega_{10}$. Both of these frequencies are reasonably far away from multiphoton resonances and

represent the two different driving regimes introduced in sections 2.3.5 and 2.3.6. For the low shaking frequency ω_l, the tunneling matrix element of the lowest band gets renormalized by a Bessel function resulting in, for example, dynamic localization [3, 10, 196]. For the high shaking frequency ω_h, the dispersion relation acquires a double minimum for strong enough driving, which can be exploited to study, for example, the formation of symmetry-broken domains [45, 46].

Chapter 5

Heating rates in a 1D lattice

In this chapter, we will determine the dimensionless scattering parameter γ_l for both shaking regimes that we found in the previous section. Having determined γ_l, one can then calculate the total theoretically expected scattering rate Γ_{tot} and compare it to the experimentally measured heating rate κ.

In a first step to calculate γ_l we have to find suitable gauge transformations $\hat{U}(t)$ for the two different shaking regimes, such that the transformed Hamiltonian $\hat{H}'(t)$ takes the desired form discussed in section 4.2.2, where Fourier components with $m \neq 0$ of $\hat{H}'(t)$ are small. This property of $\hat{H}'(t)$ is necessary in order to employ perturbation theory, as discussed in section 4.2.3, to calculate the matrix elements $C^{(l)}_{b'b}$ from which we can then determine the scattering parameter γ_l.

Furthermore, these transformations will be chosen such that the transformed Hamiltonian $\hat{H}'(t)$ can be decomposed as

$$\hat{H}'(t) = \hat{H}_{\text{bs}} + \sum_m \left(\hat{H}^{(m)}_{\text{sp}} + \hat{H}^{(m)}_{\text{tp}} \right) e^{im\omega t}. \tag{5.1}$$

Here $\hat{H}_{\text{bs}}$ describes the time-independent single-particle band structure

$$\hat{H}_{\text{bs}} = \sum_{b,\boldsymbol{k}} \varepsilon'_b(\boldsymbol{k}) \hat{a}^\dagger_{b,\boldsymbol{k}} \hat{a}_{b,\boldsymbol{k}}, \tag{5.2}$$

where $\hat{a}_{b,\boldsymbol{k}}$ is the bosonic annihilation operator for a boson in the single-particle state $|b, \boldsymbol{k}\rangle'$. The total energy of the particles is given by the sum of the energy within the Floquet band structure $\varepsilon'_b(k_x)$ and the energy in the perpendicular lattice directions $E_\perp(\boldsymbol{k}_\perp)$

$$\varepsilon'_b(\boldsymbol{k}) = \varepsilon'_b(k_x) + E_\perp(\boldsymbol{k}_\perp). \tag{5.3}$$

All other (time-dependent) single-particle terms are collected in the Hamiltonian $\hat{H}_{\text{sp}}(t)$. The Fourier components $\hat{H}^{(m)}_{\text{sp}}$ of this Hamiltonian are given by

$$\hat{H}^{(m)}_{\text{sp}} = \sum_{\boldsymbol{k}} \sum_{b,b'} A^{(m)}_{b'b,\boldsymbol{k}} \hat{a}^\dagger_{b',\boldsymbol{k}} \hat{a}_{b,\boldsymbol{k}}. \tag{5.4}$$

Similarly, we express the Fourier components of the interaction dependent Hamiltonian $\hat{H}_{\mathrm{tp}}(t)$, which describes two-particle scattering processes, as

$$\hat{H}_{\mathrm{tp}}^{(m)} = \sum_{\{b,\boldsymbol{k}\}} B_{\{b,\boldsymbol{k}\}}^{(m)} \hat{a}_{b_4,\boldsymbol{k}_4}^{\dagger} \hat{a}_{b_3,\boldsymbol{k}_3}^{\dagger} \hat{a}_{b_2,\boldsymbol{k}_2} \hat{a}_{b_1,\boldsymbol{k}_1}. \tag{5.5}$$

Furthermore, the matrix elements $B_{\{b,\boldsymbol{k}\}}^{(m)}$ will be zero if (quasi)momentum is not conserved, modulo reciprocal lattice vectors, during such two-particle scattering processes.

A further prerequisite necessary to calculate the matrix elements $C_{b'b}^{(l)}$ via perturbation theory are the eigenstates $|\boldsymbol{n}\rangle$ of $\hat{H}'^{(0)}$. We approximate them in the basis of Fock states

$$|\boldsymbol{n}\rangle = \prod_{b,\boldsymbol{k}} \frac{\left(\hat{a}_{b,\boldsymbol{k}}^{\dagger}\right)^{n_{b,\boldsymbol{k}}}}{\sqrt{n_{b,\boldsymbol{k}}!}} |\mathrm{vac}\rangle\,, \tag{5.6}$$

where $n_{b,\boldsymbol{k}}$ is the occupation number of the Bloch state $|b,\boldsymbol{k}\rangle'$ and $|\mathrm{vac}\rangle$ denotes the vacuum state. The energy of the Fock state $|\boldsymbol{n}\rangle$ is given by

$$\varepsilon_{\boldsymbol{n}} = \sum_{b,\boldsymbol{k}} n_{b,\boldsymbol{k}} \varepsilon_b'(\boldsymbol{k}). \tag{5.7}$$

Lastly let us remark on the future notation of some important states. We will denote the ground state of the condensate as $|0\rangle$. This state is given by all particles occupying the condensate mode in the lowest band $|b=0,\boldsymbol{k}=\boldsymbol{q}\rangle'$. Furthermore, we need a Fock state where two particles occupy the excited states $|b_1,\boldsymbol{k}_1\rangle'$ and $|b_2,\boldsymbol{k}_2\rangle'$, while all other particles remain in the ground state of the condensate. We shall denote this state by $|2(b_1,\boldsymbol{k}_1;b_2,\boldsymbol{k}_2)\rangle$.

5.1 The scattering parameter for small shaking frequencies

In this section, we will describe the gauge transformations for shaking frequencies much smaller than the band gap that transform the shaking Hamiltonian $H(t)$ into the desired form discussed in the previous sections. We will give a detailed description of the general path on how the scattering parameter γ_l can be determined but will skip technical parts in between that give no further insight into the general strategy on how γ_l can be determined.

5.1.1 The rotating frame

The periodic forcing of the lattice leads to a periodic modulation of the quasimomentum of the condensate in the lattice. For the low shaking frequency case discussed here, this modulation eventually leads to the Bessel function renormalization of the tunneling matrix element of the lowest band as discussed in detail in section 2.3.5. In general, the effect of the drive on the (quasi)momentum of the atoms can be described by a wave number

$$v(t) = \frac{1}{\hbar}\int_0^t \mathrm{d}t' F(t') = -\frac{\alpha}{d}\sin(\omega t), \tag{5.8}$$

where $F(t) = -F_0\cos(\omega t) = -\alpha\hbar\omega/d\cos(\omega t)$ is the external forcing and $\alpha \equiv dF_0/(\hbar\omega)$ is the dimensionless forcing strength introduced in section 2.3.5.

For the lower driving frequency, where multiphoton resonances to higher lying bands are exponentially suppressed, the dynamics of the system is restricted to the lowest band. Hence, the translation in quasimomentum can be described by the time-periodic unitary operator

$$U_1(t) = \sum_{b,\boldsymbol{k}_x} |b, k_x + v(t)\rangle \langle b, k_x| = \exp\left(idv(t)\sum_{b,j} j\,|b,j\rangle\langle b,j|\right), \tag{5.9}$$

that conserves the band index b. Within the Fock space notation this transformation takes the form

$$\hat{U}_1(t) = \exp\left(idv(t)\sum_{b,j} j\hat{a}^\dagger_{b,j}\hat{a}_{b,j}\right). \tag{5.10}$$

Using this operator, we perform a gauge transformation on the single-particle Hamiltonian defined in Eq. 4.4. Within the notation of second quantization and neglecting the external trapping potential $V_{\mathrm{dip}}(\boldsymbol{r})$, the transformed Hamiltonian reads

$$\hat{H}_0'(t) = \sum_{b,\boldsymbol{k}}\left(E_b(\boldsymbol{k}+v(t))\hat{a}^\dagger_{b,\boldsymbol{k}}\hat{a}_{b,\boldsymbol{k}} + F_0 d\cos(\omega t)\sum_{b'\neq b}\eta_{b'b}\hat{a}^\dagger_{b',\boldsymbol{k}}\hat{a}_{b,\boldsymbol{k}}\right). \tag{5.11}$$

Here we have introduced the dimensionless interband coupling parameter $\eta_{b'b}$. Since the shaking frequency is very low, only interband couplings between the lowest band $b = 0$ and the first excited band $b = 1$ have to be taken into account. For these two bands, the wave function of the atoms in the lattice is well described by a Wannier function. As the lattice depth of $11\,E_r$ is already in the tight binding regime, the Wannier functions are well localized on a single lattice site and we can neglect interband couplings between different lattice sites. With these ingredients

we can approximate the interband coupling term in Eq. 5.11 by

$$\eta_{b'b}(k_x,t) \simeq \eta_{10} = \frac{1}{d}\int \mathrm{d}x w_1(x) x w_0(x). \tag{5.12}$$

Note that the interaction Hamiltonian as defined in Eq. 4.14 is not affected by this shift in quasimomentum imposed by the gauge transformation as it is independent of quasimomentum. In a next step we Fourier decompose the time-dependent energies $E_b(\boldsymbol{k}+v(t))$ appearing in Eq. 5.11. As we can spatially separate the Hamiltonian and since the time-dependence only appears along the lattice direction, the Fourier decomposition of the band energies reads

$$E_b(k_x+v(t)) = \sum_{m=-\infty}^{\infty} E_b^{(m)}(k_x) e^{im\omega t}. \tag{5.13}$$

Due to the large lattice depth, we can assume that the kinetics of the lowest band(s) is governed only by nearest-neighbor tunneling and we obtain

$$\begin{aligned} E_b^{(m)}(k_x) &= \frac{1}{T}\int_0^T \mathrm{d}t\, e^{-im\omega t}[\epsilon_b - 2J_b\cos(dk_x - \alpha\sin(\omega t))] \\ &= \epsilon_b\delta_{m,0} - J_b\mathcal{J}_m(\alpha)\left((-1)^m e^{idk_x} + e^{-idk_x}\right), \end{aligned} \tag{5.14}$$

where ϵ_b denotes the band-center energy.

In a last step, in order to get rid of the time-dependence of the diagonal terms $\propto \hat{a}^\dagger_{b,\boldsymbol{k}}\hat{a}_{b,\boldsymbol{k}}$ in Eq. 5.11, we perform a second gauge transformation where we integrate out the time-periodic part of the band energies $E_b(k_x+v(t))$. This gauge transformation has the form

$$\hat{U}_1'(t) = \exp\left[i\sum_{b,\boldsymbol{k}}\sum_{m\neq 0}\chi_{b,\boldsymbol{k}}^{(m)} e^{im\omega t}\hat{a}^\dagger_{b,\boldsymbol{k}}\hat{a}_{b,\boldsymbol{k}}\right], \tag{5.15}$$

with

$$i\chi_{b,\boldsymbol{k}}^{(m)} = -\frac{E_b^{(m)}(k_x)}{m\hbar\omega}. \tag{5.16}$$

As the execution of this last transformation is rather technical and provides no further insight into the general scheme on how the scattering rates in a driven lattice system can be calculated, we will only present the result of this transformation and refer the reader who is interested in the intermediate steps to the supplemental material of reference [197].

After the implementation of the gauge transformation presented in Eq. 5.15, the Hamiltonian is of the desired form $\hat{H}'(t) = \hat{H}_{\mathrm{bs}} + \hat{H}_{\mathrm{sp}}(t) + \hat{H}_{\mathrm{tp}}(t)$. We find that the

single particle matrix elements $A^{(m)}_{b'b,\boldsymbol{k}}$ are proportional to

$$A^{(\pm|m|)}_{b'b,\boldsymbol{k}} \propto (J_{b'} - J_b)\eta_{b'b}\frac{\alpha^{|m|}}{|m|!} \quad \text{for} \quad |m| \geq 2. \tag{5.17}$$

As it requires a large number of photons $l = -m$ to excite atoms to the first excited band, resonant scattering process between single-particles and l photons are strongly suppressed. Therefore, the single particle terms $A^{(m)}_{b'b,\boldsymbol{k}}$ can safely be neglected in this driving regime.

For the two particle matrix elements $B^{(m)}_{b,\boldsymbol{k}}$ one can again neglect scattering events to excited bands and we can restrict ourselves to resonant *intraband scattering* processes. The corresponding matrix element for a zero-photon (ordinary collision) process reads

$$B^{(0)}_{0,\boldsymbol{k}} \simeq \frac{g\zeta}{L^3}. \tag{5.18}$$

Inserting this expression into Eq. 5.5, we find that the interaction Hamiltonian $\hat{H}_{\text{int}} \simeq \hat{H}^{(0)}_{\text{tp}}$. For $m \neq 0$ we find the matrix elements to be given by

$$B^{(m)}_{0,\boldsymbol{k}} \simeq \frac{g\zeta}{L^3}\frac{\mathcal{J}_m(\alpha)}{m}\frac{J_0}{\hbar\omega}\begin{cases} [\cos(dk_{x_1}) + \cos(dk_{x_2}) & \\ -\cos(dk_{x_3}) - \cos(dk_{x_4})] & \text{for even } |m| \\ & \\ \left[\frac{1}{i}\sin(dk_{x_1}) + \frac{1}{i}\sin(dk_{x_2})\right. & \\ \left.-\frac{1}{i}\sin(dk_{x_3}) - \frac{1}{i}\sin(dk_{x_4})\right] & \text{for odd } |m|\,. \end{cases} \tag{5.19}$$

One can see that the zero-photon matrix element $B^{(0)}_{0,\boldsymbol{k}}$ is larger than the matrix elements defined in Eq. 5.19 where $m \neq 0$. Therefore, zero-photon scattering events between two particles which lead to a thermalization of the system are faster than resonant m-photon scattering events. Hence, also from the theoretical side, we expect the system to stay in a global thermal equilibrium at this shaking frequency.

5.1.2 Scattering rate for small shaking frequencies

To finally determine the total scattering rate Γ_{tot} of atoms out of the condensate, we assume that all atoms initially occupy the lowest band at zero quasimomentum $q = 0$. Since the dominant heating process is resonant intraband scattering, a pair of condensate atoms initially in the condensate mode $|0, \mathbf{0}\rangle$ is scattered into the excited Bloch states $|0, \boldsymbol{k}\rangle$ and $|0, -\boldsymbol{k}\rangle$, such that (quasi)momentum is conserved. The dominant scattering process would be a single-photon scattering process described

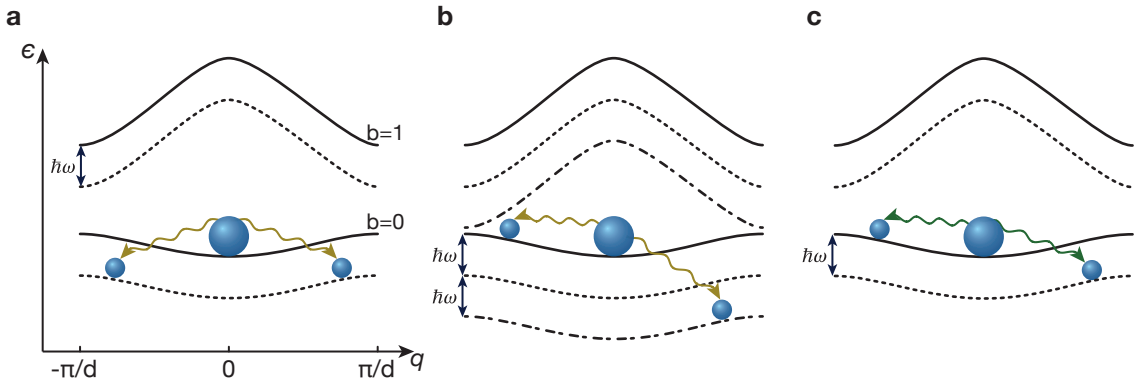

Figure 5.1: **Sketch of the dominant scattering channels. (a)** The dispersion relation of the lowest two bands $b = 0$ and $b = 1$ is sketched in solid black lines. Floquet modes of these bands that are shifted by $-\hbar\omega$ ($m = -1$) are indicated by the dashed lines. The condensate is represented by the large blue sphere, whereas scattered particles are indicated by the small spheres. The pair of yellow wiggly arrows denote a two-photon scattering process, which is the dominant scattering channel for a condensate with zero momentum spread when the shaking frequency is well below the band gap. Here, both particles each absorb a single photon during a collision event. Note that the matrix element $C_{00}^{(2)}$ describes a two-photon scattering process but does not differentiate how these absorbed photons are distributed between the scattered atoms. Therefore, the process depicted in (b) is equivalent to the process in (a). **(b)** Same process as in (a) but this time the scattered particle on the right absorbs two photons and ends up in the Floquet mode shifted by $-2\hbar\omega$ indicated by the dashed-dotted line. The other scattered particle remains in the Floquet mode with $m = 0$. Both processes in (a) and (b) are equivalent. **(c)** Due to the finite momentum spread of the condensate, single-photon scattering processes are also allowed and are illustrated by the green wiggly arrows.

by $B^{(1)}_{0,\boldsymbol{k}}$. However, this matrix element vanishes for atoms initially at $q = 0$ due to the sinusoidal dependence of the odd matrix elements defined in Eq. 5.19. Hence, the dominant scattering process is resonant two-photon scattering, which is illustrated in Fig. 5.1. As there are no virtual intermediate states present during such a scattering process, the scattering matrix elements $C^{(l)}_{b'b}(\boldsymbol{k}, \boldsymbol{q})$ for a resonant l-photon process are obtained via first order perturbation theory and read

$$\begin{aligned} C^{(l)}_{00}(\boldsymbol{k}, 0) &= \langle 2(0\boldsymbol{k}, 0-\boldsymbol{k})|\hat{H}^{(-l)}_{\mathrm{tp}}|0\rangle = N_0 B^{(-l)}_{0\boldsymbol{k},0-\boldsymbol{k},0\mathbf{0},0\mathbf{0}} && (5.20)\\ &\simeq -\frac{N_0 g}{L^3}\frac{\zeta J_0}{\hbar\omega}\frac{\mathcal{J}_l(\alpha)}{l/2}[1-\cos(dk_x)]. && (5.21)\end{aligned}$$

To calculate the dimensionless scattering rate γ_l we have to differentiate between two cases. As long as the total absorbed energy $l\hbar\omega$ from the drive is larger than twice the width of the lowest dressed band $8J_0\mathcal{J}_0(\alpha)$ all modes k_x will contribute to the integral[1]

$$\gamma_l = \left(\frac{2\zeta J_0 \mathcal{J}_l(\alpha)}{l\hbar\omega}\right)^2 \underbrace{\frac{d}{2\pi}\int_{-\pi/d}^{\pi/d} \mathrm{d}k_x\,[1-\cos(dk_x)]^2}_{3/2}. \tag{5.22}$$

However, if

$$s_l \equiv \frac{l\hbar\omega}{8J_0\mathcal{J}_0(\alpha)} < 1, \tag{5.23}$$

only modes with $|k_x| \leq k_{\max}$, where $[1-\cos(dk_{\max})] = 2s_\nu$, can fulfill the energy conservation condition for a scattering process defined in Eq. 4.26. In order to obtain a general formula for γ_l we define the function

$$\begin{aligned} g(s_l) &\equiv \frac{2}{3}\frac{d}{2\pi}\int_{-k_{\max}}^{k_{\max}} \mathrm{d}k_x\,[1-\cos(dk_x)]^2\\ &= \left(\frac{1}{2} - \frac{1}{\pi}\arcsin(1-2s_l)\right) - \frac{2s_l+6}{3\pi}\sqrt{s_l(1-s_l)}. && (5.24)\end{aligned}$$

Furthermore, we define that $g(s_l) = 1$ for $s_l \geq 1$. With these definitions, the general form of the dimensionless scattering parameter γ_l for driving frequencies far below the band gap is given by

[1] In the described heating channel two particles are always excited out of the condensate. Hence, the total energy necessary to excite both particles into the mode at $k_x = \pi/d$ is twice the energy associated with the bandwidth.

$$\gamma_l = 6g(s_l)\left(\frac{\zeta J_0 \mathcal{J}_l(\alpha)}{l\hbar\omega}\right)^2. \tag{5.25}$$

So far we have assumed that the condensate is described by a single quasimomentum wavenumber and thus has zero momentum spread. However, Fig. 3.18 shows that the condensate has an estimated momentum spread of about $\Delta q = 0.2\,\hbar k_L$ and therefore the odd matrix elements in Eq. 5.19 cannot be entirely neglected anymore. The largest of these matrix elements describes a single-photon scattering event, which is depicted in Fig. 5.1 (c). We take the finite momentum spread of the condensate into account by describing the initial state of the condensate by

$$|0\rangle = \frac{1}{\sqrt{N_0!}}\Big(\underbrace{\sum_q f_q \hat{a}_q^\dagger}_{\hat{a}_c^\dagger}\Big)^{N_0}, \tag{5.26}$$

where f_q describes the quasimomentum distribution of the condensate, which can be approximated by a Gaussian. With this definition the scattered state $|2(b_1, \boldsymbol{k}_1; b_2, \boldsymbol{k}_2)\rangle$ can be described by

$$|2(0, \boldsymbol{k}_1; 0, \boldsymbol{k}_2)\rangle = \hat{a}^\dagger_{0,\boldsymbol{k}_1}\hat{a}^\dagger_{0,\boldsymbol{k}_2}\frac{\hat{a}_c^2}{\sqrt{N_0(N_0-1)}}\,|0\rangle\,. \tag{5.27}$$

By inserting this expression into the matrix elements $C_{00}^{(l)}(\boldsymbol{k}, 0)$ defined in Eq. 5.20, we can determine the dimensionless scattering parameter γ_l for arbitrary momentum spreads of the condensate. The resulting scattering parameter only differs by a numerical factor $u(q)$ from the one defined in Eq. 5.25 and reads

$$\gamma_l = 6g(s_l)u(q)\left(\frac{\zeta J_0 \mathcal{J}_l(\alpha)}{l\hbar\omega}\right)^2. \tag{5.28}$$

For the measured momentum spread of our system, the numerical factor reads $u(q = 0.2\hbar k_L) = 0.75$ for processes with even l and $u(0.2\hbar k_L) = 0.15$ for odd l. By inserting this expression of γ_l into Eq. 4.36 we can calculate the expected scattering rate Γ_l^{LDA} of particles out of the condensate. The total scattering rate Γ_{tot} is given by summing the individual scattering rates Γ_l^{LDA}. In the case of low shaking frequencies, as discussed here, we include scattering processes up to $l = 4$.

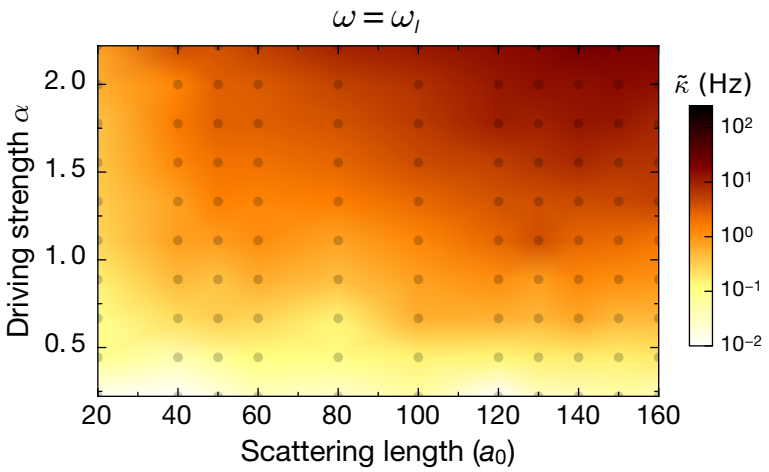

Figure 5.2: **2D map of heating rates at $\omega_l = 2\pi \times 3.5\,\mathrm{kHz}$.** Scaled loss rate $\tilde{\kappa} = \kappa N_0(0)^{2/5}$ for different driving strengths and scattering lengths. Each dot corresponds to a single lifetime measurement.

5.2 Comparison of theory and experiment for small shaking frequencies

To compare the theoretically estimated interaction dependent scattering rates with the experimentally measured heating rates, we choose for the regime of low shaking frequencies, a shaking frequency of $\omega = 2\pi \times 3.5\,\mathrm{kHz} = 0.084\,\omega_{10}$, see section 4.3.4. This frequency is far away from the first observable multiphoton resonance, as can be seen from Fig. 4.5, and hence only interaction driven heating should occur. Figure 5.2 shows a 2D map of the measured heating rates for various scattering lengths and driving strengths α. One can observe the expected behavior that stronger driving and larger scattering lengths increase the heating rate of the system quite dramatically. We observe that, depending on the driving regime, the heating rates change by almost three orders of magnitude! This impressively demonstrates the possible detrimental effect lattice shaking can have on a condensate. To present the measured loss rate κ in more intuitive units, we plot the data in Fig. 5.2 in units of the scaled loss rate $\tilde{\kappa} \equiv \kappa N_0(0)^{2/5}$. With this definition of $\tilde{\kappa}$, the initial driving-induced losses scale as $\dot{N}_0 \propto \tilde{\kappa} N_0(0)$.

In order to be able to compare the measured heating rates quantitatively with theory, we will have to take into account that scattered particles cannot directly leave the trapping potential at this driving frequency and initially stay trapped. This is the case because the depth of the trapping potential is around $V_{\mathrm{ver}} \approx h \times 20\,\mathrm{kHz}$ and therefore much deeper than the absorbed energy single atoms can maximally

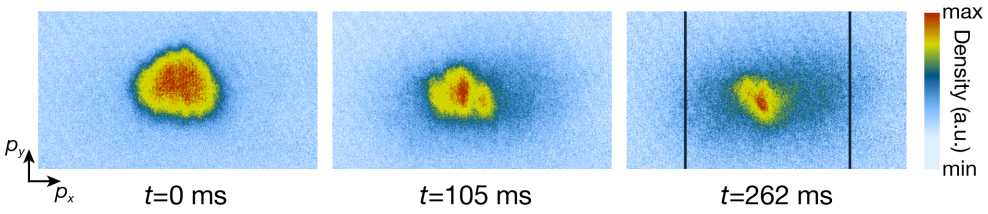

Figure 5.3: **Thermal background.** Three raw images of the BEC after different shaking durations t, at a driving frequency of $\omega_l = 2\pi \times 3.5\,\mathrm{kHz}$. The images are obtained by band mapping and subsequent 5.5 ms TOF, such that the thermal background is not strongly diluted, yet. One can clearly see the occurrence of a strong thermal background for increasing shaking durations. In the right image, the edges of the first Brillouin zone are indicated by the two vertical lines. This illustrates that the thermal background is distributed over the entire Brillouin zone.

acquire during a scattering process at this shaking frequency[2]. This effect manifests itself also in the TOF images. Figure 5.3 shows raw images of the BEC for different shaking durations. One can clearly see the occurrence of a strong thermal background. As these thermal atoms are still trapped and spatially overlapped with the condensate, they will rapidly dissipate their absorbed energy into the system. In the following section, we will estimate the detrimental effect of these additional collisions on the condensate.

5.2.1 Additional losses through thermalization

To estimate the additional losses of condensed atoms originating from ordinary collisions between thermal and condensed atoms, we assume that the system equilibrates immediately[3]. The depletion $N' = N - N_0$ of an ideal Bose gas, with density of states $g(E) \equiv cE^\gamma$ [198], where c and γ are system dependent constants, is given by

$$N' = \int_0^\infty \mathrm{d}E g(E) \frac{1}{e^{\beta E} - 1} = \frac{c\Gamma(\gamma+1)\zeta(\gamma+1)}{\beta^{\gamma+1}}. \tag{5.29}$$

Here β is the inverse temperature of the system and $\Gamma(x)$ and $\zeta(x)$ are the Gamma and Zeta function, respectively. The total energy of the system is given by

[2] If a single atom absorbs both photons during a scattering event its energy increases by maximally $2\hbar\omega = 2\pi\hbar \times 7\,\mathrm{kHz}$.

[3] In Fig. 4.2 we already saw that the system stays in a global thermal equilibrium as the BEC is well described by a Thomas-Fermi distribution during most parts of the driving. This observation is corroborated by the fact that the zero photon scattering matrix element $B^{(0)}_{0,\boldsymbol{k}}$ defined in Eq. 5.18 is larger than $B^{(2)}_{0,\boldsymbol{k}}$ so that the assumption of a thermal equilibrium is reasonable.

$$E = \int_0^\infty \mathrm{d}E' g(E') \frac{E'}{e^{\beta E'} - 1} = \frac{c\Gamma(\gamma+2)\zeta(\gamma+2)}{\beta^{\gamma+2}}. \tag{5.30}$$

By employing the property $\Gamma(\gamma+1)/\Gamma(\gamma+2) = \gamma+1$, we find that the absorption of an energy amount E changes the depletion of the condensate by

$$\frac{\mathrm{d}N'}{\mathrm{d}E} = \frac{1}{\gamma+2}\frac{\zeta(\gamma+1)}{\zeta(\gamma+2)}\beta \equiv f\beta. \tag{5.31}$$

A homogeneous, three-dimensional ideal Bose gas is described by $\gamma = 1/2$ which results in a factor $f \approx 0.78$. On the other hand, a three-dimensional harmonic oscillator would be described by $\gamma = 2$ which would yield $f \approx 0.28$. Note that the system is not described correctly by the ideal Bose gas or the harmonic oscillator. Especially for the low-energy states present in our system, the excited particles see a potential that is given by a combination of the trapping potential and a central repulsive potential bump which originates from the repulsive interaction with the condensate. Therefore, we use the factor f originating from the ideal three-dimensional Bose gas, which is also in the spirit of the local density approximation that we used earlier to determine the scattering rate Γ_l^{LDA}. Despite the uncertainty of the actual value of f, we can safely assume that it is of order one.

During a l-photon scattering event, two particles of the condensate absorb the energy $l\hbar\omega$ from the drive, which is then immediately dissipated into the system. Therefore, the depletion increases by about $lf\beta\hbar\omega/2$ for each scattered atom and we can express the total loss rate of condensate atoms by

$$\dot{N}_0 = -f\beta\hbar\omega \sum_{l>0} \frac{l}{2}\Gamma_l^{\mathrm{LDA}}. \tag{5.32}$$

5.2.2 Heating rates versus scattering length

From the theoretically estimated scattering rates, we expect that the driving induced losses scale with the scattering length as $\dot{N}_0 \propto a^{7/5}$. This scaling is reproduced by the data as can be seen from Fig. 5.4, demonstrating that the dominant loss processes are indeed interaction driven and that the Thomas-Fermi local-density approximation is consistent with our data. To overlap the theory lines with the measured data points, a factor $f\beta\hbar\omega = 10$ has been chosen. From this factor and assuming an ideal homogeneous Bose gas, as discussed in the previous section, we can provide a lower bound of the temperature of the condensate of about $T \approx 15\,\mathrm{nK}$. However, typical temperatures of our BEC will likely be slightly higher. For a homogeneous ideal Bose gas the condensate fraction is given by [199]

$$\frac{N_0}{N} = 1 - \left(\frac{T}{T_c}\right)^{3/2}. \tag{5.33}$$

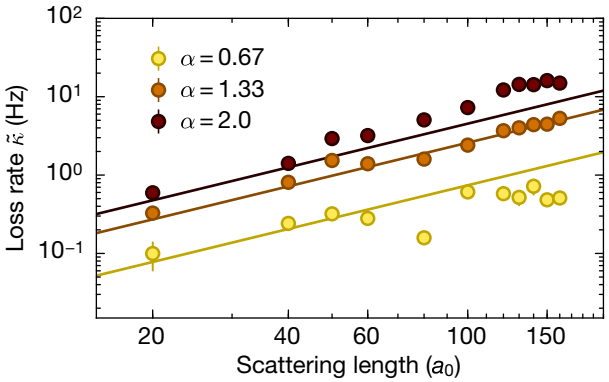

Figure 5.4: **Loss rate versus scattering length.** Effective loss rate $\tilde{\kappa}$ for different scattering lengths at a driving frequency of $\omega_l = 2\pi \times 3.5\,\mathrm{kHz}$. Error bars indicate fit uncertainties. The theory lines are scaled by eye with a factor $f\beta\hbar\omega = 10$ to overlap with the data.

In the static system we cannot detect any thermal background when taking TOF images of the condensate. Thus we can conservatively infer a condensate fraction of at least 90%. Inserting this condensate fraction into Eq. 5.33 gives an upper bound of the temperature of the BEC of around $T < 60\,\mathrm{nK}$. This temperature would yield $f\beta\hbar\omega > 2$ which is compatible with the measured factor of approximately ten. Note that due to the approximations made above, we do not expect a perfect match between the observed and estimated factor between theory and the experimental data. Furthermore, an additional heating mechanism will come into play which we have neglected so far. Since the trapped thermal atoms have a finite quasimomentum in the lattice (see Fig. 5.3) resonant single photon scattering events are not suppressed anymore and become the dominant scattering channel. Since the matrix element of this scattering channel is larger than the two-photon scattering matrix element, thermal atoms absorb energy from the drive at an even faster rate than condensed atoms.

5.2.3 Heating rates versus driving strength

Figure 5.5 (a) shows the measured loss rates for three different scattering lengths versus the driving strength α. One can see a good agreement between the scaled theory with $f\beta\hbar\omega = 10$ and the measured data for small and intermediate scattering lengths. At the largest measured scattering length, the theoretical prediction has the least overlap with the data. We assume that the lower than expected heating rates at small driving strengths might come from an interplay between the actual heating rate that stems from the lattice shaking and continuous evaporation in the dipole trap. Since the absolute heating rates in this regime are rather small and the lifetime of the condensate is on the order of seconds for all scattering lengths,

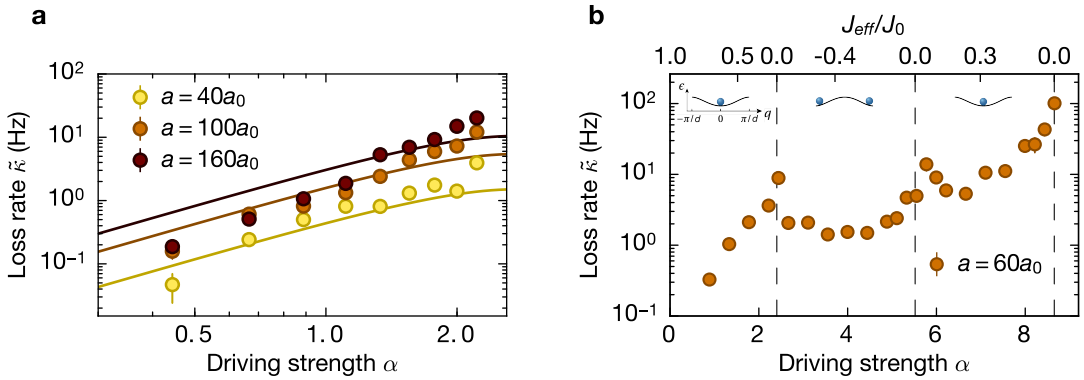

Figure 5.5: **Loss rate for different driving strengths. (a)** Effective loss rate $\tilde{\kappa}$ for different driving strengths α at a fixed shaking frequency ω_l. For moderate interaction strengths and scattering lengths, the theoretical description fits the data quite well. Solid theory lines are scaled by $f\beta\hbar\omega = 10$. Error bars indicate fit errors. **(b)** Loss rates for a wide range of driving strengths α. We observe clear peaks in the effective loss rate whenever the effective tunneling $J_{\text{eff}} = J_0\mathcal{J}_0(\alpha)$ goes to zero (dashed lines). The insets sketch the dispersion relation of the lowest band together with the equilibrium positions of the BEC (blue dots). Error bars indicate fit errors.

a slight increase in the photon scattering rate might partly be compensated by the more efficient evaporation from the dipole trap for stronger interacting condensates.

In the data of Fig. 5.5 (a) one can further observe a larger discrepancy between the measured loss rates and the theoretical prediction at large driving strengths α. We can attribute this effect to the very small bandwidth in this driving regime. As the bandwidth becomes negligibly small, zero-photon scattering processes are allowed. This effect is clearly visible when scanning the driving strength over a wide range shown in Fig. 5.5 (b). Here we observe clear maxima in the loss rate whenever the effective bandwidth of the lowest band is close to zero. Interestingly, after each zero crossing of the bandwidth, the loss rates decrease again even though the driving strength is increasing. This observation strongly supports the assumption that zero-photon scattering events become an additional important heating channel for bandwidths close to zero.

5.2.4 Heating rates for different shaking frequencies

When the total amount of absorbed energy $l\hbar\omega$ from the drive is smaller than twice the effective bandwidth $8J_0\mathcal{J}_0(\alpha)$ of the lowest band, we expect the heating rates to drop, as fewer modes k_x can be occupied along the lattice direction, see section 5.1.2. As one- and two-photon scattering processes are the dominant heating channels for small driving frequencies we expect to see this drop at two and one times the effective

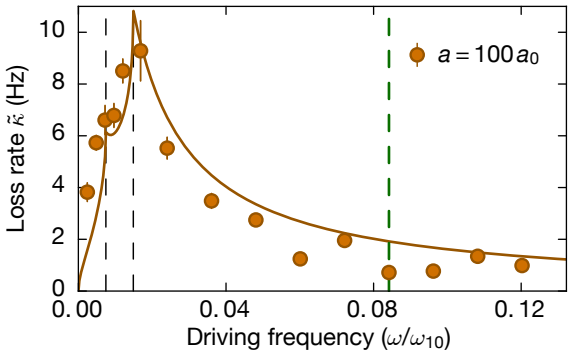

Figure 5.6: **Loss rate for different shaking frequencies.** Loss rates for a fixed driving strength of $\alpha = 1.1$. We observe peaks in the loss rate when the shaking frequency coincides with one or two times the effective bandwidth of the lowest band, indicated by the dashed black lines. When shaking below these frequencies, the number of accessible scattering states becomes reduced for two and single photon scattering processes, respectively. This reduction in target states leads to a reduced loss rate of condensed atoms. The solid line shows the theory scaled by $f\beta\hbar\omega$ for a temperature of $T = 13\,\mathrm{nK}$. The green dashed line marks the shaking frequency used in the previous sections.

bandwidth, as can clearly be seen in Fig. 5.6.

For frequencies larger than twice the bandwidth the heating rates decrease again according to the $1/\omega^2$ scaling of the scattering rates defined in Eq. 5.28. The theoretical estimate of the heating rate is plotted as a solid line. To calculate the theoretical heating rates, we assume a temperature of $T = 13\,\mathrm{nK}$ of the condensate, which gave us the scaling factor $f\beta\hbar\omega = 10$ for a shaking frequency of $\omega = \omega_l$. We see a generally good agreement between the measured heating rates and the theoretical expectation.

To conclude this section: we have observed a good agreement between the measured data and the theoretical prediction even though many approximations have been made in order to make the theoretical estimation tractable. The expected scaling with the interaction strength is in good agreement with the local-density Thomas-Fermi approximation. Furthermore, we also found good agreement in the behavior versus driving strength even though the measured loss rates show a richer structure than the predicted heating rates which should come at no surprise as many approximations have been made to estimate the loss rates. A further important impact on the heating rates is that excited atoms typically cannot directly leave the trap and therefore dissipate their entire energy into the system leading to heating rates that are an order of magnitude larger than expected. A powerful strategy to reduce heating rates in this shaking regime would, therefore, be a trapping configuration in which excited atoms can quickly leave the atom cloud before dissipating

their energy.

5.3 The scattering parameter for high shaking frequencies

Having determined the dimensionless scattering parameter for small shaking frequencies, we will now look at shaking frequencies that are larger than the band gap. In this shaking regime, scattering events that involve a single particle and one or more photons are not exponentially suppressed anymore but detuned, leading to entirely different heating channels as for the low-frequency case. We will start again by introducing a gauge transformation that brings the time-dependent Hamiltonian into the desired form introduced in Eq. 5.1. We will then describe the dominant heating channels and determine the scattering rate of particles out of the condensate.

5.3.1 The rotating frame

In section 2.3.6 we showed that for large driving frequencies ω, the lowest band(s) are not renormalized by a Bessel function, in contrast to the case for low shaking frequencies discussed in the previous sections. Instead, we find that below a critical driving strength α, the band structure remains more or less unaffected by the drive. Above this critical driving strength, the lowest band starts to exhibit a double-well-like structure as can be seen in Fig. 2.8. Furthermore, the approximation that the dynamics of the atoms are restricted to the lowest band is not valid anymore. Inspired by these observations, we employ a gauge transformation with the unitary operator

$$U_2(t) = \exp\left(iv(t)x\right), \tag{5.34}$$

which describes a translation in momentum rather than in quasimomentum. Here $v(t)$ is again the wave number defined in Eq. 5.8. Employing this transformation on the single particle Hamiltonian defined in Eq. 4.4, and again neglecting the external trapping potential, we obtain within the notation of second quantization

$$\hat{H}_0''(t) = \sum_{\{b,\boldsymbol{k}\}} E_b(\boldsymbol{k})\hat{a}^\dagger_{b,\boldsymbol{k}}\hat{a}_{b,\boldsymbol{k}} + \sum_{\{b'b,\boldsymbol{k}\}} V_{b'b}(k_x,t)\hat{a}^\dagger_{b',\boldsymbol{k}}\hat{a}_{b,\boldsymbol{k}}. \tag{5.35}$$

Here $\hat{a}^\dagger_{b,\boldsymbol{k}}$ is the creation operator that creates a particle in the undriven Bloch state $|b,\boldsymbol{k}\rangle$ whose energy is given by $E_b(\boldsymbol{k})$. The matrix elements $V_{b'b}(k_x,t)$ in Eq. 5.35 describe the effect of the periodic driving and are given by

$$V_{b'b}(k_x,t) = \frac{\hbar^2}{2M}\left(2v(t)p_{b'b}(k_x) + v^2(t)\delta_{b'b}\right). \tag{5.36}$$

Here we have introduced

$$p_{b'b}(k_x) = \langle b', k_x| - i\partial_x|b, k_x\rangle = k_x\delta_{b'b} + \frac{2\pi}{d}\beta_{b'b}(k_x), \tag{5.37}$$

with

$$\beta_{b'b}(k_x) = \sum_\beta u^*_{b',\beta}(k_x)\beta u_{b,\beta}(k_x), \tag{5.38}$$

where $u_{b,\beta}(k_x) = \langle\beta, k_x|b, k_x\rangle$ is the overlap between the momentum eigenstate $|\beta, k_x\rangle$ and the Bloch state $|b, k_x\rangle$. As for the case of low shaking frequencies, this gauge transformation does not affect the interaction Hamiltonian defined in Eq. 4.14. In a next step we again Fourier-decompose the time-dependent diagonal energies of the Hamiltonian defined in Eq. 5.35. As before, we can remove this time-dependence by employing a second gauge transformation with a unitary operator of the form defined in Eq. 5.15 and Eq. 5.16. After this transformation the Hamiltonian takes the desired form $\hat{H}''(t) = \hat{H}_{\rm bs} + \hat{H}_{\rm sp}(t) + \hat{H}_{\rm tp}(t)$. By Fourier decomposing the obtained single particle Hamiltonian $\hat{H}_{\rm sp}(t)$ and two particle Hamiltonian $\hat{H}_{\rm tp}(t)$ we obtain the matrix elements $A^{(m)}_{b'b,\boldsymbol{k}}$ and $B^{(m)}_{\{b,\boldsymbol{k}\}}$. In the limit of small driving strengths where $\alpha E_r/\hbar\omega$ is small, we find the single-particle matrix elements to be

$$\begin{aligned}
A^{(0)}_{b'b,\boldsymbol{k}}(\boldsymbol{k}) &= 0, &(5.39)\\
A^{(\pm1)}_{b'b,\boldsymbol{k}}(\boldsymbol{k}) &\simeq -E_r\frac{2\alpha}{\pi}\beta_{b'b}(k_x), &(5.40)\\
A^{(\pm2)}_{b'b,\boldsymbol{k}}(\boldsymbol{k}) &\simeq \pm\frac{E_r^2}{\hbar\omega}\left(\frac{2\alpha}{\pi}\right)^2\beta_{b'b}(k_x)[\beta_{b'b'}(k_x) - \beta_{bb}(k_x)]. &(5.41)
\end{aligned}$$

For the two-particle matrix elements we find

$$\begin{aligned}
B^{(0)}_{\{b,\boldsymbol{k}\}} &\simeq \frac{g}{2L^3}\zeta_{\{b,\boldsymbol{k}\}}, &(5.42)\\
B^{(\pm1)}_{\{b,\boldsymbol{k}\}} &\simeq \pm i\frac{g}{2L^3}\frac{E_r}{\hbar\omega}\frac{2\alpha}{\pi}\zeta_{\{b,\boldsymbol{k}\}}\big[k_{x_1} + k_{x_2} - k_{x_3} - k_{x_4}\\
&+ \beta_{b_1b_1}(k_{x_1}) + \beta_{b_2b_2}(k_{x_2}) - \beta_{b_3b_3}(k_{x_3}) - \beta_{b_4b_4}(k_{x_4})\big]. &(5.43)
\end{aligned}$$

With these matrix elements we have all the necessary ingredients to calculate the matrix elements $C^{(l)}_{b'b}(\boldsymbol{k},\boldsymbol{q})$.

5.3.2 Scattering rate for high shaking frequencies

To estimate the dimensionless scattering rate γ_l for high driving frequencies, we first have to identify the most dominant scattering processes. Compared to the low-frequency case, where the single-particle matrix elements $A^{(m)}_{b'b,\boldsymbol{k}}$ could be neglected, the determination of the dominant heating processes in the regime of high shaking frequencies is slightly more involved. We choose the dominant heating processes according to the following rules:

(i) We will only consider terms that involve the dominant matrix elements defined in Eq. 5.40 and Eq. 5.42, which describe single-photon interband transitions and zero-photon scattering (ordinary collisions) between particles, respectively.

(ii) We will assume that zero-photon scattering (ordinary collisions) events are slow compared to single-particle interband transitions, $gN_0/L^3 \ll E_r\alpha$. Therefore, within nth order perturbation theory we will only take into account a single zero-photon scattering process and $n-1$ single-particle interband processes.

(iii) We will only take into account processes that include virtual intermediate states which are detuned by a quasienergy much smaller than $\hbar\omega$.

According to these rules, the dominant heating processes which appear in second-order perturbation theory are depicted in Fig. 5.7 (a,b). Note that in this shaking regime, scattering processes that do not involve any virtual intermediate states, like the ones discussed in section 5.1.2, which would be treated in first order perturbation theory, are orders of magnitude lower than the dominant scattering channels depicted in Fig. 5.7 and can, therefore, be safely neglected. The two processes depicted in Fig. 5.7 (a,b) contribute to the matrix element $C^{(1)}_{10}(\boldsymbol{k},\boldsymbol{q})$. Note that as before, only one photon number m is associated with the whole system, meaning that mirror-inverted processes are equivalent to the processes shown in Fig. 5.7. From the resonance condition defined in Eq. 4.26 we can determine how much energy has to be transferred in the transverse direction. Furthermore, since $E_\perp(\boldsymbol{k}_1\perp) \geq 0$ we can ignore the matrix element $A^{(1)}_{b'b,\boldsymbol{k}}$ as it would correspond to a process where energy from the transverse direction would be converted into a photon during a collision process. The resulting scattering matrix element from the two processes depicted in Fig. 5.7 (a,b) reads

$$\begin{aligned} C^{(1)}_{10}(k_x,q) &= \frac{N_0 g}{L^3}\frac{\alpha}{\pi}\Bigg[-\frac{4E_r\beta_{10}(q)\zeta_{1010}(k_x,q)}{\hbar\omega-\Delta_{10}(q)} \\ &+ \frac{2E_r\beta_{10}(q+k_x)\zeta_{0000}(k_x,q)}{\hbar\omega-\Delta_{10}(q+k_x)}\Bigg], \end{aligned} \tag{5.44}$$

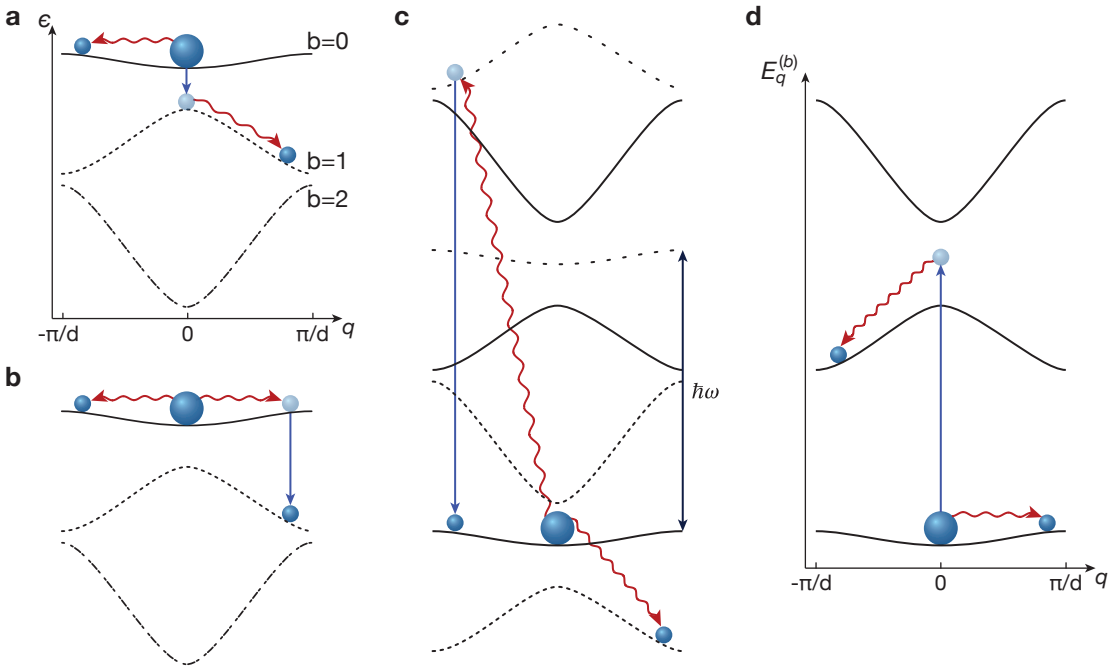

Figure 5.7: **Dominant heating channels for high shaking frequencies. (a,b)** Leading excitation channels in the regime of high driving frequencies. The dispersion relation of the lowest band is sketched by the solid black line. The Floquet mode of the second band shifted by $-\hbar\omega$ ($m = -1$) is depicted by the dashed line and the Floquet mode of the third band shifted by $-2\hbar\omega$ by the dashed-dotted line. The condensate is illustrated by the large blue sphere and scattered particles by the small spheres. The solid blue arrow indicates a single-photon interband transition described by the matrix element $A^{(-1)}_{b'b,\boldsymbol{k}}$ and the red wiggly arrows denote a zero-photon scattering process described by $B^{(0)}_{\{b,\boldsymbol{k}\}}$. Faint blue spheres indicate the virtual intermediate state. The zero-photon scattering process, during which excess energy gets transferred into the transverse directions, is possible as the virtual intermediate state is still spatially overlapped with the BEC. **(c)** As the processes in (a) and (b) attenuate each other, sub-dominant processes like the one indicated here will become important, although it violates the third selection principle. The larger spaced dashed lines indicate Floquet modes shifted by $\hbar\omega$ ($m = 1$). **(d)** Same process as pictured in (a) but plotted within a quantum optics like picture instead of the Floquet picture. One atom of the condensate absorbs a photon from the drive, as indicated by the blue arrow. This excitation into the virtual intermediate state, depicted by the faint blue sphere, is off-resonant. To reach an allowed energy state within the band structure, the excited atom has to scatter with another atom from the condensate. During this scattering process, depicted by the wiggly red arrow, excess energy gets transferred into the transverse directions.

which has the property that $C_{10}^{(1)}(k_x, q) = C_{10}^{(1)}(-k_x, q)$. In Eq. 5.44 we have introduced $\Delta_{b'b}(q) \equiv \varepsilon_{b'}(q) - \varepsilon_b(q)$, where $\varepsilon_b(q)$ denotes the energy of the bth Floquet band at quasimomentum q. Note that for driving strengths $\alpha \geq 0.75$ the lowest band starts to exhibit a double minimum and hence the condensate occupies a state with finite quasimomentum q. Furthermore, we find that the contributions from the processes depicted in Fig. 5.7 (a,b) have opposite sign and additionally have almost the same absolute value. As a result of this mutual attenuation of the dominant scattering processes, sub-dominant processes will become important. One of these processes is depicted in Fig. 5.7 (c). Compared to the processes in (a) and (b) it violates the third selection principle as the virtual intermediate state has a large detuning. Nevertheless, it leads to a significant correction of the matrix element $C_{10}^{(1)}(k_x, q)$ which reads

$$\frac{N_0 g}{L^3} \frac{\alpha}{\pi} \frac{2E_r \beta_{01}(q - k_x)\zeta_{1100}(k_x, q)}{\hbar\omega + \Delta_{10}(q - k_x)}. \tag{5.45}$$

Two-particle scattering processes that include the absorption of a single photon, which are described by the matrix element $B^{(-1)}_{1\boldsymbol{q}+\boldsymbol{k},0\boldsymbol{q}-\boldsymbol{k},0\boldsymbol{q},0\boldsymbol{q}}$, can safely be neglected when calculating the matrix elements $C_{10}^{(1)}(k_x, q)$. This is the case because they only acquire a non-zero value due to interaction processes between nearest neighboring lattice sites.

So far we only discussed matrix elements that appear in second order perturbation theory. However, matrix elements $C_{b'b}(k_x, q)$ that result from third order perturbation theory and therefore include two virtual intermediate states cannot be neglected and contribute a significant amount to the total scattering rate Γ_{tot}. The dominant scattering processes that appear in third order perturbation theory are sketched in Fig. 5.8.

The processes depicted in Fig. 5.8 (a-d) contribute to the matrix element $C_{11}^{(2)}(k_x, q)$ whereas the processes in Fig. 5.8 (e-h) contribute to $C_{20}^{(2)}(k_x, q)$. Both of these matrix elements scale quadratically with the driving strength α. Due to the increasing complexity of defining and calculating the matrix elements $C_{b'b}(k_x, q)$ in higher orders of perturbation theory, we are not going to take matrix elements into account that result from fourth or even higher orders of perturbation theory. Matrix elements from fourth order perturbation theory would scale as α^3 and would become dominant for large driving strengths α. According to Eq. 4.36, we can estimate the total scattering rate of particles out of the condensate as

$$\begin{aligned} \Gamma_{\text{tot}} &\approx \Gamma_1^{\text{LDA}} + \Gamma_2^{\text{LDA}} \\ &= \frac{128}{105}\zeta^{-3/5}\left(\frac{15\pi}{8}\frac{a}{d}N_0\right)^{7/5}\left(\frac{\hbar\bar{\omega}}{E_r}\right)^{6/5}\frac{E_r}{\hbar}(\gamma_1 + \gamma_2), \end{aligned} \tag{5.46}$$

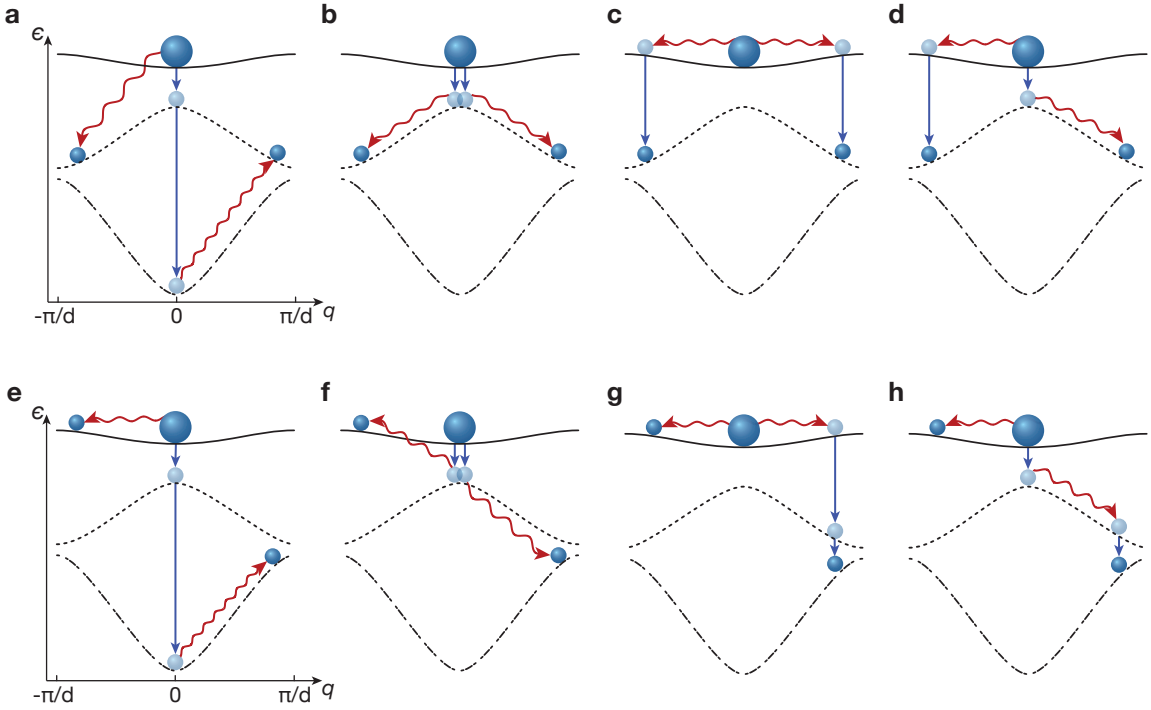

Figure 5.8: **Dominant heating channels in third order perturbation theory.** **(a-d)** Dominant scattering processes that include two single-photon processes and one zero-photon process which contribute to the matrix element $C_{11}^{(2)}(k_x, q)$. **(e-f)** Dominant scattering processes that contribute to the matrix element $C_{20}^{(2)}(k_x, q)$.

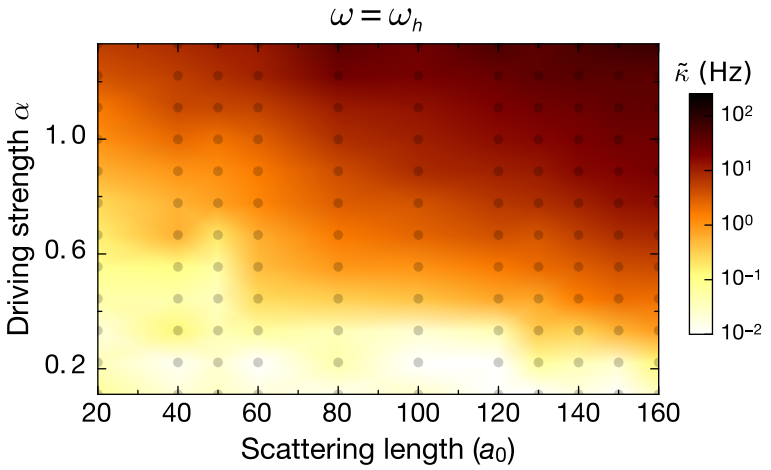

Figure 5.9: **2D map of heating rates at $\omega_h = 2\pi \times 53\,\mathrm{kHz}$.** Scaled loss rate $\tilde{\kappa} = \kappa N_0(0)^{(2/5)}$ for different driving strengths and scattering lengths. Each dot corresponds to a single lifetime measurement.

with dimensionless scattering parameters

$$\gamma_1 = \frac{d}{2\pi}\int_{-\pi/d}^{\pi/d} \mathrm{d}k_x \left(|c_{10}^{(1)}(k_x,q)|^2 + |c_{01}^{(1)}(k_x,q)|^2\right) \quad \text{and} \tag{5.47}$$

$$\gamma_2 = \frac{d}{2\pi}\int_{-\pi/d}^{\pi/d} \mathrm{d}k_x \left(|c_{11}^{(2)}(k_x,q)|^2 + |c_{20}^{(2)}(k_x,q)|^2 + |c_{02}^{(2)}(k_x,q)|^2\right), \tag{5.48}$$

where $c_{b'b}^{(l)}(k_x,q) = 1/n_{2D} C_{b'b}^{(l)}(k_x,q)$.

5.4 Comparison of theory and experiment for high shaking frequencies

As discussed in section 4.3.4, we choose a shaking frequency of $\omega_h = 2\pi \times 53\,\mathrm{kHz}$ to compare the experimentally measured heating rates with the theoretically estimated ones. This frequency was chosen because it lies in the middle of the band gap between the first and second excited band and is thus detuned from trivial single-particle multiphoton resonances. Therefore, interaction-driven heating as discussed in the previous sections should be the dominant heating process. Figure 5.9 shows an overview of the measured heating rates for various driving strengths and scattering lengths. This figure shows very close similarities to Fig. 5.2 although the scattering processes that lie at the heart of the heating processes are very different in the two shaking regimes. Another significant difference to the case of low shaking frequen-

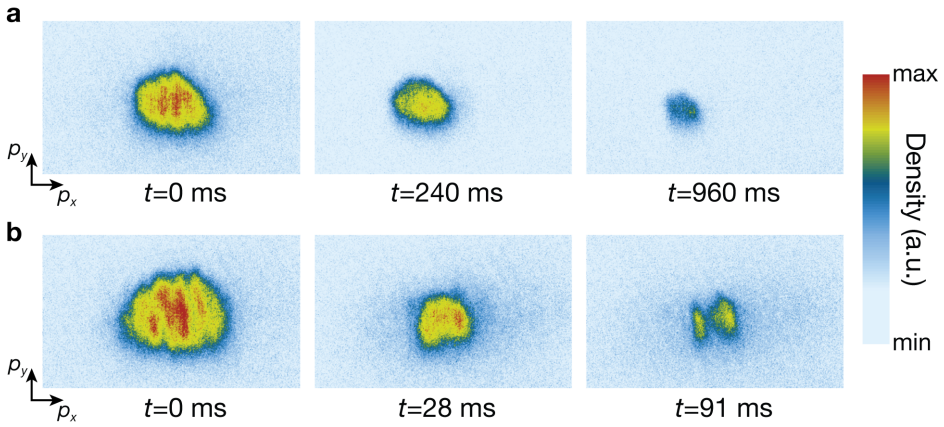

Figure 5.10: **Thermal background at large shaking frequencies. (a)** Three raw images of the BEC after different shaking durations t at a scattering length of $a = 40\,a_0$ and driving strength $\alpha = 1.1$. The images have been obtained after band mapping the atoms and imaging them after 5.5 ms TOF. This TOF is short enough that the thermal background is not strongly diluted, yet. Compared to the low frequency case in Fig. 5.3 there is no thermal background visible here. **(b)** Same as in (a) but with a larger scattering length of $a = 140\,a_0$. Here, a faint thermal background is visible which we attribute to the mean free path of the atoms becoming on the order of the size of the condensate. For more details see text.

cies discussed before is that the absorbed energy $\hbar\omega_h$ is typically large enough to directly remove scattered atoms from the trap. Because of this property we expect no thermal background to appear in this driving regime which is confirmed by TOF pictures shown in Fig. 5.10 (a). Since scattered particles directly leave the trap, we can assume that the measured heating rate coincides with the scattering rate

$$\dot{N}_0 = -\sum_{l>0} \Gamma_l. \tag{5.49}$$

5.4.1 Heating rates versus scattering length

Figure 5.11 shows the measured loss rates together with the calculated scattering rates for a driving frequency of $\omega_h = 2\pi \times 53\,\mathrm{kHz}$. As the theoretically estimated scattering rate should coincide with the measured loss rate in this frequency regime, no additional scaling with $f\beta\hbar\omega$ is applied, as was the case for low shaking frequencies. In Fig. 5.11 (a) we can see that the loss rates scale again as $\dot{N}_0 \propto a^{7/5}$ demonstrating that the measured loss rates are again interaction driven. However, we can see an increasing discrepancy from the $a^{7/5}$ scaling for scattering lengths larger than

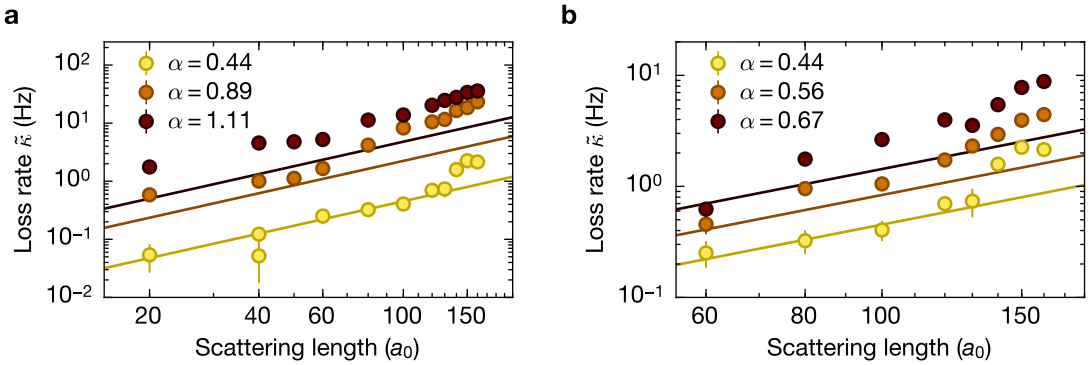

Figure 5.11: **Loss rate versus scattering length. (a)** Scaled loss rate $\tilde{\kappa}$ versus scattering length at a shaking frequency $\omega_h = 2\pi \times 53\,\mathrm{kHz}$. The solid lines show the theoretically estimated heating rates which agree quite well with the measured loss rates. Especially for weaker driving strengths, one can observe a distinctive kink in the measured loss rates for scattering lengths larger than approximately $130\,a_0$. We attribute this kink to additional collisions between excited and condensed atoms which are not captured by the theoretical description. **(b)** Zoom into the region around $130\,a_0$ for weaker driving strengths α. Due to the largely enhanced heating rates for stronger driving strengths, the effect of the secondary collisions on the heating rate becomes less important for large α.

$\simeq 130 a_0$. This effect is predominantly visible for small driving strengths where the overall heating rate is small. Figure 5.11 (b) shows a zoom into the aforementioned regime. The increasing discrepancy between theory and experiment can be explained by the mean free path $l_f = 1/\bar{n}\sigma$ of the atoms becoming on the order of the size of the BEC, see Fig. 5.12. Here $\bar{n} = N_0/V$ denotes the mean density of the condensate where the volume of the BEC can be approximated by $V = 4\pi/3 R^x_{\mathrm{TF}} R^y_{\mathrm{TF}} R^z_{\mathrm{TF}}$ and $\sigma = 8\pi a^2$ is the scattering cross-section of the atoms [85]. Consequently, as the mean free path is similar to the size of the condensate, scattered atoms have a finite probability to collide with condensed atoms while leaving the cloud. In Fig. 5.10 (b) one can indeed see the occurrence of a faint thermal background for condensates with larger scattering lengths. This supports the assumption that excited atoms can scatter with condensed atoms while leaving the cloud. After such a collision event, the typical energy of the particles is not high enough to leave the trap anymore and therefore the atoms stay trapped and form a thermal background. Due to the initially high energy of excited atoms, the amount of energy that can be dissipated into the system is considerably higher than in the low shaking frequency case discussed earlier. This means that already a few of these collision events between excited and condensed atoms can increase the heating rate significantly. However, the influence on the total heating rate of these secondary collisions is predominantly important for weak driving strengths α. For large α they become less important as

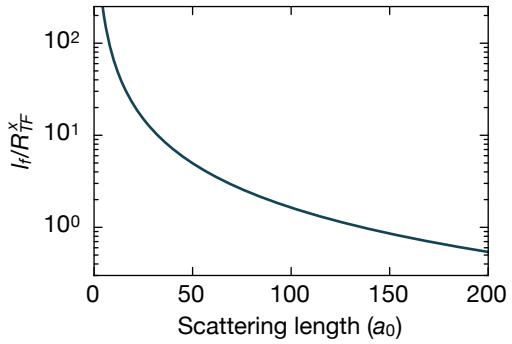

Figure 5.12: **Mean free path.** Estimated mean free path of the atoms. For scattering lengths larger than approximately $130a_0$ the mean free path becomes on the order of the size of the BEC in the horizontal direction, leading to a finite collision probability between excited and condensed atoms.

the single-particle matrix elements $A^{(m)}_{b'b,\boldsymbol{k}}$ become very large compared to the collision matrix element $B^{(0)}_{\{b,\boldsymbol{k}\}}$ and therefore these secondary collisions have almost no effect on the overall heating rate anymore.

Furthermore, we observe an increasing discrepancy between the theoretical prediction and the measured loss rates in Fig. 5.11 for larger driving strengths. We attribute this behavior to the fact that we have neglected scattering channels that include the absorption of more than two photons per scattering event. As already mentioned before, these processes will become more and more important for larger driving strengths.

5.4.2 Heating rates versus driving strength

Figure 5.13 shows crosscuts of the measured and calculated loss rates versus the driving strength α. The theory lines show a distinctive kink at a driving strength of $\alpha \simeq 0.7$. At this driving strength a double minimum occurs in the lowest band, resulting in the BEC condensing at finite values of q. Due to the finite momentum spread of the condensate, this kink gets washed-out and is not visible in the measured data. For increasing values of α, the minima of the lowest band move to larger values of q, which is for example depicted in Fig. 2.8. For driving strengths larger than $\alpha \simeq 1.4$, the minima of the lowest band approach an avoided crossing to higher lying excited bands which makes a theoretical determination of the minimum position impossible, see Fig. 2.8 (b). Therefore, we cannot determine a theoretical loss rate for $\alpha > 1.4$. Due to the appearance of a single-particle multiphoton resonance, the heating rates in this regime would in any case only be partly interaction driven. Experimentally, it is only possible to reliably determine loss rates for $\alpha > 1.4$ for

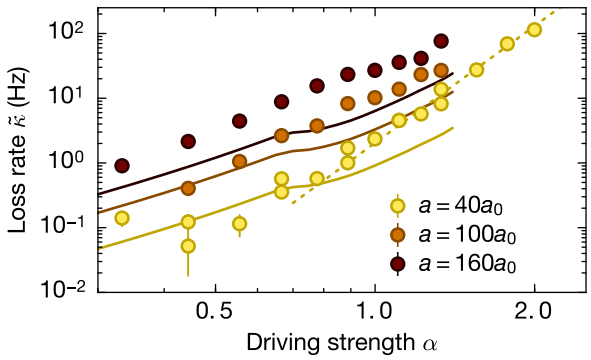

Figure 5.13: **Loss rate versus driving strength.** Scaled loss rate for different interactions versus driving strength α. The kink in the solid theory lines is due to the shift of the minima position of the lowest band to finite values of q when the driving strength exceeds a value of $\alpha \simeq 0.7$. For increasing α, a discrepancy between theory and experiment can be observed which we attribute to neglected scattering channels in the theoretical description. For driving strengths larger than $\alpha \simeq 1.4$ the minimum position of the lowest band cannot be calculated anymore due to the appearance of a single-particle multiphoton resonance. The dashed yellow line shows an α^6 fit to the data at large driving strengths.

weakly interacting systems with a small scattering length. Figure 5.13 shows some additional points in this driving regime for a scattering length of $a = 40\,a_0$. As discussed already briefly in the previous section, we can see an increasing discrepancy between the measured data and the theoretical estimation for larger values of α. We attribute this to the neglected matrix elements that include scattering processes with more than two photons. Nonetheless, despite the increased complexity of scattering channels we still get good agreement between the data and the theoretical description. Including the next higher order term in the theoretical description would reveal an α^6 scaling of the loss rate which would become dominant for larger values of α. The data for $a = 40\,a_0$ shows indeed a scaling with α^6 for driving strengths larger than approximately 0.8, which is indicated by the dashed yellow line in Fig. 5.13. This scaling seems to reproduce the data also for driving strengths $\alpha > 1.4$ where single-particle multiphoton resonances become important.

Chapter 6

Conclusion and Outlook

In this thesis, we have reported on the systematic study of interaction dependent heating rates of a BEC in a driven one-dimensional optical lattice. Apart from the experimental determination of heating rates, we have also developed a theoretical model based on Fermi's golden rule, to estimate loss rates of condensed particles for different driving strengths and shaking frequencies. By employing a Thomas-Fermi local-density approximation, we also took the density distribution of the trapped atoms into account. We focused our study on two frequency regimes which are experimentally most relevant for Floquet engineering and where interaction-induced scattering processes are the dominant heating channel.

The first considered regime is characterized by driving frequencies well below the band gap to the first excited band but above the bandwidth of the lowest band. Here the tunneling matrix element of the lowest band(s) get effectively renormalized by a Bessel function. Amongst others, this tuning possibility can be utilized for the dynamic localization of particles [9, 10, 44] or to induce the superfluid to Mott insulator transition in a dynamic way [48]. Furthermore, this shaking regime is also used for the creation of topological band structures [68, 69]. As the driving frequency is much smaller than the band gap, the dominant heating processes are resonant *intraband* scattering events. We found that the two most important heating channels are given by collision processes between two condensed particles during which one or two photons from the drive are being absorbed. These processes lead to loss rates $\dot{N}_0$ that scale with the driving strength α like $\mathcal{J}_1(\alpha)^2$ and $\mathcal{J}_2(\alpha)^2$, respectively. Furthermore, we found that scattered particles usually have not acquired enough energy to leave the trap directly and therefore dissipate their energy into the system. This effect and presumably additional heating channels that appear for thermal atoms at finite quasimomentum lead to a measured heating rate that is roughly a factor of ten larger than the theoretically estimated scattering rate. In agreement with the local-density Thomas-Fermi approximation, we found that the heating rates scale with the scattering length as $a^{7/5}$.

The second regime we investigated concerns driving frequencies that lie in the band gap between the first and second excited band. In this regime, a double minimum emerges in the lowest band for strong enough driving. This control over the

band structure has been used to study for example the formation of symmetry-broken domains [45, 200] or the dynamics of bosonic particles across a quantum phase transition [201]. As the driving frequency is larger than the band gap, the dominant heating processes are resonant *interband* scattering events. During such a scattering event a single particle absorbs up to l photons from the drive and energy conservation is granted through an ordinary collision process with a second particle from the condensate. Through this collision process excess energy gets transferred into the transverse directions. We found the dominant heating channels to be single- and two-photon scattering events which scale with the driving strength as α^2 and α^4, respectively. By comparing the experimental data and the theoretical estimation, we find generally good agreement for small driving strengths and scattering lengths. For larger interactions, we find an increasing discrepancy which we attribute to secondary collision events between excited and condensed atoms. These secondary collisions occur because the mean free path of excited atoms becomes on the order of the size of the condensate. For larger driving strengths the increasing discrepancy can be explained by the negligence of higher order processes that include the absorption of more than two photons. These processes were not taken into account due to the increasing complexity to calculate their scattering matrix elements. Furthermore, the amount of energy that gets absorbed from the drive during a scattering event is typically large enough for scattered atoms to leave the trap directly. As a result, no further scaling of the theoretically estimated scattering rates has been applied.

From the relatively good agreement between theory and experiment at large driving frequencies, we assume that our model adequately estimates scattering rates in a driven system. As the measured heating rates for small shaking frequencies are an order of magnitude larger than the estimated scattering rates with a major difference to the high shaking frequency case being that scattered atoms remain trapped, we deduce that the dissipation of absorbed energy into the system is a significant heating source. Therefore, a strategy to decrease heating rates in driven lattice systems is a trapping configuration where scattered atoms, even at small driving frequencies, can directly leave the trap. By doing so, one can assume to reduce the heating rates for low shaking frequencies up to a factor of about ten. As this direct "evaporation" process of excited particles already happens to a large extent in the regime of high shaking frequencies, this strategy cannot significantly reduce heating in this regime. A further possibility to reduce heating might be the use of a three-dimensional lattice structure. As in all our considered scattering processes excess energy gets transferred into transverse directions these heating channels should be forbidden in a three-dimensional lattice [76, 77]. Another possibility is the use of non-ergodic systems such as many-body localized systems [186–188]. It was already shown experimentally that heating in these systems can be suppressed for properly chosen driving frequencies [189].

6.1 Outlook

So far our analysis of heating rates focused on the one-dimensional optical lattice. This system was chosen due to its inherent simplicity. It enabled the derivation of analytical expressions for the heating rates and simplified the identification of the dominant heating processes. A next step would be to extend our knowledge to more complicated two- or even three-dimensional lattice structures. As our experimental setup is predominantly designed to work with a hexagonal lattice structure [89, 90], a logical next step is to determine the heating rates in this system.

In particular, a primary interest of our team is to explore topological band structures and, in preparation to this, different methods have been developed to measure the band geometry and topology [23, 202][1]. However, the so far conducted experiments in our lab were performed in topologically trivial bands. Combining periodic driving with hexagonal lattices would enable the creation of topologically non-trivial bands and the study of interesting topological phases that span from a quantum Hall effect without Landau levels [68, 70] over Majorana-Fermions [205] to Floquet topological or Floquet spin-Hall insulators [52, 206, 207] and fractional Chern insulators [208] to mention a few.

Many of the above-mentioned proposals require the combination of periodic driving with strong interactions. Therefore, it is important to study interaction dependent heating rates in the hexagonal lattice. In the following section, we will present preliminary data on heating rates obtained in a shaken honeycomb lattice.

6.1.1 Heating rates in a hexagonal lattice

To determine the positions of single-particle multiphoton resonances, we perform a frequency scan as we did for the one-dimensional lattice. Since the honeycomb lattice is comprised of two lattice sites per unit cell, the bands are grouped together, compare to Fig. 2.5, and we, therefore, expect an increased number of multiphoton resonances compared to the one-dimensional case.

We perform the frequency scan in a $4\,E_r$ deep lattice[2], where we ramp up the driving amplitude ν_0 within 10 ms to a final value of $\nu_0 = 10\,\mathrm{kHz}$. Here the recoil energy is defined as $E_r = \hbar^2 k_L^2/(2M)$, where $k_L = 2\pi/\lambda$. From the definition of the driving strength α in Eq. 3.28 one can see that the same absolute shaking amplitude ν_0 results in a weaker driving strength compared to the one-dimensional lattice. This

[1] Apart from these and similar interferometric techniques [203] other groups have developed measurement techniques to determine the topology of the band structure by measuring the Hall drift of accelerated wave packets [60, 68], projection onto flat bands [104] or by charge pumping [105, 106, 204].

[2] As the honeycomb lattice is created by three individual lattice beams which are derived from the same laser source and the tunneling barrier between neighboring lattice sites is only a single beam light shift, see Fig. 3.4, the maximum experimentally reachable lattice depth is much smaller than for the one-dimensional optical lattice.

is the case because the lattice spacing of the honeycomb lattice is smaller than the lattice spacing of the one-dimensional lattice. The chosen shaking amplitude of $\nu_0 = 10\,\mathrm{kHz}$ corresponds to a driving strength of $\alpha = 0.5$[3]. We perform frequency scans both for linear shaking where only one of the lattice beams is modulated and circular shaking, where two lattice beams are modulated out of phase with a phase difference of $\pi/3$. Figure 6.1 shows the normalized atom number after a shaking duration of 300 ms at a scattering length of $5\,a_0$. At a lattice depth of $4\,E_r$, the resonance frequency to the first excited (s-)band is at $\omega_{10} = 2\pi \times 9.5\,\mathrm{kHz}$. Compared to the case of a one-dimensional optical lattice one can observe broad frequency regions below ω_{10} where multiphoton resonances strongly reduce the lifetime of the condensate. However, one can see a wide frequency region above ω_{10} where no resonances are observed. This can be explained by the larger band gap of $\omega_{20} = 2\pi \times 36.5\,\mathrm{kHz}$ between the lowest s-band and the first p-band in the static lattice system.

In the case of circular shaking, the multiphoton excitation spectrum looks slightly different compared to the linearly shaken case. This observation can be explained by a different Floquet band structure as indicated in Fig. 6.2. Here we have only plotted the lowest two bands in order to obtain a better visibility of the band structure. Although circular shaking can yield topological band structures due to time-reversal-symmetry breaking, we mainly focus on linear shaking to have a more direct comparison to the data obtained in a one-dimensional optical lattice. The dashed green lines in Fig. 6.1 mark the positions at which we measure interaction dependent heating rates for linear shaking.

Figure 6.3 shows the measured heating rates at a red-detuned shaking frequency of $\omega_l = 2\pi \times 6\,\mathrm{kHz} \approx 0.6\,\omega_{10}$ for different driving strengths and scattering lengths. We assume that the loss mechanisms in the honeycomb lattice are similar to the one-dimensional lattice and therefore determine the experimental loss rates with the same fit function as introduced in section 4.3.3. One can clearly see that the measured heating rates in the honeycomb lattice are dramatically higher than in the one-dimensional lattice. We attribute this partly to an increased density of atoms on a single lattice site as the atoms are now stronger confined than in the one-dimensional lattice. This increased density enhances collision rates between atoms, which is already visible in the static lattice system. Whereas we had $1/e$ lifetimes of about 3-4 s in the one-dimensional lattice, the lifetime in the honeycomb lattice is reduced to about 1-2 s, depending on the scattering length of the condensate. Furthermore, as can be seen in Fig. 6.3 (a), the scaling with the driving strength α is only quadratic as indicated by the dashed red line. This can be explained by the

[3] Due to the geometry of the honeycomb lattice even linear shaking results in a modification of all tunneling matrix elements. In the case of red-detuned linear shaking, the tunneling matrix element along the shaking direction gets modified by a Bessel function according to $J_{\mathrm{eff}} = J_0 \mathcal{J}_0(\alpha) = J_0 \mathcal{J}_0(M d_H^2 \nu_0/\hbar)$. From simple geometric considerations, we find that the other two tunneling matrix elements are modulated by $J'_{\mathrm{eff}} = J_0 \mathcal{J}_0(\alpha/2)$. Similarly we find that the driving strength α for circular shaking is given by $\alpha = \sqrt{3} M d_H^2 \nu_0/(2\hbar)$.

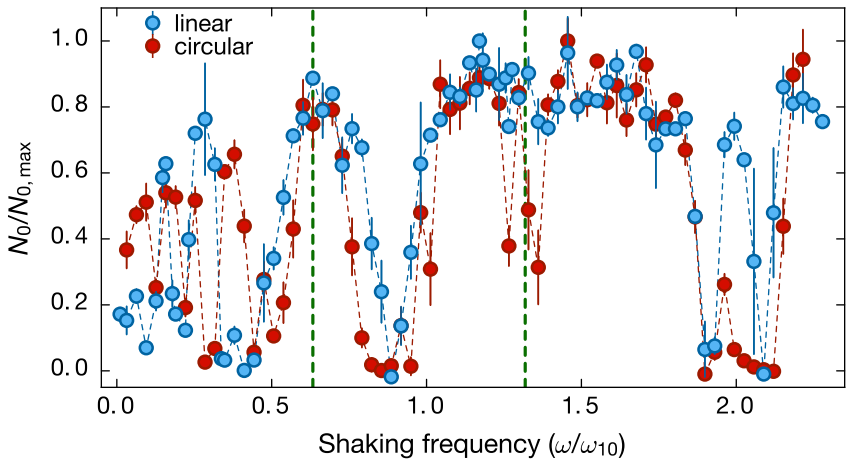

Figure 6.1: **Frequency scan in the honeycomb lattice.** Normalized atom number after a constant shaking duration of 300 ms with variable frequency at a shaking amplitude of $\nu_0 = 10\,\mathrm{kHz}$. In the case of linear shaking, this shaking amplitude results in a driving strength of $\alpha = 0.5$. For circular shaking, this shaking amplitude leads to a reduced driving strength of $\alpha \approx 0.43$. The blue data points show a frequency scan for linear shaking, where the frequency of only one lattice beam is modulated. The red data points show a frequency scan for circular shaking where two lattice beams are modulated out of phase. Both driving schemes show a large number of multiphoton resonances when the shaking frequency is smaller than ω_{10} and a wide frequency regime above ω_{10} where no multiphoton resonances can be observed. In the case of circular shaking additional resonances appear that are not present for linear shaking. The green dashed lines mark the positions at which we measure interaction-dependent heating rates for linear shaking.

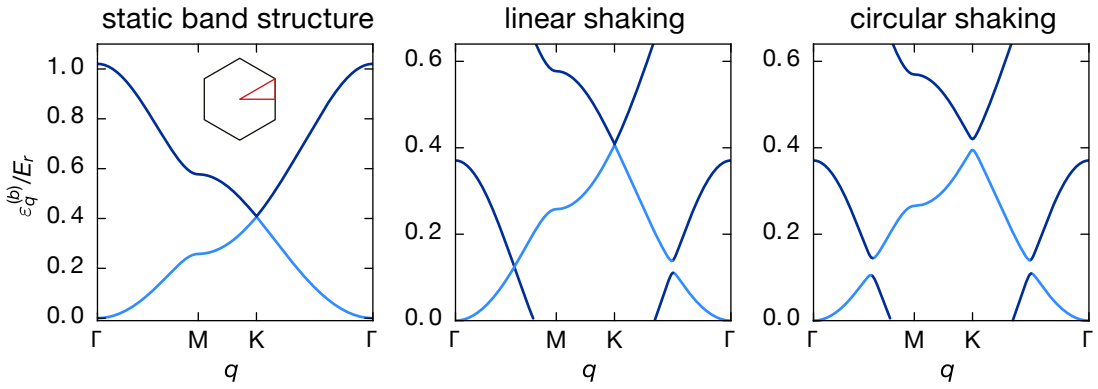

Figure 6.2: **Floquet band structure. Left:** Bandstructure of the lowest two bands of a honeycomb lattice with a lattice depth of $4\,E_r$ along the high symmetry path $\Gamma \to \mathrm{M} \to \mathrm{K} \to \Gamma$, see inset. **Center:** Floquet band structure of the lowest two bands for linear shaking with a driving frequency of $\omega = \omega_l = 2\pi \times 6\,\mathrm{kHz}$ and a shaking amplitude of $\nu_0 = 4.5\,\mathrm{kHz}$. Higher bands have been omitted for clarity reasons. The color coding is kept from the left figure to emphasize that the new Floquet bands are a mixture of both static bands. One can see a gap opening at the band crossing along the shaking direction. **Right:** Floquet band structure for the same shaking parameters as in the middle plot but for circular instead of linear driving. One can see a band gap opening at all band crossings including the Dirac points. This driving scheme yields a topological band structure [209, 210].

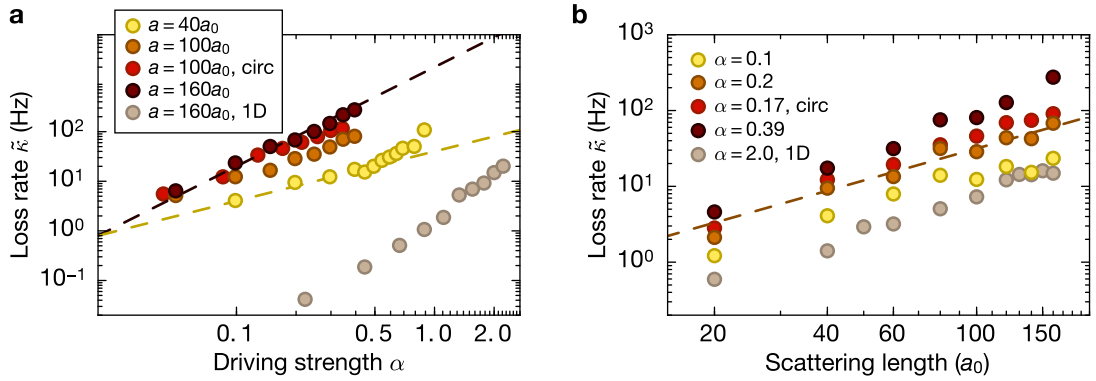

Figure 6.3: **Heating rates for red-detuned shaking. (a)** Effective loss rate $\tilde{\kappa}$ versus driving strength α. The gray data points show the measured data obtained in an 11 E_r deep one-dimensional lattice, see section 5.2.3. Note that these data points represent the strongest heating rates measured in the 1D lattice system! The heating rates obtained in a 4 E_r deep hexagonal lattice are dramatically higher than for the one-dimensional lattice and show a weaker scaling with α than the data obtained in the 1D lattice. The dashed yellow line is a guide to the eye and indicates a linear scaling with α, whereas the dashed dark red line is a guide to the eye which scales as α^2. The lighter red data points show heating rates obtained in a circularly shaken lattice and show slightly increased heating rates compared to the linear shaken case. **(b)** Heating rates versus scattering length. As for the 1D lattice, the heating rates scale as $a^{7/5}$, indicated by the dashed orange line, which is consistent with a Thomas-Fermi description of the condensate.

fact that apart from *intraband* scattering also single-photon scattering processes to the first excited band which scale with α^2 are allowed at this shaking frequency, which is slightly larger than the bandwidth of the lowest band. This property, that both *intraband* and *interband* scattering processes are available, could serve as an additional explanation for why the measured heating rates are dramatically higher compared to the one-dimensional lattice. The data for 40 a_0 even shows a linear scaling with α for driving strengths below $\alpha = 0.5$. This linear scaling might indicate that even coherent processes, like Rabi oscillations between two states that scale linearly with the driving strength, could play a role in the heating of the system.

We also measured heating rates for circular driving at this shaking frequency which showed comparable results to the linear case. For similar shaking parameters, the measured heating rates for circular shaking are slightly higher than for linear shaking. To keep Fig. 6.3 clear, we only plot one exemplary data set for circular shaking.

Figure 6.3 (b) shows the measured heating rates versus scattering length. The data

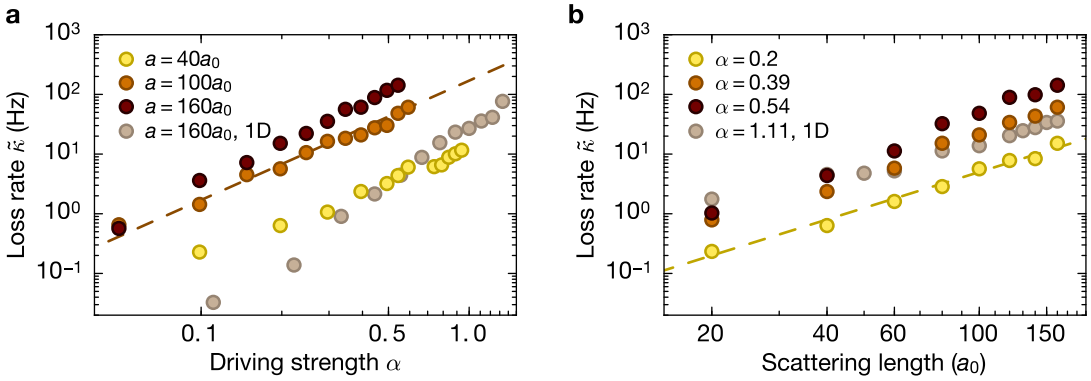

Figure 6.4: **Heating rates for blue-detuned shaking. (a)** Effective loss rate $\tilde{\kappa}$ versus driving strength α. Compared to the 1D lattice (gray data points) the loss rates are enhanced in the honeycomb lattice. The measured scaling of $\tilde{\kappa}$ is weaker than in a one-dimensional optical lattice. The orange dashed line is a guide to the eye with a scaling $\propto \alpha^2$. **(b)** When plotting the data versus the interaction between atoms one can see a stronger scaling than expected. The yellow dashed line indicates a quadratic scaling with the scattering length which is slightly stronger than the usual $a^{7/5}$ scaling observed before. This might suggest that the Thomas-Fermi approximation is not valid anymore in this driving regime.

is consistent with an $a^{7/5}$ scaling which was already obtained in the one-dimensional lattice. This scaling indicates that the measured heating rates are indeed interaction driven and not singe-particle like.

In a next step, we also determine heating rates for shaking frequencies above the band gap. This driving regime can also be employed to create topological band structures which was demonstrated in reference [68]. We choose a shaking frequency of $\omega_h = 2\pi \times 12.5\,\mathrm{kHz} \approx 1.3\,\omega_{10}$ indicated by the dashed green line in Fig. 6.1. As for the low-frequency case, the heating rates are dramatically increased compared to the 1D lattice as can be seen in Fig. 6.4. However, one can also see that the difference between the heating rates in the two different lattice structures is not as extreme anymore. Whereas heating rates were around three orders of magnitude larger for comparable shaking parameters for ω_l, the heating rates for the larger driving frequency ω_h are only two orders of magnitude larger than in the 1D case. This indicates that shaking with frequencies larger than the band gap might be favorable in the honeycomb lattice.

Like in the the low-frequency case, we find a weaker scaling with α than in the 1D lattice. The dashed orange line is a guide to the eye with a quadratic scaling indicating that single-photon processes are the dominant heating channel. Figure 6.4 (b) shows the measured heating rates versus the scattering length of the atoms. One can again observe a clear increase in the heating rates with scattering length. However,

the scaling is quadratic as indicated by the dashed yellow line, pointing out that the Thomas-Fermi approximation might not be valid anymore in this driving regime.

To conclude, the presented data in the honeycomb lattice shows dramatically increased heating rates compared to the one-dimensional lattice. To give an intuitive understanding of the measured loss rates let us look at the following example of an interacting condensate with a scattering length of $a = 160\,a_0$. For a shaking frequency of ω_h and after having ramped up the driving strength in 10 ms to its final value of $\alpha \simeq 0.5$, all atoms are lost within just 20 ms. This corresponds to only 250 shaking cycles. While it might be possible to conduct experiments with non-interacting atoms, the more interesting regime that combines periodic driving with strong interactions is, at least with the current setup, not accessible.

6.1.2 Next steps

While it might be possible to study shaking induced topological band structures with non-interacting particles, the interesting realm that combines strong interactions with topology will be inaccessible in the current setup. However, our study of heating rates was conducted in lattice systems that exhibit at least one weakly confined transverse direction. This weak transverse confinement enables the off-resonant absorption of energy from the drive, as excess energy can always be transferred in the transverse direction. By tightly confining atoms in a three-dimensional lattice all interaction induced heating channels discussed in this thesis should be forbidden or at least strongly suppressed. It is generally believed that a deep three-dimensional lattice structure should reduce the observed heating rates for shaking frequencies away from single-particle resonances as they were discussed in reference [119] and section 4.3.4. To this end, we started to build an additional lattice that tightly confines the atoms along the vertical direction. Future studies have to show whether this additional lattice can effectively reduce the heating rates as desired.

Another possibility to reduce heating rates could be to change to fermionic ^{40}K which is also present in our experimental setup [89]. As typical densities for degenerate Fermi gases are much lower than for condensates, and for a spin-polarized Fermi gas s-wave scattering events are forbidden by Pauli blocking, the heating channels discussed in this thesis should be strongly suppressed. Measurements presented in reference [68] show indeed only a moderate increase in the heating rates in the shaken lattice compared to the static case.

Despite the many disadvantages heating has on shaken lattice systems, it was recently shown that shaking induced heating can be utilized to measure the topology of a system [211]. This technique can be readily implemented in our system.

6.1.3 Future prospects

The additional lattice along the vertical direction will allow the tuning of its lattice spacing and will, therefore, facilitate the study of three-dimensional lattice structures as well as the study of single or coupled two-dimensional lattice systems and the study of strongly correlated phases. One paradigmatic example of such a strongly correlated phase is the interaction driven phase transition into a topological Mott insulator state in the honeycomb lattice [212]. Moreover, loading interacting atoms into the p-bands of the hexagonal lattice, which exhibit flat bands, enables the study of interesting and exotic many-body states as, for example, Wigner crystals [213–215]. In combination with artificial gauge fields, these flat bands become topological and enable the realization of fractional quantum Hall states [216–218]. These states exhibit quasiparticles with fractional charges [73] that neither obey bosonic nor fermionic exchange statistics and are therefore called anyons [219].

Furthermore, by properly tuning the vertical lattice potential, only two layers of it can be loaded with atoms. By coupling these two planes with each other, the system resembles that of bilayer graphene which exhibits different properties than monolayered graphene [220]. In particular, bilayered graphene exhibits even-denominator fractional quantum Hall states in the lowest Landau level [221, 222] where at least one of these states is expected to exhibit non-Abelian topological order [223]. Hence, this state exhibits non-Abelian anyons which are a key ingredient for the creation of fault-tolerant topological quantum computers [224].

Bibliography

[1] A. Stephenson, "Xx. on induced stability", Philosophical Magazine **15**, 233–236 (1908) (cit. on p. 1).

[2] P. L. Kapitza, "Dynamical stability of a pendulum when its point of suspension vibrates", Sov. Phys. JETP **21** (1951) https://doi.org/10.1016/B978-0-08-010973-2.50015-X (cit. on p. 1).

[3] D. H. Dunlap and V. M. Kenkre, "Dynamic localization of a charged particle moving under the influence of an electric field", Phys. Rev. B **34**, 3625 (1986) (cit. on pp. 1, 90).

[4] M. Holthaus, "Collapse of minibands in far-infrared irradiated superlattices", Phys. Rev. Lett. **69**, 351–354 (1992) (cit. on p. 1).

[5] X.-G. Zhao, "The suppression of a Bloch band in a driving laser field", Journal of Physics: Condensed Matter **6**, 2751 (1994) (cit. on p. 1).

[6] K. Drese and M. Holthaus, "Ultracold atoms in modulated standing light waves", Chemical Physics **217**, Dynamics of Driven Quantum Systems, 201 –219 (1997) (cit. on p. 1).

[7] T. Meier, G. von Plessen, P. Thomas, and S. W. Koch, "Coherent effects induced by static and time-dependent electric fields in semiconductors", Phys. Rev. B **51**, 14490–14497 (1995) (cit. on p. 1).

[8] B. J. Keay, S. Zeuner, S. J. Allen, K. D. Maranowski, A. C. Gossard, U. Bhattacharya, and M. J. W. Rodwell, "Dynamic Localization, Absolute Negative Conductance, and Stimulated, Multiphoton Emission in Sequential Resonant Tunneling Semiconductor Superlattices", Phys. Rev. Lett. **75**, 4102–4105 (1995) (cit. on p. 2).

[9] K. W. Madison, M. C. Fischer, R. B. Diener, Q. Niu, and M. G. Raizen, "Dynamical Bloch Band Suppression in an Optical Lattice", Phys. Rev. Lett. **81**, 5093–5096 (1998) (cit. on pp. 2, 34, 117).

[10] H. Lignier, C. Sias, D. Ciampini, Y. Singh, A. Zenesini, O. Morsch, and E. Arimondo, "Dynamical Control of Matter-Wave Tunneling in Periodic Potentials", Phys. Rev. Lett. **99**, 220403 (2007) (cit. on pp. 2, 26, 34, 73, 90, 117).

[11] A. Eckardt, M. Holthaus, H. Lignier, A. Zenesini, D. Ciampini, O. Morsch, and E. Arimondo, "Exploring dynamic localization with a Bose-Einstein condensate", Phys. Rev. A **79**, 013611 (2009) (cit. on pp. 2, 31, 73).

[12] I. Bloch, J. Dalibard, and W. Zwerger, "Many-body physics with ultracold gases", Rev. Mod. Phys. **80**, 885–964 (2008) (cit. on p. 2).

[13] I. Bloch, J. Dalibard, and S. Nascimbène, "Quantum simulations with ultracold quantum gases", Nat Phys **8**, 267–276 (2012) (cit. on p. 2).

[14] M. H. Anderson, J. R. Ensher, M. R. Matthews, C. E. Wieman, and E. A. Cornell, "Observation of Bose-Einstein Condensation in a Dilute Atomic Vapor", Science **269**, 198–201 (1995) (cit. on pp. 2, 7).

[15] K. B. Davis, M. O. Mewes, M. R. Andrews, N. J. van Druten, D. S. Durfee, D. M. Kurn, and W. Ketterle, "Bose-Einstein Condensation in a Gas of Sodium Atoms", Phys. Rev. Lett. **75**, 3969–3973 (1995) (cit. on pp. 2, 7, 46).

[16] C. C. Bradley, C. A. Sackett, J. J. Tollett, and R. G. Hulet, "Evidence of Bose-Einstein Condensation in an Atomic Gas with Attractive Interactions", Phys. Rev. Lett. **75**, 1687–1690 (1995) (cit. on p. 2).

[17] B. DeMarco and D. S. Jin, "Onset of Fermi Degeneracy in a Trapped Atomic Gas", Science **285**, 1703–1706 (1999) (cit. on p. 2).

[18] D. Jaksch, C. Bruder, J. I. Cirac, C. W. Gardiner, and P. Zoller, "Cold Bosonic Atoms in Optical Lattices", Phys. Rev. Lett. **81**, 3108–3111 (1998) (cit. on p. 2).

[19] J. Hubbard, "Electron correlations in narrow energy bands", Proceedings of the Royal Society of London A: Mathematical, Physical and Engineering Sciences **276**, 238–257 (1963) (cit. on p. 2).

[20] S. Inouye, M. R. Andrews, J. Stenger, H.-J. Miesner, D. M. Stamper-Kurn, and W. Ketterle, "Observation of Feshbach resonances in a Bose-Einstein condensate", Nature **392**, 151–154 (1998) (cit. on p. 2).

[21] M. Greiner, O. Mandel, T. Esslinger, T. W. Hänsch, and I. Bloch, "Quantum phase transition from a superfluid to a Mott insulator in a gas of ultracold atoms", Nature **415**, 39–44 (2002) (cit. on pp. 2, 56).

[22] L. Tarruell, D. Greif, T. Uehlinger, G. Jotzu, and T. Esslinger, "Creating, moving and merging Dirac points with a Fermi gas in a tunable honeycomb lattice", Nature **483**, 302–305 (2012) (cit. on p. 2).

[23] L. Duca, T. Li, M. Reitter, I. Bloch, M. Schleier-Smith, and U. Schneider, "An Aharonov-Bohm interferometer for determining Bloch band topology", Science **347**, 288–292 (2015) (cit. on pp. 2, 119).

[24] C. Becker, P. Soltan-Panahi, J. Kronjäger, S. Dörscher, K. Bongs, and K. Sengstock, "Ultracold quantum gases in triangular optical lattices", New Journal of Physics **12**, 065025 (2010) (cit. on p. 2).

[25] G. Wirth, M. Ölschläger, and A. Hemmerich, "Evidence for orbital superfluidity in the p-band of a bipartite optical square lattice", Nat Phys **7**, 147–153 (2011) (cit. on p. 2).

[26] G.-B. Jo, J. Guzman, C. K. Thomas, P. Hosur, A. Vishwanath, and D. M. Stamper-Kurn, "Ultracold Atoms in a Tunable Optical Kagome Lattice", Phys. Rev. Lett. **108**, 045305 (2012) (cit. on p. 2).

[27] C. Weitenberg, M. Endres, J. F. Sherson, M. Cheneau, P. Schauß, T. Fukuhara, I. Bloch, and S. Kuhr, "Single-spin addressing in an atomic Mott insulator", Nature **471**, 319–324 (2011) (cit. on p. 2).

[28] W. Ketterle, D. S. Durfee, and S. D. M. Kurn, "Making, probing and understanding Bose-Einstein condensates", in *Bose-einstein condensation in atomic gases (proceedings of the international school of physics "enrico fermi," course cxl)*, edited by M. Inguscio, S. Stringari, and C. E. Wieman (IOS Press, 1999) (cit. on pp. 2, 49).

[29] S. Fölling, F. Gerbier, A. Widera, O. Mandel, T. Gericke, and I. Bloch, "Spatial quantum noise interferometry in expanding ultracold atom clouds", Nature **434**, 481–484 (2005) (cit. on p. 2).

[30] T. Rom, T. Best, D. van Oosten, U. Schneider, S. Fölling, B. Paredes, and I. Bloch, "Free fermion antibunching in a degenerate atomic Fermi gas released from an optical lattice", Nature **444**, 733–736 (2006) (cit. on p. 2).

[31] W. S. Bakr, A. Peng, M. E. Tai, R. Ma, J. Simon, J. I. Gillen, S. Fölling, L. Pollet, and M. Greiner, "Probing the Superfluid–to–Mott Insulator Transition at the Single-Atom Level", Science **329**, 547–550 (2010) (cit. on pp. 2, 52).

[32] J. F. Sherson, C. Weitenberg, M. Endres, M. Cheneau, I. Bloch, and S. Kuhr, "Single-atom-resolved fluorescence imaging of an atomic Mott insulator", Nature **467**, 68–72 (2010) (cit. on pp. 2, 52).

[33] E. Haller, J. Hudson, A. Kelly, D. A. Cotta, B. Peaudecerf, G. D. Bruce, and S. Kuhr, "Single-atom imaging of fermions in a quantum-gas microscope", Nat Phys **11**, 738–742 (2015) (cit. on pp. 2, 52).

[34] M. F. Parsons, F. Huber, A. Mazurenko, C. S. Chiu, W. Setiawan, K. Wooley-Brown, S. Blatt, and M. Greiner, "Site-Resolved Imaging of Fermionic ^{6}Li in an Optical Lattice", Phys. Rev. Lett. **114**, 213002 (2015) (cit. on pp. 2, 52).

[35] A. Omran, M. Boll, T. A. Hilker, K. Kleinlein, G. Salomon, I. Bloch, and C. Gross, "Microscopic Observation of Pauli Blocking in Degenerate Fermionic Lattice Gases", Phys. Rev. Lett. **115**, 263001 (2015) (cit. on pp. 2, 52).

[36] G. J. A. Edge, R. Anderson, D. Jervis, D. C. McKay, R. Day, S. Trotzky, and J. H. Thywissen, "Imaging and addressing of individual fermionic atoms in an optical lattice", Phys. Rev. A **92**, 063406 (2015) (cit. on pp. 2, 52).

[37] L. W. Cheuk, M. A. Nichols, M. Okan, T. Gersdorf, V. V. Ramasesh, W. S. Bakr, T. Lompe, and M. W. Zwierlein, "Quantum-Gas Microscope for Fermionic Atoms", Phys. Rev. Lett. **114**, 193001 (2015) (cit. on pp. 2, 52).

[38] D. Greif, L. Tarruell, T. Uehlinger, R. Jördens, and T. Esslinger, "Probing Nearest-Neighbor Correlations of Ultracold Fermions in an Optical Lattice", Phys. Rev. Lett. **106**, 145302 (2011) (cit. on p. 2).

[39] J. Heinze, S. Götze, J. S. Krauser, B. Hundt, N. Fläschner, D.-S. Lühmann, C. Becker, and K. Sengstock, "Multiband Spectroscopy of Ultracold Fermions: Observation of Reduced Tunneling in Attractive Bose-Fermi Mixtures", Phys. Rev. Lett. **107**, 135303 (2011) (cit. on p. 3).

[40] C. Schori, T. Stöferle, H. Moritz, M. Köhl, and T. Esslinger, "Excitations of a Superfluid in a Three-Dimensional Optical Lattice", Phys. Rev. Lett. **93**, 240402 (2004) (cit. on p. 3).

[41] T. Stöferle, H. Moritz, C. Schori, M. Köhl, and T. Esslinger, "Transition from a Strongly Interacting 1D Superfluid to a Mott Insulator", Phys. Rev. Lett. **92**, 130403 (2004) (cit. on p. 3).

[42] R. Ma, M. E. Tai, P. M. Preiss, W. S. Bakr, J. Simon, and M. Greiner, "Photon-Assisted Tunneling in a Biased Strongly Correlated Bose Gas", Phys. Rev. Lett. **107**, 095301 (2011) (cit. on p. 3).

[43] W. S. Bakr, P. M. Preiss, M. E. Tai, R. Ma, J. Simon, and M. Greiner, "Orbital excitation blockade and algorithmic cooling in quantum gases", Nature **480**, 500–503 (2011) (cit. on p. 3).

[44] N. Gemelke, E. Sarajlic, Y. Bidel, S. Hong, and S. Chu, "Parametric Amplification of Matter Waves in Periodically Translated Optical Lattices", Phys. Rev. Lett. **95**, 170404 (2005) (cit. on pp. 3, 34, 36, 117).

[45] C. V. Parker, L.-C. Ha, and C. Chin, "Direct observation of effective ferromagnetic domains of cold atoms in a shaken optical lattice", Nat Phys **9**, 769–774 (2013) (cit. on pp. 3, 36, 73, 90, 118).

[46] L.-C. Ha, L. W. Clark, C. V. Parker, B. M. Anderson, and C. Chin, "Roton-Maxon Excitation Spectrum of Bose Condensates in a Shaken Optical Lattice", Phys. Rev. Lett. **114**, 055301 (2015) (cit. on pp. 3, 36, 90).

[47] A. Eckardt, C. Weiss, and M. Holthaus, "Superfluid-Insulator Transition in a Periodically Driven Optical Lattice", Phys. Rev. Lett. **95**, 260404 (2005) (cit. on pp. 3, 34).

[48] A. Zenesini, H. Lignier, D. Ciampini, O. Morsch, and E. Arimondo, "Coherent Control of Dressed Matter Waves", Phys. Rev. Lett. **102**, 100403 (2009) (cit. on pp. 3, 26, 34, 117).

[49] K. v. Klitzing, G. Dorda, and M. Pepper, "New Method for High-Accuracy Determination of the Fine-Structure Constant Based on Quantized Hall Resistance", Phys. Rev. Lett. **45**, 494–497 (1980) (cit. on p. 3).

[50] R. Peierls, "Zur Theorie des Diamagnetismus von Leitungselektronen", Zeitschrift für Physik **80**, 763–791 (1933) (cit. on p. 3).

[51] J. M. Luttinger, "The Effect of a Magnetic Field on Electrons in a Periodic Potential", Phys. Rev. **84**, 814–817 (1951) (cit. on p. 3).

[52] P. Hauke, O. Tieleman, A. Celi, C. Ölschläger, J. Simonet, J. Struck, M. Weinberg, P. Windpassinger, K. Sengstock, M. Lewenstein, and A. Eckardt, "Non-Abelian Gauge Fields and Topological Insulators in Shaken Optical Lattices", Phys. Rev. Lett. **109**, 145301 (2012) (cit. on pp. 3, 119).

[53] J. Struck, C. Ölschläger, M. Weinberg, P. Hauke, J. Simonet, A. Eckardt, M. Lewenstein, K. Sengstock, and P. Windpassinger, "Tunable Gauge Potential for Neutral and Spinless Particles in Driven Optical Lattices", Phys. Rev. Lett. **108**, 225304 (2012) (cit. on pp. 3, 26, 34).

[54] J. Struck, M. Weinberg, C. Ölschläger, P. Windpassinger, J. Simonet, K. Sengstock, R. Hoppner, P. Hauke, A. Eckardt, M. Lewenstein, and L. Mathey, "Engineering Ising-XY spin-models in a triangular lattice using tunable artificial gauge fields", Nat Phys **9**, 738–743 (2013) (cit. on pp. 3, 26, 34).

[55] M. Aidelsburger, M. Atala, S. Nascimbène, S. Trotzky, Y.-A. Chen, and I. Bloch, "Experimental Realization of Strong Effective Magnetic Fields in an Optical Lattice", Phys. Rev. Lett. **107**, 255301 (2011) (cit. on pp. 3, 26, 34).

[56] K. Jiménez-García, L. J. LeBlanc, R. A. Williams, M. C. Beeler, A. R. Perry, and I. B. Spielman, "Peierls Substitution in an Engineered Lattice Potential", Phys. Rev. Lett. **108**, 225303 (2012) (cit. on p. 3).

[57] M. Aidelsburger, M. Atala, S. Nascimbène, S. Trotzky, Y.-A. Chen, and I. Bloch, "Experimental realization of strong effective magnetic fields in optical superlattice potentials", Applied Physics B **113**, 1–11 (2013) (cit. on p. 3).

[58] M. Aidelsburger, M. Atala, M. Lohse, J. T. Barreiro, B. Paredes, and I. Bloch, "Realization of the Hofstadter Hamiltonian with Ultracold Atoms in Optical Lattices", Phys. Rev. Lett. **111**, 185301 (2013) (cit. on pp. 3, 26, 34, 73).

[59] M. Atala, M. Aidelsburger, M. Lohse, J. T. Barreiro, B. Paredes, and I. Bloch, "Observation of chiral currents with ultracold atoms in bosonic ladders", Nat Phys **10**, 588–593 (2014) (cit. on pp. 3, 26, 34).

[60] M. Aidelsburger, M. Lohse, C. Schweizer, M. Atala, J. T. Barreiro, S. Nascimbène, N. R. Cooper, I. Bloch, and N. Goldman, "Measuring the Chern number of Hofstadter bands with ultracold bosonic atoms", Nat Phys **11**, 162–166 (2015) (cit. on pp. 3, 26, 34, 73, 119).

[61] H. Miyake, G. A. Siviloglou, C. J. Kennedy, W. C. Burton, and W. Ketterle, "Realizing the Harper Hamiltonian with Laser-Assisted Tunneling in Optical Lattices", Phys. Rev. Lett. **111**, 185302 (2013) (cit. on pp. 3, 26, 34, 73).

[62] C. J. Kennedy, W. C. Burton, W. C. Chung, and W. Ketterle, "Observation of Bose-Einstein condensation in a strong synthetic magnetic field", Nat Phys **11**, 859–864 (2015) (cit. on pp. 3, 26, 34).

[63] N. Goldman and J. Dalibard, "Periodically Driven Quantum Systems: Effective Hamiltonians and Engineered Gauge Fields", Phys. Rev. X **4**, 031027 (2014) (cit. on pp. 3, 28, 78).

[64] W. Zheng and H. Zhai, "Floquet topological states in shaking optical lattices", Phys. Rev. A **89**, 061603 (2014) (cit. on p. 3).

[65] A. S. Sørensen, E. Demler, and M. D. Lukin, "Fractional Quantum Hall States of Atoms in Optical Lattices", Phys. Rev. Lett. **94**, 086803 (2005) (cit. on p. 3).

[66] N. Goldman, J. C. Budich, and P. Zoller, "Topological quantum matter with ultracold gases in optical lattices", Nat Phys **12**, 639–645 (2016) (cit. on p. 3).

[67] T. Kitagawa, E. Berg, M. Rudner, and E. Demler, "Topological characterization of periodically driven quantum systems", Phys. Rev. B **82**, 235114 (2010) (cit. on p. 3).

[68] G. Jotzu, M. Messer, R. Desbuquois, M. Lebrat, T. Uehlinger, D. Greif, and T. Esslinger, "Experimental realization of the topological Haldane model with ultracold fermions", Nature **515**, 237–240 (2014) (cit. on pp. 4, 26, 34, 73, 117, 119, 124, 125).

[69] N. Fläschner, D. Vogel, M. Tarnowski, B. S. Rem, D.-S. Lühmann, M. Heyl, J. C. Budich, L. Mathey, K. Sengstock, and C. Weitenberg, "Observation of a dynamical topological phase transition", ArXiv e-prints (2016) (cit. on pp. 4, 117).

[70] F. D. M. Haldane, "Model for a Quantum Hall Effect without Landau Levels: Condensed-Matter Realization of the "Parity Anomaly"", Phys. Rev. Lett. **61**, 2015–2018 (1988) (cit. on pp. 4, 119).

[71] A. Lazarides, A. Das, and R. Moessner, "Equilibrium states of generic quantum systems subject to periodic driving", Phys. Rev. E **90**, 012110 (2014) (cit. on pp. 4, 73).

[72] L. D'Alessio and M. Rigol, "Long-time Behavior of Isolated Periodically Driven Interacting Lattice Systems", Phys. Rev. X **4**, 041048 (2014) (cit. on pp. 4, 73).

[73] R. B. Laughlin, "Anomalous Quantum Hall Effect: An Incompressible Quantum Fluid with Fractionally Charged Excitations", Phys. Rev. Lett. **50**, 1395–1398 (1983) (cit. on pp. 4, 126).

[74] S. Choudhury and E. J. Mueller, "Stability of a Floquet Bose-Einstein condensate in a one-dimensional optical lattice", Phys. Rev. A **90**, 013621 (2014) (cit. on pp. 4, 73, 74).

[75] S. Choudhury and E. J. Mueller, "Transverse collisional instabilities of a Bose-Einstein condensate in a driven one-dimensional lattice", Phys. Rev. A **91**, 023624 (2015) (cit. on pp. 4, 73, 74).

[76] S. Choudhury and E. J. Mueller, "Stability of a Bose-Einstein condensate in a driven optical lattice: Crossover between weak and tight transverse confinement", Phys. Rev. A **92**, 063639 (2015) (cit. on pp. 4, 73, 74, 118).

[77] T. Bilitewski and N. R. Cooper, "Scattering theory for Floquet-Bloch states", Phys. Rev. A **91**, 033601 (2015) (cit. on pp. 4, 73, 74, 118).

[78] T. Bilitewski and N. R. Cooper, "Population dynamics in a Floquet realization of the Harper-Hofstadter Hamiltonian", Phys. Rev. A **91**, 063611 (2015) (cit. on pp. 4, 73, 74).

[79] Bose, "Plancks Gesetz und Lichtquantenhypothese", Zeitschrift für Physik **26**, 178–181 (1924) (cit. on p. 7).

[80] A. Einstein, "Quantentheorie des einatomigen idealen Gases", Sitzungsberichte der Preußischen Akademie der Wissenschaften **Physikalisch-mathematische Klasse**, 261–267 (1924) (cit. on p. 7).

[81] L. Pitaevskii and S. Stringari, *Bose-Einstein Condensation*, International Series of Monographs on Physics (Clarendon Press, 2003) (cit. on pp. 7, 10).

[82] D. Griffiths, *Introduction to Quantum Mechanics*, Pearson international edition (Pearson Prentice Hall, 2005) (cit. on pp. 8, 21).

[83] S. R. de Groot, G. J. Hooyman, and C. A. ten Seldam, "On the Bose-Einstein Condensation", Proceedings of the Royal Society of London A: Mathematical, Physical and Engineering Sciences **203**, 266–286 (1950) (cit. on p. 8).

[84] F. Dalfovo, S. Giorgini, L. P. Pitaevskii, and S. Stringari, "Theory of Bose-Einstein condensation in trapped gases", Rev. Mod. Phys. **71**, 463–512 (1999) (cit. on pp. 9, 11).

[85] J. Dalibard, "Collisional dynamics of ultra-cold atomic gases", in Proceedings of the International School of Physics "Enrico Fermi", edited by M. Inguscio, S. Stringari, and C. Wieman (1998) (cit. on pp. 10, 113).

[86] J. Weiner, V. S. Bagnato, S. Zilio, and P. S. Julienne, "Experiments and theory in cold and ultracold collisions", Rev. Mod. Phys. **71**, 1–85 (1999) (cit. on p. 10).

[87] C. Pethick and H. Smith, *Bose-Einstein Condensation in Dilute Gases* (Cambridge University Press, 2002) (cit. on pp. 10, 16).

[88] N. Ashcroft and N. Mermin, *Solid State Physics* (Cengage Learning, 2011) (cit. on pp. 13, 15).

[89] L. Duca, "Probing topological properties of Bloch bands with ultracold atoms in a honeycomb optical lattice", PhD thesis (Ludwig-Maximilians-Universität München, 2015) (cit. on pp. 18, 42, 44, 46, 51, 59, 119, 125).

[90] T. Li, "Probing Bloch band geometry with ultracold atoms in optical lattices", PhD thesis (Ludwig-Maximilians-Universität München, 2016) (cit. on pp. 18, 42, 44, 119).

[91] C. Kittel, *Introduction to Solid State Physics* (Wiley, 2004) (cit. on p. 18).

[92] K. I. Petsas, A. B. Coates, and G. Grynberg, "Crystallography of optical lattices", Phys. Rev. A **50**, 5173–5189 (1994) (cit. on p. 19).

[93] A. H. Castro Neto, F. Guinea, N. M. R. Peres, K. S. Novoselov, and A. K. Geim, "The electronic properties of graphene", Rev. Mod. Phys. **81**, 109–162 (2009) (cit. on p. 20).

[94] B. Bernevig and T. Hughes, *Topological Insulators and Topological Superconductors* (Princeton University Press, 2013) (cit. on p. 21).

[95] J. L. Mañes, F. Guinea, and M. A. H. Vozmediano, "Existence and topological stability of Fermi points in multilayered graphene", Phys. Rev. B **75**, 155424 (2007) (cit. on p. 21).

[96] A. Eckardt, "Colloquium: Atomic quantum gases in periodically driven optical lattices", Rev. Mod. Phys. **89**, 011004 (2017) (cit. on pp. 21, 24).

[97] G. Floquet, "Sur les équations différentielles linéaires à coefficients périodiques", Annales scientifiques de l'cole Normale Suprieure **12**, 47–88 (1883) (cit. on p. 21).

[98] J. H. Shirley, "Solution of the Schrödinger Equation with a Hamiltonian Periodic in Time", Phys. Rev. **138**, B979–B987 (1965) (cit. on pp. 21, 25).

[99] S. H. Autler and C. H. Townes, "Stark Effect in Rapidly Varying Fields", Phys. Rev. **100**, 703–722 (1955) (cit. on p. 21).

[100] H. Sambe, "Steady States and Quasienergies of a Quantum-Mechanical System in an Oscillating Field", Phys. Rev. A **7**, 2203–2213 (1973) (cit. on p. 22).

[101] C. Cohen-Tannoudji, J. Dupont-Roc, and G. Grynberg, *Atom-Photon Interactions: Basic Processes and Applications*, A Wiley-Interscience publication (Wiley, 1998) (cit. on p. 24).

[102] J. Struck, C. Ölschläger, R. Le Targat, P. Soltan-Panahi, A. Eckardt, M. Lewenstein, P. Windpassinger, and K. Sengstock, "Quantum Simulation of Frustrated Classical Magnetism in Triangular Optical Lattices", Science **333**, 996–999 (2011) (cit. on p. 26).

[103] M. E. Tai, A. Lukin, M. Rispoli, R. Schittko, T. Menke, D. Borgnia, P. M. Preiss, F. Grusdt, A. M. Kaufman, and M. Greiner, "Microscopy of the interacting Harper-Hofstadter model in the few-body limit", ArXiv e-prints (2016) (cit. on pp. 26, 34).

[104] N. Fläschner, B. S. Rem, M. Tarnowski, D. Vogel, D.-S. Lühmann, K. Sengstock, and C. Weitenberg, "Experimental reconstruction of the Berry curvature in a Floquet Bloch band", Science **352**, 1091–1094 (2016) (cit. on pp. 26, 34, 119).

[105] M. Lohse, C. Schweizer, O. Zilberberg, M. Aidelsburger, and I. Bloch, "A Thouless quantum pump with ultracold bosonic atoms in an optical superlattice", Nat Phys **12**, 350–354 (2016) (cit. on pp. 26, 34, 119).

[106] M. Lohse, C. Schweizer, H. M. Price, O. Zilberberg, and I. Bloch, "Exploring 4D Quantum Hall Physics with a 2D Topological Charge Pump", ArXiv e-prints (2017) (cit. on pp. 26, 34, 119).

[107] S. Arlinghaus and M. Holthaus, "Driven optical lattices as strong-field simulators", Phys. Rev. A **81**, 063612 (2010) (cit. on pp. 27, 32).

[108] D. Sarason, *Complex Function Theory* (American Mathematical Soc.) (cit. on p. 28).

[109] C. Moler and C. V. Loan, "Nineteen Dubious Ways to Compute the Exponential of a Matrix, Twenty-Five Years Later", SIAM Review **45**, 3–49 (2003) (cit. on p. 28).

[110] A. M. Davie and A. J. Stothers, "Improved bound for complexity of matrix multiplication", Proceedings of the Royal Society of Edinburgh: Section A Mathematics **143**, 351369 (2013) (cit. on p. 28).

[111] T. P. Grozdanov and M. J. Raković, "Quantum system driven by rapidly varying periodic perturbation", Phys. Rev. A **38**, 1739–1746 (1988) (cit. on p. 28).

[112] S. Rahav, I. Gilary, and S. Fishman, "Effective Hamiltonians for periodically driven systems", Phys. Rev. A **68**, 013820 (2003) (cit. on p. 28).

[113] A. Eckardt and E. Anisimovas, "High-frequency approximation for periodically driven quantum systems from a Floquet-space perspective", New Journal of Physics **17**, 093039 (2015) (cit. on pp. 28, 73, 78).

[114] M. M. Maricq, "Application of average Hamiltonian theory to the NMR of solids", Phys. Rev. B **25**, 6622–6632 (1982) (cit. on p. 29).

[115] K. F. Milfeld and R. E. Wyatt, "Study, extension, and application of Floquet theory for quantum molecular systems in an oscillating field", Phys. Rev. A **27**, 72–94 (1983) (cit. on p. 29).

[116] F Casas, J. A. Oteo, and J Ros, "Floquet theory: exponential perturbative treatment", Journal of Physics A: Mathematical and General **34**, 3379 (2001) (cit. on p. 29).

[117] C. Heinisch and M. Holthaus, "Adiabatic preparation of Floquet condensates", Journal of Modern Optics **63**, 1768–1776 (2016) (cit. on p. 31).

[118] W. V. Houston, "Acceleration of Electrons in a Crystal Lattice", Phys. Rev. **57**, 184–186 (1940) (cit. on p. 31).

[119] M. Weinberg, C. Ölschläger, C. Sträter, S. Prelle, A. Eckardt, K. Sengstock, and J. Simonet, "Multiphoton interband excitations of quantum gases in driven optical lattices", Phys. Rev. A **92**, 043621 (2015) (cit. on pp. 32, 74, 87, 89, 125).

[120] S. Haroche, C. Cohen-Tannoudji, C. Audoin, and J. P. Schermann, "Modified Zeeman Hyperfine Spectra Observed in H^1 and Rb^{87} Ground States Interacting with a Nonresonant rf Field", Phys. Rev. Lett. **24**, 861–864 (1970) (cit. on p. 34).

[121] R. Grimm, M. Weidemüller, and Y. B. Ovchinnikov, "Optical Dipole Traps for Neutral Atoms", Advances in Atomic Molecular and Optical Physics **42**, 95–170 (2000) (cit. on p. 38).

[122] L. Allen and J. Eberly, *Optical Resonance and Two-level Atoms*, Dover books on physics and chemistry (Dover, 1975) (cit. on p. 38).

[123] U. Schneider, "Interacting Fermionic Atoms in Optical Lattices - A Quantum Simulator for Condensed Matter Physics ", PhD thesis (Johannes Gutenberg Universität Mainz, 2010) (cit. on p. 41).

[124] M. Reitter, "Ultracold Fermions in a novel 2D setup", Master's thesis (Ludwig-Maximilians-Universität München, 2012) (cit. on pp. 41, 44).

[125] U. Schneider, L. Hackermüller, J. P. Ronzheimer, S. Will, S. Braun, T. Best, I. Bloch, E. Demler, S. Mandt, D. Rasch, and A. Rosch, "Fermionic transport and out-of-equilibrium dynamics in a homogeneous Hubbard model with ultracold atoms", Nat Phys **8**, 213–218 (2012) (cit. on p. 41).

[126] J. P. Ronzheimer, M. Schreiber, S. Braun, S. S. Hodgman, S. Langer, I. P. McCulloch, F. Heidrich-Meisner, I. Bloch, and U. Schneider, "Expansion Dynamics of Interacting Bosons in Homogeneous Lattices in One and Two Dimensions", Phys. Rev. Lett. **110**, 205301 (2013) (cit. on p. 41).

[127] T. Li, "An apparatus for probing fermions in a quasi-two-dimensional geometry", Master's thesis (Ludwig-Maximilians-Universität München, 2011) (cit. on p. 44).

[128] M. Boll, "A $2D^+$-3D MOT system for producing laser-cooled K-Rb mixtures", Master's thesis (Johannes Gutenberg Universität Mainz, 2011) (cit. on p. 44).

[129] K. Dieckmann, R. J. C. Spreeuw, M. Weidemüller, and J. T. M. Walraven, "Two-dimensional magneto-optical trap as a source of slow atoms", Phys. Rev. A **58**, 3891–3895 (1998) (cit. on p. 44).

[130] J. Catani, P. Maioli, L. De Sarlo, F. Minardi, and M. Inguscio, "Intense slow beams of bosonic potassium isotopes", Phys. Rev. A **73**, 033415 (2006) (cit. on p. 44).

[131] S. Ospelkaus-Schwarzer, "Quantum Degenerate Fermi-Bose Mixtures of ^{40}K and ^{87}Rb in 3D Optical Lattices", PhD thesis (Universität Hamburg, 2006) (cit. on p. 44).

[132] H. J. Metcalf and P. van der Straten, *Laser Cooling and Trapping* (Springer, 2.edition, 2002) (cit. on pp. 44, 65).

[133] W. Petrich, M. H. Anderson, J. R. Ensher, and E. A. Cornell, "Behavior of atoms in a compressed magneto-optical trap", J. Opt. Soc. Am. B **11**, 1332–1335 (1994) (cit. on p. 44).

[134] C. Fort, A. Bambini, L. Cacciapuoti, F. Cataliotti, M. Prevedelli, G. Tino, and M. Inguscio, "Cooling mechanisms in potassium magneto-optical traps", The European Physical Journal D - Atomic, Molecular, Optical and Plasma Physics **3**, 113–118 (1998) (cit. on p. 44).

[135] V. Gokhroo, G Rajalakshmi, R. K. Easwaran, and C. S. Unnikrishnan, "Sub-Doppler deep-cooled bosonic and fermionic isotopes of potassium in a compact 2D + 3D MOT set-up", Journal of Physics B: Atomic, Molecular and Optical Physics **44**, 115307 (2011) (cit. on p. 44).

[136] M. Landini, S. Roy, L. Carcagní, D. Trypogeorgos, M. Fattori, M. Inguscio, and G. Modugno, "Sub-Doppler laser cooling of potassium atoms", Phys. Rev. A **84**, 043432 (2011) (cit. on p. 44).

[137] G. Salomon, L. Fouch, P. Wang, A. Aspect, P. Bouyer, and T. Bourdel, "Gray-molasses cooling of 39 K to a high phase-space density", EPL **104**, 63002 (2013) (cit. on p. 45).

[138] D. A. Steck, *Rubidium 87 D Line Data*, available online at `http://steck.us/alkalidata` (revision 2.1.5, 13 January 2015) (cit. on pp. 45, 52, 54).

[139] T. G. Tiecke, *Properties of Potassium*, available online at `http://tobiastiecke.nl/archive/PotassiumProperties.pdf`, 2011 (cit. on pp. 45, 52).

[140] A. L. Migdall, J. V. Prodan, W. D. Phillips, T. H. Bergeman, and H. J. Metcalf, "First Observation of Magnetically Trapped Neutral Atoms", Phys. Rev. Lett. **54**, 2596–2599 (1985) (cit. on p. 45).

[141] M. Greiner, I. Bloch, T. W. Hänsch, and T. Esslinger, "Magnetic transport of trapped cold atoms over a large distance", Phys. Rev. A **63**, 031401 (2001) (cit. on p. 46).

[142] E. Majorana, "Atomi orientati in campo magnetico variabile", Nuovo Cimento **9**, 43 (1932) (cit. on p. 46).

[143] L. De Sarlo, P. Maioli, G. Barontini, J. Catani, F. Minardi, and M. Inguscio, "Collisional properties of sympathetically cooled ^{39}K", Phys. Rev. A **75**, 022715 (2007) (cit. on p. 46).

[144] F. Ferlaino, C. D'Errico, G. Roati, M. Zaccanti, M. Inguscio, G. Modugno, and A. Simoni, "Feshbach spectroscopy of a K−Rb atomic mixture", Phys. Rev. A **73**, 040702 (2006) (cit. on p. 47).

[145] C. D'Errico, M. Zaccanti, M. Fattori, G. Roati, M. Inguscio, G. Modugno, and A. Simoni, "Feshbach resonances in ultracold ^{39}K", New Journal of Physics **9**, 223 (2007) (cit. on p. 47).

[146] D. S. Jin, J. R. Ensher, M. R. Matthews, C. E. Wieman, and E. A. Cornell, "Collective Excitations of a Bose-Einstein Condensate in a Dilute Gas", Phys. Rev. Lett. **77**, 420–423 (1996) (cit. on p. 47).

[147] M.-O. Mewes, M. R. Andrews, N. J. van Druten, D. M. Kurn, D. S. Durfee, C. G. Townsend, and W. Ketterle, "Collective Excitations of a Bose-Einstein Condensate in a Magnetic Trap", Phys. Rev. Lett. **77**, 988–991 (1996) (cit. on p. 47).

[148] E. Timmermans, P. Tommasini, M. Hussein, and A. Kerman, "Feshbach resonances in atomic BoseEinstein condensates", Physics Reports **315**, 199 –230 (1999) (cit. on p. 47).

[149] C. Chin, R. Grimm, P. Julienne, and E. Tiesinga, "Feshbach resonances in ultracold gases", Rev. Mod. Phys. **82**, 1225–1286 (2010) (cit. on p. 47).

[150] T. Köhler, K. Góral, and P. S. Julienne, "Production of cold molecules via magnetically tunable Feshbach resonances", Rev. Mod. Phys. **78**, 1311–1361 (2006) (cit. on p. 49).

[151] H. Feshbach, "Unified theory of nuclear reactions", Annals of Physics **5**, 357 –390 (1958) (cit. on p. 49).

[152] U. Fano, "Effects of Configuration Interaction on Intensities and Phase Shifts", Phys. Rev. **124**, 1866–1878 (1961) (cit. on p. 49).

[153] A. J. Moerdijk, B. J. Verhaar, and A. Axelsson, "Resonances in ultracold collisions of ^{6}Li, ^{7}Li, and ^{23}Na", Phys. Rev. A **51**, 4852–4861 (1995) (cit. on p. 49).

[154] H. Haken and H. Wolf, *The physics of atoms and quanta: introduction to experiments and theory* (Springer-Verlag, 1994) (cit. on p. 50).

[155] G. Reinaudi, T. Lahaye, Z. Wang, and D. Guéry-Odelin, "Strong saturation absorption imaging of dense clouds of ultracold atoms", Opt. Lett. **32**, 3143–3145 (2007) (cit. on p. 50).

[156] C. Hofrichter, "Probing the SU(N) Fermi-Hubbard model with ytterbium atoms in an optical lattice", PhD thesis (Ludwig-Maximilians-Universität München, 2016) (cit. on p. 51).

[157] U. Schneider, L. Hackermüller, S. Will, T. Best, I. Bloch, T. A. Costi, R. W. Helmes, D. Rasch, and A. Rosch, "Metallic and Insulating Phases of Repulsively Interacting Fermions in a 3D Optical Lattice", Science **322**, 1520–1525 (2008) (cit. on p. 52).

[158] N. Gemelke, X. Zhang, C.-L. Hung, and C. Chin, "In situ observation of incompressible Mott-insulating domains in ultracold atomic gases", Nature **460**, 995–998 (2009) (cit. on p. 52).

[159] M. Endres, M. Cheneau, T. Fukuhara, C. Weitenberg, P. Schauß, C. Gross, L. Mazza, M. C. Bañuls, L. Pollet, I. Bloch, and S. Kuhr, "Observation of Correlated Particle-Hole Pairs and String Order in Low-Dimensional Mott Insulators", Science **334**, 200–203 (2011) (cit. on p. 52).

[160] M. Cheneau, P. Barmettler, D. Poletti, M. Endres, P. Schauß, T. Fukuhara, C. Gross, I. Bloch, C. Kollath, and S. Kuhr, "Light-cone-like spreading of correlations in a quantum many-body system", Nature **481**, 484–487 (2012) (cit. on p. 52).

[161] C.-L. Hung, X. Zhang, L.-C. Ha, S.-K. Tung, N. Gemelke, and C. Chin, "Extracting densitydensity correlations from in situ images of atomic quantum gases", New Journal of Physics **13**, 075019 (2011) (cit. on p. 52).

[162] C.-L. Hung, X. Zhang, N. Gemelke, and C. Chin, "Observation of scale invariance and universality in two-dimensional Bose gases", Nature **470**, 236–239 (2011) (cit. on p. 52).

[163] T. Yefsah, R. Desbuquois, L. Chomaz, K. J. Günter, and J. Dalibard, "Exploring the Thermodynamics of a Two-Dimensional Bose Gas", Phys. Rev. Lett. **107**, 130401 (2011) (cit. on p. 52).

[164] X. Zhang, C.-L. Hung, S.-K. Tung, and C. Chin, "Observation of Quantum Criticality with Ultracold Atoms in Optical Lattices", Science **335**, 1070–1072 (2012) (cit. on p. 52).

[165] K. D. Nelson, X. Li, and D. S. Weiss, "Imaging single atoms in a three-dimensional array", Nat Phys **3**, 556–560 (2007) (cit. on p. 52).

[166] G. Breit and I. I. Rabi, "Measurement of Nuclear Spin", Phys. Rev. **38**, 2082–2083 (1931) (cit. on p. 54).

[167] F. Gerbier, A. Widera, S. Fölling, O. Mandel, T. Gericke, and I. Bloch, "Interference pattern and visibility of a Mott insulator", Phys. Rev. A **72**, 053606 (2005) (cit. on p. 56).

[168] M. Greiner, "Ultracold quantum gases in three-dimensional optical lattice potentials", PhD thesis (Ludwig-Maximilians-Universität München, 2003) (cit. on p. 56).

[169] F. Gerbier, S. Trotzky, S. Fölling, U. Schnorrberger, J. D. Thompson, A. Widera, I. Bloch, L. Pollet, M. Troyer, B. Capogrosso-Sansone, N. V. Prokof'ev, and B. V. Svistunov, "Expansion of a Quantum Gas Released from an Optical Lattice", Phys. Rev. Lett. **101**, 155303 (2008) (cit. on p. 56).

[170] M. Greiner, I. Bloch, O. Mandel, T. W. Hänsch, and T. Esslinger, "Exploring Phase Coherence in a 2D Lattice of Bose-Einstein Condensates", Phys. Rev. Lett. **87**, 160405 (2001) (cit. on pp. 56, 57).

[171] F. Gerbier, A. Widera, S. Fölling, O. Mandel, T. Gericke, and I. Bloch, "Phase Coherence of an Atomic Mott Insulator", Phys. Rev. Lett. **95**, 050404 (2005) (cit. on p. 56).

[172] S. Braun, M. Friesdorf, S. S. Hodgman, M. Schreiber, J. P. Ronzheimer, A. Riera, M. del Rey, I. Bloch, J. Eisert, and U. Schneider, "Emergence of coherence and the dynamics of quantum phase transitions", Proceedings of the National Academy of Sciences **112**, 3641–3646 (2015) (cit. on p. 56).

[173] A. Kastberg, W. D. Phillips, S. L. Rolston, R. J. C. Spreeuw, and P. S. Jessen, "Adiabatic Cooling of Cesium to 700 nK in an Optical Lattice", Phys. Rev. Lett. **74**, 1542–1545 (1995) (cit. on p. 57).

[174] M. Ben Dahan, E. Peik, J. Reichel, Y. Castin, and C. Salomon, "Bloch Oscillations of Atoms in an Optical Potential", Phys. Rev. Lett. **76**, 4508–4511 (1996) (cit. on p. 59).

[175] T. Rom, "Bosonische und fermionische Quantengase in dreidimensionalen optischen Gittern: Prparation, Manipulation und Analyse", PhD thesis (Ludwig-Maximilians-Universität München, 2009) (cit. on p. 69).

[176] P. L. Gould, G. A. Ruff, and D. E. Pritchard, "Diffraction of atoms by light: The near-resonant Kapitza-Dirac effect", Phys. Rev. Lett. **56**, 827–830 (1986) (cit. on p. 70).

[177] A. Eckardt and M. Holthaus, "Avoided level crossing spectroscopy with dressed matter waves", Phys. Rev. Lett. **101**, 245302 (2008) (cit. on p. 73).

[178] D. Poletti and C. Kollath, "Slow quench dynamics of periodically driven quantum gases", Phys. Rev. A **84**, 013615 (2011) (cit. on p. 73).

[179] M. Genske and A. Rosch, "Floquet-Boltzmann equation for periodically driven Fermi systems", Phys. Rev. A **92**, 062108 (2015) (cit. on pp. 73, 74).

[180] M. Bukov, S. Gopalakrishnan, M. Knap, and E. Demler, "Prethermal Floquet Steady States and Instabilities in the Periodically Driven, Weakly Interacting Bose-Hubbard Model", Phys. Rev. Lett. **115**, 205301 (2015) (cit. on pp. 73, 74).

[181] C. Sträter and A. Eckardt, "Interband heating processes in a periodically driven optical lattice", Z. Naturforsch. A **71**, 909 (2016) (cit. on pp. 73, 74, 87, 89).

[182] E. Canovi, M. Kollar, and M. Eckstein, "Stroboscopic prethermalization in weakly interacting periodically driven systems", Phys. Rev. E **93**, 012130 (2016) (cit. on pp. 73, 74).

[183] T. Kuwahara, T. Mori, and K. Saito, "FloquetMagnus theory and generic transient dynamics in periodically driven many-body quantum systems", Annals of Physics **367**, 96 –124 (2016) (cit. on pp. 73, 74).

[184] S. I. Mistakidis, T. Wulf, A. Negretti, and P. Schmelcher, "Resonant quantum dynamics of few ultracold bosons in periodically driven finite lattices", Journal of Physics B: Atomic, Molecular and Optical Physics **48**, 244004 (2015) (cit. on p. 73).

[185] S. Lellouch, M. Bukov, E. Demler, and N. Goldman, "Parametric Instability Rates in Periodically Driven Band Systems", Phys. Rev. X **7**, 021015 (2017) (cit. on p. 73).

[186] V. Khemani, A. Lazarides, R. Moessner, and S. L. Sondhi, "Phase Structure of Driven Quantum Systems", Phys. Rev. Lett. **116**, 250401 (2016) (cit. on pp. 73, 118).

[187] P. Ponte, Z. Papić, F. Huveneers, and D. A. Abanin, "Many-Body Localization in Periodically Driven Systems", Phys. Rev. Lett. **114**, 140401 (2015) (cit. on pp. 73, 118).

[188] P. Ponte, A. Chandran, Z. Papić, and D. A. Abanin, "Periodically driven ergodic and many-body localized quantum systems", Annals of Physics **353**, 196 –204 (2015) (cit. on pp. 73, 118).

[189] P. Bordia, H. Lüschen, U. Schneider, M. Knap, and I. Bloch, "Periodically driving a many-body localized quantum system", Nat. Phys. **13**, 460–464 (2017) (cit. on pp. 73, 118).

[190] S. A. Weidinger and M. Knap, "Floquet prethermalization and regimes of heating in a periodically driven, interacting quantum system", Scientific Reports **7**, 45382 (2017) (cit. on p. 74).

[191] D. A. Abanin, W. De Roeck, and F. Huveneers, "Exponentially Slow Heating in Periodically Driven Many-Body Systems", Phys. Rev. Lett. **115**, 256803 (2015) (cit. on p. 74).

[192] D. A. Abanin, W. De Roeck, W. W. Ho, and F. Huveneers, "Effective Hamiltonians, prethermalization, and slow energy absorption in periodically driven many-body systems", Phys. Rev. B **95**, 014112 (2017) (cit. on p. 74).

[193] Z. Hadzibabic and J. Dalibard, "Two-dimensional Bose fluids: An atomic physics perspective", Rivista del Nuovo Cimento della Societa Italiana di Fisica **34(6)** (2011) 10.1393/ncr/i2011-10066-3 (cit. on p. 80).

[194] B. D. Esry, C. H. Greene, and J. P. Burke, "Recombination of Three Atoms in the Ultracold Limit", Phys. Rev. Lett. **83**, 1751–1754 (1999) (cit. on p. 86).

[195] J. Stenger, S. Inouye, M. R. Andrews, H.-J. Miesner, D. M. Stamper-Kurn, and W. Ketterle, "Strongly Enhanced Inelastic Collisions in a Bose-Einstein Condensate near Feshbach Resonances", Phys. Rev. Lett. **82**, 2422–2425 (1999) (cit. on p. 86).

[196] C. Sias, H. Lignier, Y. Singh, A. Zenesini, D. Ciampini, O. Morsch, and E. Arimondo, "Observation of photon-assisted tunneling in optical lattices", Phys. Rev. Lett. **100**, 040404 (2008) (cit. on p. 90).

[197] M. Reitter, J. Näger, K. Wintersperger, C. Sträter, I. Bloch, A. Eckardt, and U. Schneider, "Interaction Dependent Heating and Atom Loss in a Periodically Driven Optical Lattice", Phys. Rev. Lett. **119**, 200402 (2017) (cit. on p. 94).

[198] Z. Yan, M. Li, L. Chen, C. Chen, and J. Chen, "Density of states and thermodynamic properties of an ideal system trapped in any dimension", Journal of Physics A: Mathematical and General **32**, 4069 (1999) (cit. on p. 100).

[199] V. Bagnato, D. E. Pritchard, and D. Kleppner, "Bose-Einstein condensation in an external potential", Phys. Rev. A **35**, 4354–4358 (1987) (cit. on p. 101).

[200] T. Liu, L. W. Clark, and C. Chin, "Exotic domain walls in Bose-Einstein condensates with double-well dispersion", Phys. Rev. A **94**, 063646 (2016) (cit. on p. 118).

[201] L. W. Clark, L. Feng, and C. Chin, "Universal space-time scaling symmetry in the dynamics of bosons across a quantum phase transition", Science **354**, 606–610 (2016) (cit. on p. 118).

[202] T. Li, L. Duca, M. Reitter, F. Grusdt, E. Demler, M. Endres, M. Schleier-Smith, I. Bloch, and U. Schneider, "Bloch state tomography using Wilson lines", Science **352**, 1094–1097 (2016) (cit. on p. 119).

[203] M. Atala, M. Aidelsburger, J. T. Barreiro, D. Abanin, T. Kitagawa, E. Demler, and I. Bloch, "Direct measurement of the Zak phase in topological Bloch bands", Nat Phys **9**, 795–800 (2013) (cit. on p. 119).

[204] H.-I Lu, M. Schemmer, L. M. Aycock, D. Genkina, S. Sugawa, and I. B. Spielman, "Geometrical Pumping with a Bose-Einstein Condensate", Phys. Rev. Lett. **116**, 200402 (2016) (cit. on p. 119).

[205] Z. bo Wang, H. Jiang, H. Liu, and X. Xie, "Floquet Majorana fermions in driven hexagonal lattice systems", Solid State Communications **215**, 18 –26 (2015) (cit. on p. 119).

[206] Z. Yan, B. Li, X. Yang, and S. Wan, "A General Time-Periodic Driving Approach to Realize Topological Phases in Cold Atomic Systems", **5**, 16197 (2015) (cit. on p. 119).

[207] T. Oka and H. Aoki, "Photovoltaic Hall effect in graphene", Phys. Rev. B **79**, 081406 (2009) (cit. on p. 119).

[208] A. G. Grushin, A. Gómez-León, and T. Neupert, "Floquet Fractional Chern Insulators", Phys. Rev. Lett. **112**, 156801 (2014) (cit. on p. 119).

[209] S. Scherg, "Periodically modulated hexagonal optical lattices", MA thesis (Ludwig-Maximilians-Universität München, 2015) (cit. on p. 122).

[210] Y. Tenenbaum Katan and D. Podolsky, "Generation and manipulation of localized modes in Floquet topological insulators", Phys. Rev. B **88**, 224106 (2013) (cit. on p. 122).

[211] D. T. Tran, A. Dauphin, A. G. Grushin, P. Zoller, and N. Goldman, "Probing topology by "heating": Quantized circular dichroism in ultracold atoms", Science Advances **3** (2017) `10.1126/sciadv.1701207` (cit. on p. 125).

[212] S. Raghu, X.-L. Qi, C. Honerkamp, and S.-C. Zhang, "Topological Mott Insulators", Phys. Rev. Lett. **100**, 156401 (2008) (cit. on p. 126).

[213] C. Wu, D. Bergman, L. Balents, and S. Das Sarma, "Flat Bands and Wigner Crystallization in the Honeycomb Optical Lattice", Phys. Rev. Lett. **99**, 070401 (2007) (cit. on p. 126).

[214] C. Wu, "Orbital Ordering and Frustration of p-Band Mott Insulators", Phys. Rev. Lett. **100**, 200406 (2008) (cit. on p. 126).

[215] L. Zheng, L. Feng, and W. Yong-Shi, "Exotic electronic states in the world of flat bands: From theory to material", Chinese Physics B **23**, 077308 (2014) (cit. on p. 126).

[216] K. Sun, Z. Gu, H. Katsura, and S. Das Sarma, "Nearly Flatbands with Nontrivial Topology", Phys. Rev. Lett. **106**, 236803 (2011) (cit. on p. 126).

[217] E. Tang, J.-W. Mei, and X.-G. Wen, "High-Temperature Fractional Quantum Hall States", Phys. Rev. Lett. **106**, 236802 (2011) (cit. on p. 126).

[218] T. Neupert, L. Santos, C. Chamon, and C. Mudry, "Fractional Quantum Hall States at Zero Magnetic Field", Phys. Rev. Lett. **106**, 236804 (2011) (cit. on p. 126).

[219] F. Wilczek, "Quantum Mechanics of Fractional-Spin Particles", Phys. Rev. Lett. **49**, 957–959 (1982) (cit. on p. 126).

[220] A. Rozhkov, A. Sboychakov, A. Rakhmanov, and F. Nori, "Electronic properties of graphene-based bilayer systems", Physics Reports **648**, Electronic properties of graphene-based bilayer systems, 1 –104 (2016) (cit. on p. 126).

[221] D.-K. Ki, V. I. Falko, D. A. Abanin, and A. F. Morpurgo, "Observation of Even Denominator Fractional Quantum Hall Effect in Suspended Bilayer Graphene", Nano Letters **14**, PMID: 24611523, 2135–2139 (2014) (cit. on p. 126).

[222] J. I. A. Li, C. Tan, S. Chen, Y. Zeng, T. Taniguchi, K. Watanabe, J. Hone, and C. R. Dean, "Even-denominator fractional quantum Hall states in bilayer graphene", Science **358**, 648–652 (2017) (cit. on p. 126).

[223] Z. Papić and D. A. Abanin, "Topological Phases in the Zeroth Landau Level of Bilayer Graphene", Phys. Rev. Lett. **112**, 046602 (2014) (cit. on p. 126).

[224] C. Nayak, S. H. Simon, A. Stern, M. Freedman, and S. Das Sarma, "Non-Abelian anyons and topological quantum computation", Rev. Mod. Phys. **80**, 1083–1159 (2008) (cit. on p. 126).

Danksagung

Nach langer gemeinsamer Zeit am Lehrstuhl möchte ich mich bei vielen Personen ausdrücklich bedanken, da sie maßgeblich zum Gelingen dieser Arbeit beigetragen haben: Zuallererst möchte ich mich bei meinem Doktorvater Immanuel Bloch dafür bedanken, dass er mir die Möglichkeit gegeben hat, in seiner Gruppe zu promovieren und dass er trotz eines vollen Terminkalenders immer Zeit für Fragen und Diskussionen hatte. Des Weiteren bedanke ich mich bei Ulrich Schneider für die gute Betreuung. Bei physikalischen Fragen und technischen Problemen konnte er stets schnell und professionell weiterhelfen. Ein besonderer Dank geht an Monika Schleier-Smith für die tatkräftige Unterstützung im Labor. Sie konnte mir und dem gesamten Laborteam vieles mit auf den Weg geben.

Darüber hinaus bedanke ich mich bei meinen Laborkolleginnen Lucia Duca und Tracy Li für die schöne gemeinsame Zeit. Ihr habt während meiner Masterarbeit und den ersten drei Jahren meiner Promotion stets für gute Laune und eine tolle Atmosphäre gesorgt. Ohne euch wären diese Jahre nur halb so schön gewesen. Ich werde die gemeinsame Zeit und auch die vielen Wochenendaktivitäten, inklusive der ein oder anderen längeren Nacht, in guter Erinnerung behalten. Ich hoffe, dass unsere Freundschaft noch lange bestehen bleibt.

Ein großer Dank geht an Jakob Näger und Karen Wintersperger, die die letzten Jahre mit mir im Labor verbracht haben. Es hat sehr viel Spaß gemacht mit euch zu arbeiten und ich hoffe, dass ihr in der Zukunft noch viel Erfolg haben werdet.

Außerdem möchte ich mich bei der "Feinschmeckercrew" Henrik Lüschen, Sebastian Scherg und Thomas Kohlert bedanken, sowie bei Michael Schreiber und Pranjal Bordia für die lustigen Mittagspausen.

Ich danke André Eckardt und Christoph Sträter für die sehr gute Zusammenarbeit. André war stets kurzfristig erreichbar und hat sich immer viel Zeit genommen, um meine vielen Fragen zu beantworten. Durch deine theoretische Unterstützung hast du einen großen Teil zum Erfolg unseres Experiments beigetragen.

Ein weiterer Dank geht an Ildiko Kecskesi und Kristina Schuldt für ihre Hilfe bei organisatorischen Fragen. Insbesondere möchte ich mich bei Ildiko dafür bedanken, dass sie häufig unmöglich erscheinende Dinge möglich gemacht hat. Zudem möchte ich Bodo Hecker für die Unterstützung beim Entwickeln und Reparieren der Laborelektronik danken.

Bei Jürgen Aust und den Mitarbeitern der Werkstatt möchte ich mich dafür bedanken, dass sie unsere stets dringenden und kurzfristigen Aufträge immer schnell und präzise bearbeitet haben.

Meinen Eltern danke ich für die bedingungslose Unterstützung in all den Jahren.

Zu guter Letzt möchte ich mich bei Kerstin für all die gemeinsamen Jahre und die schöne Zeit miteinander bedanken.